THE HONG KONG POLYTECHNIC UNIVERSITY
香港理工大學
Pao Yue-kong Library
包玉剛圖書館

Copyright Undertaking

This thesis is protected by copyright, with all rights reserved.

By reading and using the thesis, the reader understands and agrees to the following terms:

1. The reader will abide by the rules and legal ordinances governing copyright regarding the use of the thesis.
2. The reader will use the thesis for the purpose of research or private study only and not for distribution or further reproduction or any other purpose.
3. The reader agrees to indemnify and hold the University harmless from and against any loss, damage, cost, liability or expenses arising from copyright infringement or unauthorized usage.

IMPORTANT

If you have reasons to believe that any materials in this thesis are deemed not suitable to be distributed in this form, or a copyright owner having difficulty with the material being included in our database, please contact lbsys@polyu.edu.hk providing details. The Library will look into your claim and consider taking remedial action upon receipt of the written requests.

Pao Yue-kong Library, The Hong Kong Polytechnic University, Hung Hom, Kowloon, Hong Kong

http://www.lib.polyu.edu.hk

ADDITIVE MANUFACTURING OF HIGH ENTROPY ALLOYS BY LASER ENGINEERED NET SHAPING

SHUAI GUAN

PhD

The Hong Kong Polytechnic University

2020

The Hong Kong Polytechnic University

Department of Industrial and Systems Engineering

Additive Manufacturing of High Entropy Alloys by Laser Engineered Net Shaping

Shuai GUAN

A thesis submitted in partial fulfillment of the
requirements for the degree of Doctor of Philosophy

April 2020

CERTIFICATE OF ORIGINALITY

I hereby declare that this thesis is my own work and that, to the best of my knowledge and belief, it reproduces no material previously published or written, nor material that has been accepted for the award of any other degree or diploma, except where due acknowledgement has been made in the text.

____________ (Signed)

GUAN Shuai (Name of student)

Abstract

Differing from conventional alloys with a single major element, high entropy alloys (HEAs) comprise multiple elements (typically ≥5) in significant atomic fractions (often 5 to 35 at.%), possibly with alloying elements, and have higher configurational entropies. Since their first emergence in 2004, HEAs have attracted considerable research interest because they define a new and near-infinite compositional space with diverse microstructures and improved properties. However, the vast majority of HEAs (e.g. CrMnFeCoNi) were processed by casting, possibly followed by cold deformation and subsequent annealing. For particular hard or brittle HEAs (e.g. $AlCoCrFeNiTi_{0.5}$), certain post processing routes (e.g. cold deformation) are not applicable. Furthermore, these approaches are often used to generate simple geometry parts and require post tooling. It is also worth mentioning that, similar to conventional alloys, HEAs often face the dilemma of strength-plasticity trade-off. To address these issues, the laser engineered net shaping (LENS^{TM}) process, a typical additive manufacturing (AM) process, was adopted to manufacture HEAs in this project. The LENS^{TM} process allows for the manufacturing of 3D complex-shaped parts with fine microstructures and good mechanical properties in a single print. The LENS^{TM} process also provides the flexibility of multi-material (i.e. multi-phase) design, and may be a feasible approach to achieve enhanced strength-plasticity synergy of HEAs.

In this study, we first performed a systematic study on the microstructural evolution

and cracking behavior of a simple ternary equi-atomic CrCoNi alloy during the AM process. The increased laser scan speed generates more heterogenous grain structures (i.e. columnar plus equiaxed). Furthermore, the increased laser scan speed achieves more pronounced quenching effects and hence finer microstructures, and a quantitative relationship between the cooling rate and celluar spacing is established. The increased laser scan speed can trigger the solidification cracking of the CrCoNi alloy due to larger thermal gradients and thermal stresses.

Based on the above findings, the microstructures and mechanical behavior of various AM-ed HEAs were further investigated. The LENS^{TM}-deposited FCC CrMnFeCoNi HEA exhibits a multi-scale microstructure, i.e. columnar grains, solidification substructures and dislocation substructures. The tensile deformation process is mainly accommodated by dislocation activities with the assistance of deformation twinning. The high tensile yield strength of the LENS^{TM}-deposited CrMnFeCoNi HEA originates from the initial-dislocation strengthening. The decreased uniform tensile elongation of the LENS^{TM}-deposited HEA CrMnFeCoNi is attributed to the increased dynamic dislocation recovery rate and hence the weakened work hardening capability.

The $AlCoCrFeNiTi_{0.5}$ HEA was also additively manufactured by the LENS^{TM} process. The microstructure of the LENS^{TM}-deposited $AlCoCrFeNiTi_{0.5}$ HEA consists of proeutectic B2-structured dendrites delineated by lamellar or rod-like B2/A2 eutectic structures. Such microstructures are successfully described with the aid of Scheil’s solidification simulation. Furthermore, proeutectic B2-structured grains are totally equiaxed and randomly textured. A high density of nucleation sites (a minimum of 3×10^9 /mm^3) is estimated, which is attributed to the frequent dendrite fragmentation. The volume fraction ϕ values of equiaxed crystals at the solidification front are estimated to be greater than 49% for the various G - V combinations established in this study, indicating that fully equiaxed grain microstructures can be formed and hence providing a theoretical basis for our experimental findings.

In view of the strength-plasticity trade-off of monolithic AM-ed HEAs, we additively manufactured CrMnFeCoNi/AlCoCrFeNiTi$_{0.5}$ laminated HEAs that exhibit an enhanced strength-plasticity synergy during compression (yield strength up to 990 MPa and no complete fracture until 80% strain), surpassing those of monolithic bulk HEAs. The enhanced strength-plasticity synergy originates from heterogenous microstructures of ultra-hard BCC equiaxed grains and soft FCC columnar grains periodically arranged in the AlCoCrFeNiTi$_{0.5}$ and CrMnFeCoNi lamellae respectively.

In this research, the microstructures and mechanical behavior of various HEAs manufactured by the LENS^{TM} process are investigated. The findings demonstrate the capability of the LENS^{TM} process for manufacturing HEAs with high performance and also provide guidelines for producing fully equiaxed alloys during the AM process. This work also demonstrates a feasible and flexible way to design HEAs with heterogenous microstructures and improved mechanical properties.

Publications arising from the research

1. **S. Guan**, D. Wan, K. Solberg, F. Berto, T. Welo, T.M. Yue, K.C. Chan, Additive manufacturing of fine-grained and dislocation-populated CrMnFeCoNi high entropy alloy by laser engineered net shaping, Mater. Sci. Eng. A 761 (2019) 138056.
2. K. Solberg, **S. Guan**, S.M.J. Razavi, T. Welo, K.C. Chan, F. Berto, Fatigue of additively manufactured 316L stainless steel: The influence of porosity and surface roughness, Fatigue Fract. Eng. Mater. Struct. 42 (2019) 2043-2052.
3. **S. Guan**, K. Solberg, D. Wan, F. Berto, T. Welo, T.M. Yue, K.C. Chan, Formation of fully equiaxed grain microstructure in additively manufactured $AlCoCrFeNiTi_{0.5}$ high entropy alloy, Mater. Des. 184 (2019) 108202.
4. **S. Guan**, D. Wan, K. Solberg, F. Berto, T. Welo, T.M. Yue, K.C. Chan, Additively manufactured $CrMnFeCoNi/AlCoCrFeNiTi_{0.5}$ laminated high-entropy alloy with enhanced strength-plasticity synergy, Scr. Mater. 183 (2020) 133-138.
5. **S. Guan**, D. Wan, K. Solberg, F. Berto, T. Welo, T.M. Yue, K.C. Chan, Metallurgy of a ternary equiatomic alloy produced using laser engineered net shaping, to be submitted.

Acknowledgements

Firstly, I would like to express my sincere gratitude to my chief supervisor Prof. K.C. Chan for his continuous support for my PhD research. His patience, high standards and immense knowledge guide me throughout my PhD study. I also want to thank Prof. T. Welo and Prof. F. Berto at Norwegian University of Science and Technology (NTNU), for their provision of facilities that could assist in materials characterization. Moreover, I gratefully thank my ex-co-supervisor retired Prof. T.M. Yue at the Hong Kong Polytechnic University for useful discussions throughout my PhD study.

I also thank Mr. K. Solberg (NTNU), Dr. D. Wan (NTNU), Dr. D. Wang (NTNU), Dr. X. Lu (NTNU), Mr. S.Q. Wang (NTNU), Dr. D.D. Zhao (NTNU), Dr. X.Z. Lu, Dr. S.H. Chen, Dr. D.Q. Guo, Dr. L. Zhao, Dr. S.D. Feng, Dr. D.X. Han, Dr. R. Li and Ms. Y.L. Wang for useful discussions regarding my research. I am also appreciative of Mr. S.Y. Lau at the Materials Engineering Laboratory, Mr. K. Cheng at the Laser Laboratory and the staff at the University Research Facility in 3D Printing who provide technical support to my research.

I also thank Prof. X.G. Wang at the Institute of Metal Research, Chinese Academy of Sciences, Dr. M. Yang at National University of Singapore and Dr. D.Y. Deng at Linköping University for their insightful suggestions and fruitful discussions regarding my research.

Special thanks go to the Research Committee of the Hong Kong Polytechnic University for its financial support of my PhD project.

Finally, I would like to express my most sincere gratitude to my parents, my family members and my friends for their continuous support, understanding and encouragement throughout the period of my PhD study.

Table of contents

List of figures and tables

Chapter 1 Introduction

1.1 Research background

Conventional alloy design approaches generate alloys based on one principal element (e.g. Fe in steels), with modifications by adding relatively small amounts of other alloying elements (e.g. C in steels). This alloy design approach retains the characteristic properties of the base element that makes several attractive alloy families (e.g. steels, Ti alloy, etc.). However, this alloy concept disregards a compositional space of multi-principal elements that possibly forms desirable microstructures with improved properties. Such a new and infinite compositional space is somewhat covered by high entropy alloys (HEAs), comprising multiple elements (normally ≥5), each in significant atomic fraction (5 to 35 at.%), possibly with trace alloying elements. HEAs may form various microstructures, e.g. single-phase FCC, BCC or HCP microstructures [1-3] and more complex multi-phase microstructures [4]. Since their first emergence in 2004, HEAs have aroused intensive research interest due to certain promising properties observed in some specific HEAs. For example, the quinary equi-atomic HEA CrMnFeCoNi exhibits an exceptional fracture toughness exceeding 200 MPa $m^{1/2}$ at cryogenic temperatures (comparable to cryogenic steels [5]), making it a candidate material for low-temperature applications [1].

Until now, HEAs were often processed by conventional casting [1, 6-8], powder metallurgy [9] and magnetron co-sputtering [10], etc. To refine the microstructures and to achieve the desired properties, the as-cast HEAs are often processed by cold rolling/forging and annealing [1, 6]. These conventional metallurgical processes (e.g. casting, powder metallurgy, etc.) are often used to generate simple geometry parts, with post tooling required. For magnetron co-sputtering, it is only applicable for manufacturing thin films for ultra-small-dimension devices. Furthermore, similar to conventional alloys, HEAs often faces a dilemma in the strength-plasticity trade-off. To be more specific, FCC HEAs, e.g. quinary equi-atomic CrMnFeCoNi [1, 11], are very ductile but not strong enough. In contrast, BCC HEAs, e.g. senary non-equi-atomic $AlCoCrFeNiTi_{0.5}$ [12], are very strong but at the sacrifice of plasticity. Although a few HEAs with multi-phase (e.g. FCC + BCC) microstructures and balanced mechanical properties have recently been designed [13, 14], composition design is a trial-and-error routine. Therefore, resolving the dilemma of strength-plasticity trade-off in a cleverer way is still a big challenge.

Additive manufacturing (AM) is a process by which 3D objects are created layer upon layer from 3D models. The AM process can build large-scale parts with complex geometries and internal features, requiring little or no post tooling. Furthermore, the AM process is characterized by a highly localized melting and solidification process, and provides the possibility of achieving hierarchical microstructures with enhanced mechanical properties [15]. These advantages are the key drivers for the recent interest in the AM process in the manufacturing of HEAs. In this project, we aim to manufacture HEAs with enhanced strength-plasticity synergy by laser engineered net shaping

(LENS^{TM}) process, a typical powder-blown additive manufacturing (AM) process. In addition to the above-mentioned common advantages of the AM process, the LENS^{TM} process allows the manufacturing of laminated structures with distinct microstructures and properties, via the alternate deposition of multiple powdered materials layer-upon-layer. In other words, the LENS^{TM} process enables us to produce multi-HEAs and hence multi-phases with the aid of multi-powder feeding. Heterogeneities in the compositions, phases and microstructures can often result in properties enhancement, as can be seen, for example, in laminated materials [16]. Several micro-mechanisms, e.g. crack bridging [17] and crack blunting [18], can be induced by the laminated microstructures. We believe that the LENS^{TM}-deposited laminated HEAs with distinct phases and microstructures can circumvent the dilemma of the strength-plasticity trade-off of monolithic HEAs.

1.2 Research objectives

With the ultimate aim of manufacturing HEAs with improved strength-plasticity synergy, the specific objectives are as follows:

(1) To study the microstructural evolution and cracking behavior of a ternary equi-atomic alloy CrCoNi in the LENS^{TM} process.

(2) To understand the solidification conditions, phase formations, as-deposited microstructures and mechanical behavior of the LENS^{TM}-processed quinary HEA

CrMnFeCoNi.

(3) To understand the microstructure formation mechanism and mechanical behavior of the LENS^{TM}-processed senary HEA AlCoCrFeNiTi$_{0.5}$.

(4) To additively manufacture CrMnFeCoNi/AlCoCrFeNiTi$_{0.5}$ laminated HEAs with enhanced strength-plasticity synergy and to probe into the corresponding mechanisms.

1.3 Outline of this thesis

This thesis has 9 chapters. Chapter 1 identifies the research gaps and gives the research objectives of the PhD project. Chapter 2 describes the systematic literature review. Chapter 3 gives an overall review of the methodologies used in this study. Chapters 4, 5, 6 and 7 present the main research outcomes and discussions. Chapter 8 gives overall conclusions. Chapter 9 suggests directions for future research.

Chapter 2 Literature review

2.1 Overview

This chapter systematically reviews the research work relating to the topic of this PhD project. This section gives an overview of the literature review. Section 2.2 introduces the birth, definition and characteristics of high entropy alloys (HEAs). In Section 2.3, the microstructures of a wide range of typical HEAs are reviewed and summarized. Several phase formation rules are reviewed. Research into the phase and microstructure stability of HEAs is also reviewed. Section 2.4 is dedicated to the mechanical behavior of HEAs. Section 2.5 reviews the manufacturing routes for the HEAs, including the additive manufacturing (AM) process that has been used recently. Furthermore, some fundamental research problems related to the AM process have also been reviewed. Section 2.6 gives conclusions to this chapter.

2.2 HEAs: Birth, definition and characteristics

Conventional metal alloys have one major element (e.g. Fe in steels), with one or more alloying elements (e.g. C in steels) in small amounts. Such a conventional alloy design approach was challenged with the emergence of HEAs in 2004, comprising five or more principal elements in equi-atomic ratios [19, 20]. In Ref. [19], Cantor et al. reported several HEAs, e.g. a five-component equi-atomic HEA CrMnFeCoNi (also referred to as Cantor alloy) and a series of six-, seven-, eight- and nine-component equi-atomic HEAs. They even reported in Ref. [19], a HEA consisting of 20 elements in equi-atomic proportions, 5 at.% each of Mg, Sb, Si, Ge, Zn, Bi, Pb, Sn, Cd, Al, Nb, Mo, W, Ag, Cu, Ni, Co, Fe, Cr and Mn. It should be noted that HEAs are not restricted to equi-atomic ratios, and Yeh et al. [20] expanded the scope of HEAs to alloys comprising multiple principle elements with the concentration of each element between 5 and 35 at.%. More and more non-equi-atomic HEAs (e.g. $Al_{0.5}CoCrCuFeNi$) [6, 12] and four-component HEAs (e.g. NbMoTaW) [21] were reported. Recently, several HEAs with trace elements have been also reported. For example, Park et al. [22] studied a novel Cantor alloy with 1 at.% C additions, designated as 1%C-CrMnFeCoNi HEA. Therefore, in this thesis, HEAs refer to the alloys comprising multiple elements (normally ≥5), each in significant atomic fractions (often 5 to 35 at.%), possibly with trace alloying elements. It should be noted that some ternary equi-atomic alloys (e.g. CrCoNi) are referred to as medium entropy alloys (MEAs) [7, 23].

Such a novel alloy design approach defines a new and near-infinite compositional space, providing the possibility of discovering diverse phases and microstructures with improved properties [1, 20, 24]. Moreover, compositional characteristics of HEAs increase the configurational entropy ΔS_{conf}, as given below [25]:

$$\Delta S_{\mathrm{conf}} = k ln\omega \tag{2.1}$$

where k represents Boltzmann’s constant and ω represents the ways in which the available energy can be mixed. Therefore, the configurational entropy resulting from the formation of a solid solution from N elements can be given as follows:

$$\Delta S_{\mathrm{conf}} = -R \sum_{i=1}^{N} x_{\mathrm{i}}\, ln x_{\mathrm{i}} \tag{2.2}$$

where x_i represents the atomic fraction of the ith element. For an equi-atomic HEA system, Eq. 2.2 can be further reduced to:

$$\Delta S_{\mathrm{conf}} = RlnN \tag{2.3}$$

Obviously, the configurational entropy ΔS_{conf} increases with the number of elements for equi-atomic HEAs. As calculated, the configurational entropy of a five-component equi-atomic HEA reaches $1.61R$, a value that is much larger than those of conventional alloys. The configurational entropies of some typical conventional alloys are listed in Table 2.1. In addition to novel compositional characteristics and the large configurational entropy value, HEAs are also characterized by severe lattice distortion, as schematically shown in Fig. 2.1. Such a distorted lattice originates from the differences in atomic size, bonding energy and crystal structure among several components in HEAs. All of these characteristics make HEAs a novel class of metal alloys that deviates from conventional metal alloys.

Table 2.1 Configurational entropies of representative conventional alloys at their liquid state or random state [26].

Systems	**Alloys**	**Configurational entropies**
Low-alloy steel	4340	$0.22R$
Stainless steel	304	$0.96R$
	316	$1.15R$
High-speed steel	M2	$0.73R$

Mg alloy	AZ91D	0.35*R*
Al alloy	2024	0.29*R*
	7075	0.43*R*
Cu alloy	7-3 brass	0.61*R*
Ni-base superalloy	Inconel 718	1.31*R*
	Hastelloy X	1.37*R*
Co-base superalloy	Stellite 6	1.13*R*
BMG	$Cu_{47}Zr_{11}Ti_{34}Ni_8$	1.17*R*
	$Zr_{53}Ti_5Cu_{16}Ni_{10}Al_{16}$	1.30*R*

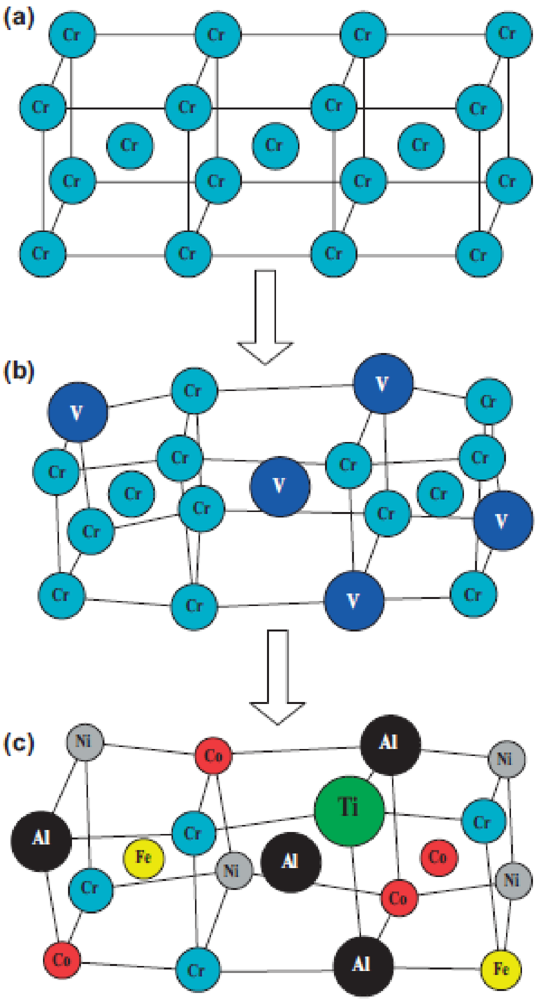

Fig. 2.1 Schematic illustration of severe lattice distortion of HEAs [27].

2.3 HEAs: Phases and microstructures

2.3.1 Single-phase solid solution microstructures

The vast number of HEAs lead to diverse phases and microstructures. Roughly speaking, they can be classified into three categories: (i) single-phase solid solution microstructures, (ii) multi-phase solid solution microstructures and (iii) multi-phase solid solution plus intermetallic microstructures.

Many HEAs were reported to exhibit a single-phase face-centered cubic (FCC), body-centered cubic (BCC) or hexagonal close packing (HCP) solid solution microstructure. For example, the quinary equi-atomic HEA CrMnFeCoNi crystallizes as a single-phase FCC solid solution structure [1, 28]. Furthermore, several equi-atomic quaternaries (CrCoNiMn, CoNiFeMn and CrCoNiFe), ternaries (CrCoNi, CoNiFe, FeNiMn, NiCoMn and CrNiFe) and binaries (NiFe and CoNi) also have a single-phase FCC solid solution structure [7, 8, 23, 29]. Deng et al. [30] also reported that the quaternary non-equi-atomic HEA $Fe_{40}Mn_{40}Co_{10}Cr_{10}$ exhibits a single-phase FCC solid solution structure in as-cast, hot-rolled and homogenized states. Similar microstructures were observed in other HEAs (e.g. FeNiCrCuCo and FeNiCrCuMo) [31]. In contrast to the FCC HEAs, HEAs consisting of refractory BCC metals (e.g. W, Mo, Nb, Ta and V) typically crystallize as a single-phase BCC solid solution structure. Senkov et al. [21] reported that both NbMoTaW and VNbMoTaW exhibit a single-phase BCC solid solution structure. Single-phase BCC solid solution microstructures were also reported for MoNbHfZrTi [32], TaNbHfZrTi [33] and TaNbHfZr [34]. It should be noted that the metals Hf, Zr and Ti have an HCP structure at room temperature, changing to a BCC structure at high temperatures, i.e. allotropic transformation. Until now, reports on HEAs with a single-phase HCP solid solution structure are rare, and such HEAs typically consist of several HCP metals (e.g. Y, Ru, Re, Gd, Tb, Dy, Tm and Lu). Such HEAs include YGdTbDyLu [2], GdTbDyTmLu [2] and CoFeReRu [3].

2.3.2 Multi-phase solid solution microstructures

In addition to single-phase FCC, BCC or HCP solid solution microstructures, multi-phase microstructures comprising multiple solid solution phases were also observed in some HEAs [35]. Li et al. [35] reported that the quaternary non-equi-atomic HEA $Fe_{50}Mn_{30}Co_{10}Cr_{10}$ achieves a dual-phase FCC plus HCP solid solution microstructure after rapid quenching from the single-phase FCC region, due to partial martensitic transformation. Fig. 2.2 gives the as-quenched microstructure that consists of a 72% FCC matrix with ~ 45 μm grain size plus 28% HCP laminate layers from several nanometers to 10 μm in thickness.

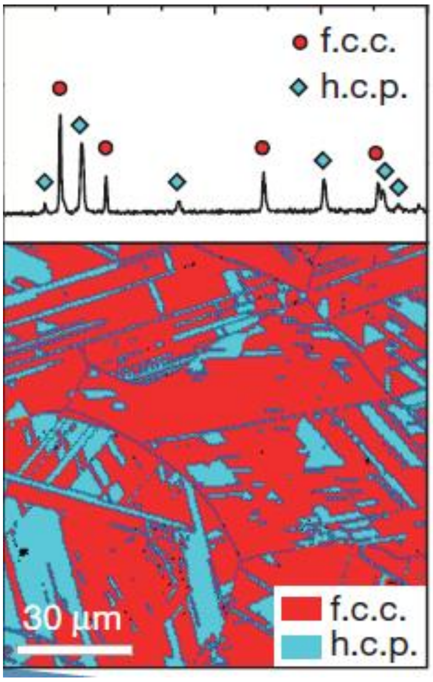

Fig. 2.2 XRD profile and EBSD phase map of $Fe_{50}Mn_{30}Co_{10}Cr_{10}$ HEA [35].

2.3.3 Multi-phase solid solution plus intermetallic microstructures

Although single- or multi-phase solid solution microstructures are common for HEAs, some of the existing HEAs contain intermetallic phases and form multi-phase solid solution plus intermetallic microstructures. Yang et al. [36] reported that the HEA CrCoNiFeAl$_x$ forms a single-phase FCC solid solution microstructure when x equals to 0.1, but changes to a basket weave-like microstructure of nanoscale FCC plus B2 phases when x increases to 0.75, and finally to nanoscale duplex BCC plus B2 microstructures when x increases to 1.5. Manzoni et al. [37] also reported that the as-cast HEA CrCoNiFeAl forms a typical dendritic microstructure comprising 52% BCC precipitates in the B2 matrix. After hot isostatic press and homogenization, 16% FCC and 14% σ phases are also formed in the HEA CrCoNiFeAl [38]. Research on the HEA CrCoNiFeAl$_x$ was also reported elsewhere [39-42].

It should be noted that the multi-phase solid solution and intermetallic microstructures formed in the HEA CrCoNiFeAl$_x$ are due to phase separation occurring in the solid state. Such decomposed microstructures were also observed for several other HEAs, e.g. CrCoNiFeCuAl$_{0.5}$ [43, 44], (FeCoNiCr)$_{94}$Ti$_2$Al$_4$ [45] and Al$_{0.5}$Cr$_{0.9}$FeNi$_{2.5}$V$_{0.2}$ [4]. Tsuno et al. [43] reported that the as-cast HEA CrCoNiFeCuAl$_{0.5}$ has a single-phase FCC solid solution structure. However, nanoscale separation into L1$_2$ and FCC coherent phases was confirmed for the HEA CrCoNiFeCuAl$_{0.5}$ and such phase separation is enhanced after annealing [44]. Ye et al. [45] also reported that L1$_2$-Ni$_3$(Ti, Al) phases precipitate in the FCC solid solution microstructure after thermomechanical treatment of HEA (FeCoNiCr)$_{94}$Ti$_2$Al$_4$. Such a FCC+L1$_2$ duplex microstructure was also reported for HEA Al$_{0.5}$Cr$_{0.9}$FeNi$_{2.5}$V$_{0.2}$ [4].

Besides phase separation occurring in the solid state, eutectic solidification also forms multi-phase microstructures. For instance, the HEA $AlCoCrFeNi_{2.1}$ forms a fine lamellar $L1_2$/B2 duplex microstructure due to eutectic solidification [13, 46-50]. Ma et al. [51] also reported that the microstructure of the HEA $CrCoNiFeAlNb_x$ changes from B2 proeutectic dendrites plus B2/Laves interdendritic eutectics (i.e. hypoeutectic) when x equals to 0.25 or 0.5 to Laves proeutectic dendrites plus B2/Laves interdendritic eutectics when x increases to 0.75 (i.e. hypereutectic). Phases and microstructures of some typical HEAs are listed in Table 2.2.

Table 2.2 Summary of phases and microstructural characteristics of some typical HEAs and a few ternary equi-atomic MEAs. C: casting; H: homogenization; R: rolling; A: annealing; d.c. MCS: d.c. magnetron co-sputtering; WQ: water quenching; SLM: selective laser melting.

Systems	**Processing**	**Phases**	**Refs.**
CrCoNi	C+A	FCC	[7, 23]
CoNiFe	C+H+R+A	FCC	[7]
FeNiMn	C+H+R+A	FCC	[7]
NiCoMn	C+H+R+A	FCC	[7]
CrNiFe	C+H	FCC	[7, 8]
CrCoNiMn	C+H+R+A	FCC	[7]
CoNiFeMn	C+H+R+A	FCC	[7]
CrCoNiFe	C+A	FCC	[7, 23]
CrCoNiFePd	C+A	FCC	[23]
CrMnFeCoNi	C+R+A	FCC	[1, 7, 28]

FeNiCrCuCo	C	FCC	[31]
FeNiCrCuMo	C	FCC	[31]
$Fe_{40}Mn_{40}Co_{10}Cr_{10}$	C+R+H	FCC	[30]
$FeCoCrNiC_{0.05}$	SLM	FCC	[52]
$Fe_{50}Mn_{30}Co_{10}Cr_{10}$	C	FCC	[35]
$Fe_{50}Mn_{30}Co_{10}Cr_{10}$	C+R+H (WQ)	FCC+HCP	[35]
$FeCoCrNiC_{0.05}$	SLM+A	$FCC+Cr_{23}C_6$	[53, 54]
$FeCoNi(AlSi)_x$	C	x=0, 0.1, 0.2, FCC; x=0.3, FCC+BCC; x=0.4 ~ 0.8, BCC	[55]
$CrCoNiFeAl_x$	C	x=0.1, FCC; x=0.75, FCC+B2; x=1.5, BCC+B2	[36]
$CrCoNiFeAl_{0.1}$	C+R+A	FCC	[56]
$CrCoNiFeCuAl_{0.5}$	C/C+A	$FCC+L1_2$	[44]
$AlCoCrFeNiMo_x$	C	BCC	[57]
NbMoTaW	C	BCC	[21, 58]
NbMoTaW	d.c. MCS	BCC	[10]
VNbMoTaW	C	BCC	[21]
MoNbHfZrTi	C	BCC	[32]
TaNbHfZrTi	C	BCC	[33]
TaNbHfZr	C	BCC	[34]
$AlCoCrFeNiMo_x$	C	BCC+α	[57]
YGdTbDyLu	C	HCP	[2]

GdTbDyTmLu	C	HCP	[2]
CoFeReRu	C	HCP	[3]
$AlCoCrFeNiTi_x$	C	B2+BCC	[12, 59, 60]
$AlCoCrFeNiTi_{0.5}Cu_x$	C	B2+BCC	[61]
$AlCoCrFeNi_{2.1}$	C/C+R+A	B2+A2	[13, 46-50]

2.3.4 Phase formation rule

The microstructures of HEAs have been reviewed. Some of these HEAs form a single-phase FCC, BCC or HCP solid solution microstructure. Others form a more complex multi-phase microstructure consisting of multiple solid solution phases or solid solution plus intermetallic phases. Until now, several rules have been established to explain or predict the phase formation of HEAs [27, 62, 63]. Zhang et al. [27] adopted two parameters, δ and ΔH_{mix}, to analyze the phase formation of HEAs. The first parameter δ describes the atomic size difference among the elements in HEAs and is defined as follows:

$$\delta = \sqrt{\sum_{i=1}^{N} c_{\mathrm{i}}(1 - r_{\mathrm{i}}/\bar{r})^2} \tag{2.4}$$

where N is the total number of elements in a HEA system, c_{i} is the atomic percentage of element i, r_{i} is the covalent atomic radius of element i, with the values compiled elsewhere [64], and $\bar{r} = \sum_{i=1}^{N} c_{\mathrm{i}} r_{\mathrm{i}}$ is the arithmetical mean value of covalent atomic radius.

The other parameter ΔH_{mix} (i.e. mixing enthalpy) describes the chemical compatibility among the elements in HEAs and is defined as follows:

$$\Delta H_{\mathrm{mix}} = \sum_{i=1, i\neq j}^{N} \Omega_{\mathrm{ij}} c_{\mathrm{i}} c_{\mathrm{j}} \tag{2.5}$$

where $\Omega_{ij} = 4\ \Delta H_{AB}^{mix}$ is the melt-interaction parameter between elements i and j, and ΔH_{AB}^{mix} is the mixing enthalpy of binary liquid alloys, with the values compiled elsewhere [65].

Zhang et al [27] created a 2D map illustrating the dependence of HEAs' microstructures on these two parameters, δ and ΔH_{mix}, as shown in Fig. 2.3. When the atomic-size difference δ is small and the mixing enthalpy ΔH_{mix} is not sufficiently negative, the HEAs tend to form solid solutions (zone S). With increase of δ and decrease of ΔH_{mix}, the formation of some ordered phases (zones S′ and B2) or even amorphous phases (zone B1) will be promoted.

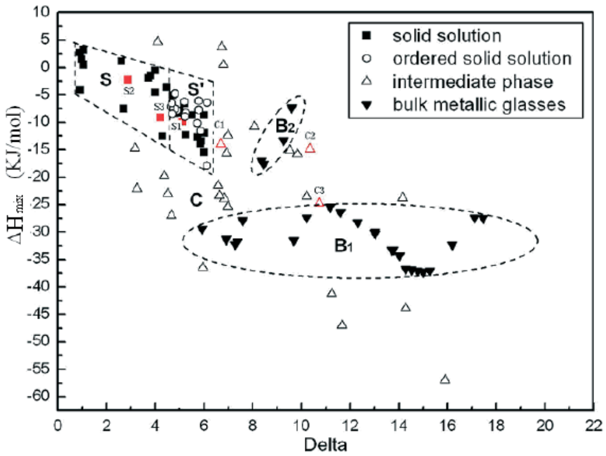

Fig. 2.3 Dependence of microstructures on the δ and ΔH_{mix} values [27]. Here δ value is amplified by a hundred times.

Ye et al. [62] developed a geometric model that evaluates the atomic size mismatch among elements and calculates the intrinsic residual strain in HEAs. They pointed out that a single- to multi-phase microstructure occurs when the root-mean-square (R.M.S.) residual strain reaches ~5%, and an amorphous microstructure even forms when the RMS residual strain value reaches above ~10%. Ye et al.'s theory satisfactorily explains the microstructure formation of many HEAs (Fig. 2.4).

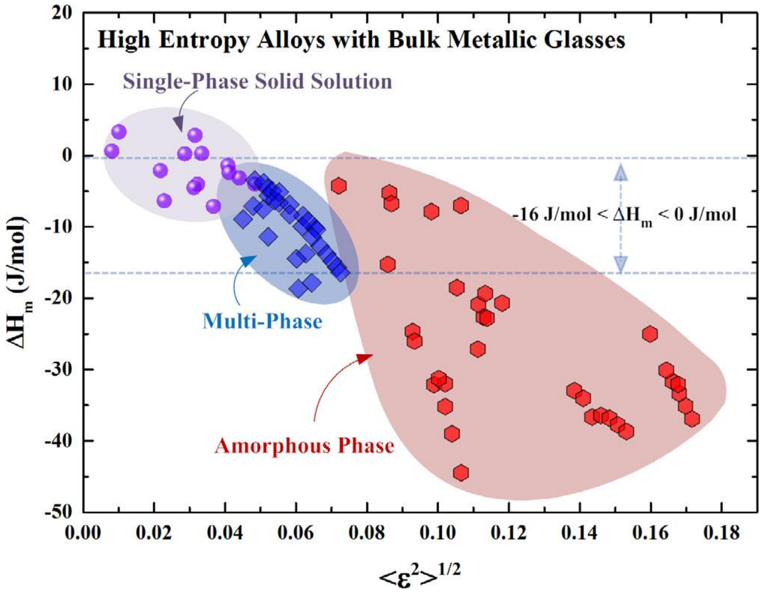

Fig. 2.4 Effect of RMS residual strain on the microstructure formation [62].

Guo et al. [63] adopted the parameter valence electron concentration (*VEC*) to analyze the formation of the FCC and BCC phases in HEAs. The parameter *VEC* is defined as follows:

$$VEC = \sum_{i=1}^{N} c_\mathrm{i} \, (VEC)_\mathrm{i} \qquad (2.6)$$

where $(VEC)_\mathrm{i}$ is the *VEC* value for element *i* in a HEA system, with the values compiled in Ref. [63]. Guo et al. [63] satisfactorily explain the formation of FCC and BCC phases in HEAs using *VEC* parameter, as shown in Fig. 2.5. More specifically, FCC phases form when $VEC \geq 8$; FCC plus BCC phases form when $VEC < 6.87$; BCC phases form when $6.87 \leq VEC < 8$.

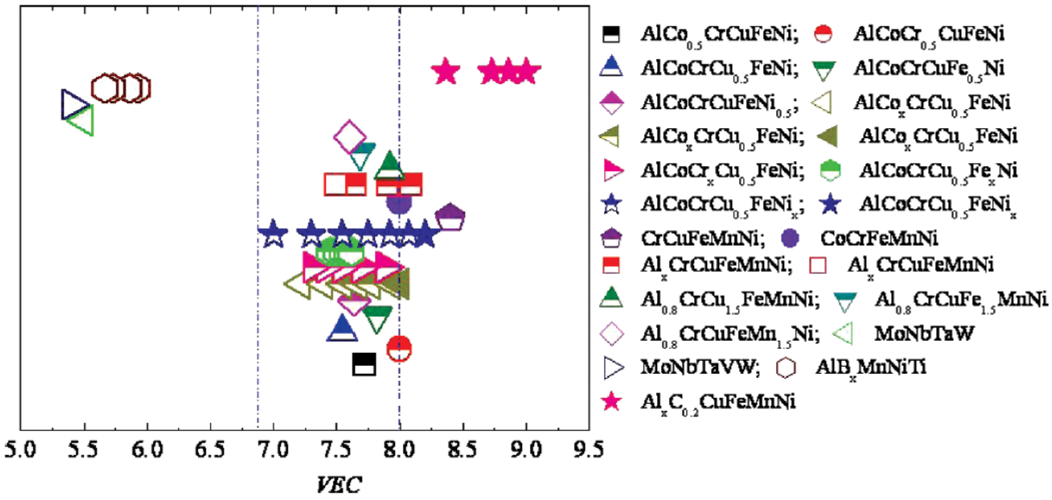

Fig. 2.5 Effects of *VEC* value on the formation of FCC and BCC phases [63]. Open symbols for BCC phase; half closed symbols for FCC plus BCC phases; closed symbols for FCC phase.

It is worth mentioning that, in addition to the above-mentioned parametric approaches, machining learning may be an alternative to predict the phase formation of the HEAs. Based on the experimental dataset of HEAs, machine learning algorithms can effectively predict the phase formation without the need of explicit programming. For example, in Ref. [66], Huang et al. employed several machine learning algorithms, i.e. artificial neural network (ANN), support vector machine (SVM) and K-nearest neighbours (KNN), to predict the phase formation of the HEAs. Among them, the ANN algorithm exhibits a good testing accuracy of 74.3% for the classification of the phases of the HEAs. Overall speaking, the phase formation rule of the HEAs is a hot topic, and the relevant research is still underway.

2.3.5 Phase and microstructure stability

The phases and microstructures of HEAs have been reviewed in Sections 2.3.1−2.3.4. It should be noted, however, that these phases or microstructures are not necessarily stable from a thermodynamic point of view, and that prolonged annealing treatments may trigger their evolution. For example, recent studies reported the decomposition of the single-phase FCC solid solution microstructure of HEA CrMnFeCoNi into a more complex multi-phase microstructure [67-70]. The Cr-rich secondary phases were observed to precipitate, especially at grain boundaries [67, 68]. Pickering et al. [69] reported that the σ phase precipitates in the HEA CrMnFeCoNi during prolonged anneals at 973 K. Otto et al. [70] also reported that $L1_0$-NiMn, B2-CoFe and Cr-rich BCC phases are formed in the HEA CrMnFeCoNi during prolonged anneals at 773 K. Similar research on the phase and microstructure stability of HEA has also been reported elsewhere [8, 34, 58, 62, 71-81]. These works demonstrate that the reported phases and microstructures of HEAs may deviate from their thermal equilibria and need to be carefully evaluated, especially those HEAs that are promising for high-temperature applications. In addition to prolonged anneals, high pressure also induces the phase transition of some HEAs, e.g. HCP phases start to form in the single-phase FCC HEA CrCoNiFe when the pressure increases to 13.5 GPa, and reach a weight percent of ~36% when the pressure increases to 39 GPa [23].

2.4 HEAs: Mechanical behavior

2.4.1 Deformation and fracture mechanisms

HEAs deform through dislocation motion, nano-twinning or martensitic phase transformation. Regarding the deformation mechanisms, FCC HEA CrMnFeCoNi [28, 82-84] is probably the most researched. Laplanche et al. [84] studied the formation and hence evolution of the deformation substructures in CrMnFeCoNi during tensile straining. At small global strain levels, the tensile deformation process is dominated by dislocation motion. When the global strain level increases, for example to ~ 7.4% for 77 K and ~ 25% for 293 K, nano-twinning is activated and serves as an additional deformation mechanism. The nano-twinning behavior introduces more interfaces and hence increases the strain hardening capability. Fig. 2.6 shows the formation and hence evolution of the deformation substructures in CrMnFeCoNi during tensile straining at 77 K. During compression, however, a larger strain value may be needed to trigger the nano-twinning mode, since mechanical twinning is still negligible when CrMnFeCoNi is compressed to 46% strain [83].

The ternary equi-atomic MEA CrCoNi, a variant alloy of the quinary equi-atomic HEA CrMnFeCoNi, has also received a lot of attention in terms of deformation behavior [85-87]. Laplanche et al. [85] also deduced that the nano-twinning mode can be activated at a smaller critical strain level (4.0 ~ 6.7% for 77 K; 9.7 ~ 12.9% for 293 K) in CrCoNi. The earlier activation of nanotwins in CrCoNi well explains the enhanced strain hardening capability and hence increased ultimate tensile strength and ductility values. Miao et al. [86] even observed narrow HCP laths within the nanotwins, forming nanotwin/HCP lamellae in strained CrCoNi. Furthermore, the deformation mechanism of the as-quenched HEA $Fe_{50}Mn_{30}Co_{10}Cr_{10}$ with a FCC+HCP duplex microstructure has been also studied [30, 35]. During the tensile process, strain-induced HCP martensite is formed, with deformation nanotwins inside these HCP martensitic phases.

In addition to those HEAs with single or multiple solid solution phases, HEAs are also commonly formed in the form of nanoscale precipitates embedded in the matrix [4, 43-45] or eutectic structures [13, 14, 46-50]. Shi et al. [14] prepared a hierarchical eutectic HEA $AlCoCrFeNi_{2.1}$ by casting, followed by thermo-mechanical processes. Such an eutectic HEA has a high yield strength of 1490 MPa and a ductility of 16%. This hierarchical eutectic HEA $AlCoCrFeNi_{2.1}$ exhibits a FCC/B2 lamellar structure with 1.5 ~ 5 μm lamellar spacing. Inside these lamellae, there are recrystallized grains with an average grain size of 0.71 μm. Besides FCC recrystallized grains, intergranular B2 grains with ~ 350 nm grain size and intragranular B2 grains with 50 ~ 180 nm grain size are also formed inside the FCC lamellae. During tensile straining, the soft FCC phases tend to deform plastically initially. In contrast, the hard B2 phases are still elastic, thus creating a plastic strain gradient in the soft FCC lamellae near the lamella interfaces. Such a plastic strain gradient needs to be accommodated by the storage of geometrically necessary dislocations (GNDs) that in turn generate a large long-range back-stress up of to ~ 950 MPa as measured by synchrotron XRD. Such a high back-stress leads to the high yield strength. During further straining, both the soft FCC and hard B2 phases deform plastically, and further strain gradients, and hence more GNDs are generated, leading to extra strain-hardening capacity. Therefore, high ultimate tensile strength and reasonable ductility are achieved. The deformation micro-mechanisms in this hierarchical eutectic HEA $AlCoCrFeNi_{2.1}$ during tensile straining are shown in Fig. 2.7.

For those HEA with single-phase BCC/multi-phase BCC plus intermetallics, normally only compressive properties and subsequent fracture mechanisms are evaluated due to their poor plasticity. Ma et al. [51] reported that the HEA CrCoNiFeAlNb$_x$ shows a typical quasi-cleavage fracture pattern after compression. Chen et al. [88] also observed several brittle fracture characteristics on the compression fracture surface of the HEA CrCoNiFeAlZr$_x$, e.g. radial herringbone patterns, tear edges and flat fracture patterns. Obviously, this type of HEAs normally fails in a very brittle manner, with very limited plasticity.

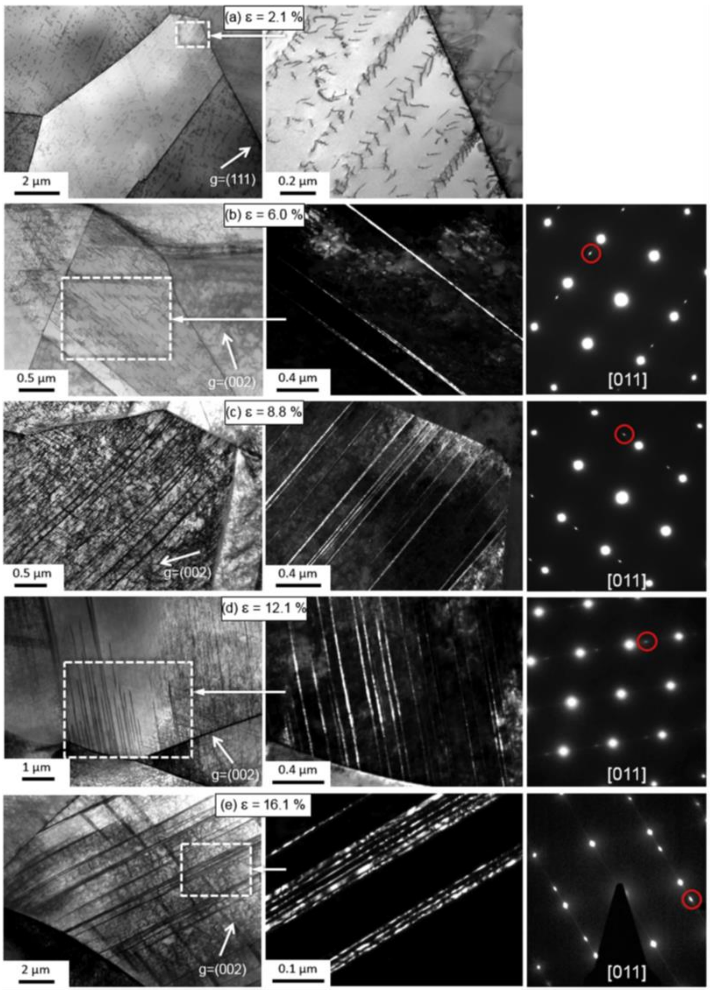

Fig. 2.6 The formation and hence evolution of the deformation substructures during tensile straining of CrMnFeCoNi at 77 K [84].

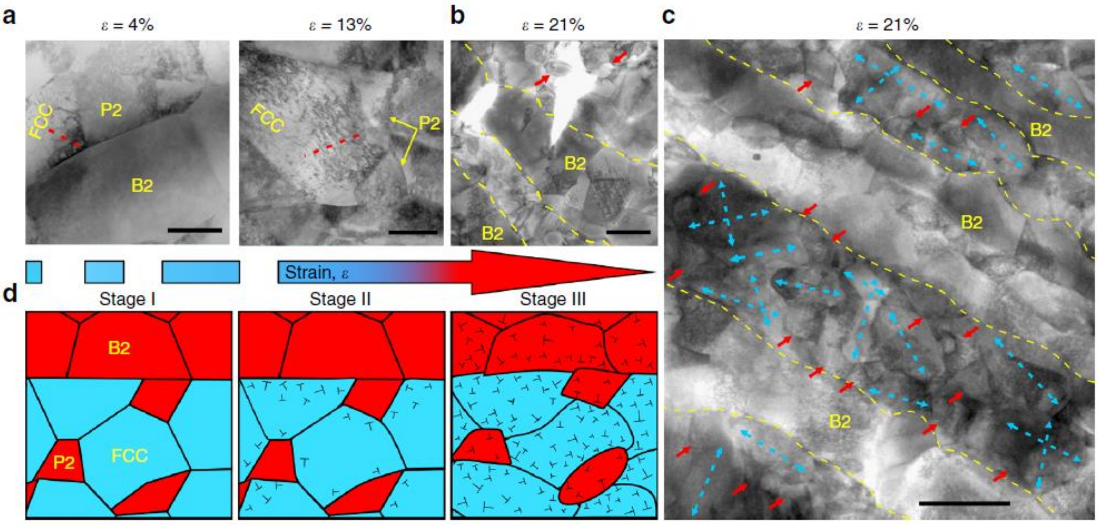

Fig. 2.7 Deformation evolutions in the hierarchical eutectic HEA $AlCoCrFeNi_{2.1}$ during tensile straining [14].

2.4.2 Mechanical properties

Due to the diverse microstructures and hence the deformation and fracture mechanisms, the mechanical properties of HEAs are very scattered. HEAs with a single-phase FCC solid solution structure are normally ductile but not strong enough, e.g. CrMnFeCoNi [28, 82-84]. In contrast, HEAs with a single-phase BCC solid solution structure are normally strong but at the sacrifice of plasticity. For example, BCC HEAs NbMoTaW and VNbMoTaW exhibit a compressive yield strength above 1 GPa but a compressive plasticity below 3% at room temperature [21]. Such a low plasticity is consistent with the clear brittle quasi-cleavage fracture observed from the compressive fracture surface. The fracture strain was reported to increase to above 10% or even 20% at temperatures above 878 K, whereas the compressive yield strength dropped by 30 ~ 40% [21]. Similar to the other metals and alloys, the size-effect phenomenon has also been found in HEAs. For example, Zou et al. [58] prepared single-crystalline NbMoTaW pillars with diameters ranging from 2 μm to 200 nm from the as-cast form using focused ion beam (FIB) milling and then compressed these pillars using a flat-punch tip in a nano-indenter. Both strength and plasticity are improved significantly as compared to the bulk counterparts reported in Ref. [21], due to the decreased average size of the dislocation sources. Zou et al. [10] also prepared 3-μm thick HEA NbMoTaW films using the d.c. magnetron co-sputtering technique, and the FIB technique was then used to mill fine-scale pillars (1 μm to 100 nm in diameter) out of the prepared HEA films. The compressive yield strength of these pillars reaches a maximum of 10 GPa and the compressive plastic strain reaches over 30%. These findings demonstrate that these single-phase BCC refractory HEAs may be promising materials for small-dimensional device applications, but for large-scale engineering structures they are not safe to use due to the low plasticity at room temperature. High strength and low plasticity have been also reported for other single-phase BCC/multi-phase BCC plus intermetallics HEAs, e.g. $AlCoCrFeNiMo_x$ (x=0~0.5) [57], $AlCoCrFeNiTi_x$ (x=0~1.5) [12], $AlCoCrFeNiTi_{0.5}Cu_x$ (x=0~0.5) [61], $FeCoNi(AlSi)_x$ (x=0.4~0.5) [55], $CrCoNiFeAlV_x$ (x=0~1) [89], $CrCoNiFeAlZr_x$ (x=0~0.5) [88] and $CrCoNiFeAlNb_x$ (x=0~0.75) [51].

In contrast, HEAs with multi-phase (both strong and ductile phases) microstructures provide more possibilities of achieving balanced mechanical properties. Furthermore, single-phase but heterogenous microstructures also leads to a balanced combination of strength and ductility. For example, Wu et al. [56] reported that cold rolling followed by intermediate temperature anneals imparts heterogenous structures (i.e. heterogenous grain structures, dislocations and twins) to the HEA $CrCoNiFeAl_{0.1}$ despite a single-phase FCC solid solution structure. Hence, a balanced combination of strength and ductility (yield strength: 711 MPa; ultimate tensile strength: 928 MPa; uniform elongation: 30%) could be achieved.

2.5 Manufacturing routes

2.5.1 Overview

Until now, the vast majority of HEAs were manufactured by casting, possibly followed by post processing to control the grain size [1, 6-8, 24]. For example, many FCC HEAs were processed by casting and characterized by coarse grains that yield low strength, and to refine the grains and achieve fully recrystallized microstructures, post cold rolling/forging and annealing treatment is often needed [7, 8]. In this way, the strength is often enhanced, at the sacrifice of the plasticity. Furthermore, it is worth mentioning that the whole process is complex and time-consuming and only simple geometries can be generated, with post tooling required. In contrast, for certain strong and brittle HEAs (e.g. BCC $AlCoCrFeNiTi_{0.5}$, etc.), these post cold deformation and machining processes are often impossible and therefore this class of HEAs has to be used in the as-cast state [12]. Furthermore, similar to conventional alloys, monolithic HEAs processed by these conventional routes typically face a dilemma in the strength-plasticity trade-off. More specifically, FCC HEAs are ductile but not sufficiently strong, and BCC HEAs are strong but at the sacrifice of plasticity.

Besides various casting processes, mechanical alloying (MA) followed by spark plasma sintering (SPS) was also used to manufacture bulk HEAs, e.g. $CoFeNiAl_{0.5}Ti_{0.5}$ [90], CrMnFeCoNi [9, 91] and $AlCoCrFeNiTi_{0.5}$ [92]. However, these SPS-ed HEAs also face the strength-plasticity trade-off. For example, the SPS-ed HEA CrMnFeCoNi exhibits a ultra-high compressive strength of ~ 2 GPa, with a low compressive plasticity of < 16% [9]. Liu et al. [91] also reported that the HEA CrMnFeCoNi processed by MA+SPS processes exhibits nanocrystalline microstructures with a high ultimate tensile strength of ~ 1 GPa but a low tensile ductility of ~ 6%. In addition to the above-mentioned processes, the magnetron co-sputtering technique was also used to process HEAs [10]. However, only thin films for ultra-small-dimensional devices can be prepared.

In contrast, the AM process produces physical components, layer upon layer, from a digital design, which increases design freedom and manufacturing flexibility. Complex-shaped components can be built in a single step by the AM process, requiring little or no post machining. Furthermore, the AM process is a localized melting and solidification process in essence that typically creates a strong temperature gradient and high solidification velocity. Therefore, hierarchical microstructures, e.g. fine grains and solidification and dislocation substructures, can be achieved, which may lead to excellent mechanical properties [15]. Until now, the AM process has been used to process a variety of conventional metal alloys, e.g. stainless steels [15, 93-97], tool steels [98], Ti alloys [99-101], superalloys [102], AlSi10Mg [103], TiC/AlSi10Mg composites [104], and some of them exhibit good performances. The AM process has also been used to manufacture some hard-to-process alloys, e.g. Ti-22Al-25Nb intermetallics, and a good combination of strength and ductility (yield strength: 960 MPa; strain to failure: 23%) has been achieved [105]. Furthermore, possible in-situ phase decomposition during the AM process may also lead to desirable microstructures and hence good mechanical properties [100, 101]. These advantages are the key drivers for the recently increasing interest in manufacturing of HEAs using the AM process.

Some HEAs, especially Al_xCoCrFeNi [29, 52, 106-111] and CrMnFeCoNi [112-120] alloys, have been recently processed by various AM processes with different processing parameters. Other work includes AM of $Co_{1.5}CrFeNi_{1.5}Ti_{0.5}Mo_{0.1}$ [121], TiZrNbMoV [122], $Co_{0.5}CrCu_{0.5}FeNi_{1.5}AlTi_{0.4}$ [123], C-containing CrCoNiFe [54] and compositionally graded HEAs, i.e. $AlCo_xCr_{1-x}FeNi$ ($0 \leq x \leq 1$) [124], $Al_xCrCuFeNi_2$ ($0 < x < 1.5$) [125] and $AlCrFeMoV_x$ ($0 < x < 1$) [126]. However, more thorough research on the AM of HEAs is still needed. Section 2.5.2 introduces the AM process in terms of thermal history, microstructure formation, cracking, porosity and residual stress. The possible effects of process parameters are also reviewed. Furthermore, a review on the AM processing of HEAs is also given.

2.5.2 AM processes

2.5.2.1 Thermal history

The AM process involves rapid heating and melting followed by rapid resolidification of materials in the scale of melt pool, with subsequent numerous reheating-recooling cycles of the as-solidified region, as seen in Fig. 2.8 [98]. Such a complex thermal process determines the as-solidified microstructures (e.g. phase formation, grain structure and solidification substructure), defects (e.g. cracks and pores) formation and hence the final mechanical properties. Therefore, studying this thermal process, especially the rapid solidification process, is of significance for the AM process.

Multiple methods, i.e. experimental or numerical, have been used to study the complex thermal process intrinsic to the AM process. The experimental measurements used thermocouples [127] or imaging pyrometers [97, 127-129]. The thermocouples record temperatures away from the melt pool as a function of time during the whole fabrication event. Therefore, a series of reheating-recooling sequences at a specified location can be recorded. In contrast, the in-situ high-speed thermal imaging technique allows for the measurement of temperatures in the top surface of the melt pool and hence enables the calculation of the temperature gradients and cooling rates. However, the subsequent reheating-recooling sequences of the as-solidified melt pool cannot be recorded. In contrast to these experimental measurement methods, numerical methods [97, 98, 128, 130, 131] allow for the simulation of the entire thermal process inside the whole melt pool. For example, Xiong et al. [128] established a general model to evaluate the thermal behavior during deposition, by assuming that Fourier's law of heat conduction is obeyed and that convection and radiation can be neglected. In Ref. [128], Fourier's law of heat conduction in 3D space was written in a vector form:

$$\vec{q} = -k \cdot \vec{\nabla} T = -k_x \frac{\partial T}{\partial x}\vec{x} - k_y \frac{\partial T}{\partial y}\vec{y} - k_z \frac{\partial T}{\partial z}\vec{z} \qquad (2.7)$$

where $\vec{q}$ is the heat flow rate conducted per unit area, k is the thermal conductivity, T is the temperature, $\vec{\nabla} = \frac{\partial}{\partial x}\vec{x} - k_y \frac{\partial}{\partial y}\vec{y} - k_z \frac{\partial}{\partial z}\vec{z}$ is the operator. The heat flow equilibrium in the interior of the body is written as follows:

$$\vec{\nabla}(k \cdot \vec{\nabla} T) = \frac{\partial}{\partial x}(k_x \frac{\partial T}{\partial x}) + \frac{\partial}{\partial y}(k_y \frac{\partial T}{\partial y}) + \frac{\partial}{\partial z}(k_z \frac{\partial T}{\partial z}) = -H \qquad (2.8)$$

where H is the rate of heat generated per unit volume. In the AM process, the laser heat can be transferred to the material:

$$H_1 = \alpha \cdot Q \qquad (2.9)$$

where α is the absorptivity at a specific laser wavelength, and Q is the laser power. Part of absorbed heat from the laser can be stored in the material, which can be expressed as follows:

$$H_2 = -\rho \cdot C \cdot \frac{\partial T}{\partial t} \tag{2.10}$$

where ρ is the material density, C is the material specific heat capacity and $\frac{\partial T}{\partial t}$ is the temperature change rate. Considering $H = H_1 + H_2$, they derived:

$$\vec{\nabla}(k \cdot \vec{\nabla}T) + \alpha \cdot Q = \rho \cdot C \cdot \frac{\partial T}{\partial t} \tag{2.11}$$

By applying appropriate boundary conditions, the thermal behavior can be evaluated. However, it is worth mentioning that, in some cases, the low reliability of numerical methods is still a big problem. In addition to those experimental and numerical methods, some researchers also roughly estimated the cooling rate during melt pool solidification, based on empirical relations between the cooling rate and the scale of the solidification substructure [102].

Until now, the solidification process of the vast majority of conventional metal alloys during the AM process has been investigated by experimental or numerical methods. For example, Zheng et al. [98], with the aid of the alternate-direction explicit (ADE) finite difference method (FDM), reported the complex thermal process during the laser engineered net shaping (LENS$^{\text{TM}}$) processing (in total of 20-deposited layers) of H13 tool steel and estimated that the cooling rate reaches 10^3 ~ 10^4 K/s during the initial stage, and such a quenching effect decreases and even disappears when a critical height is reached. Xiong et al. [128], with the aid of a combination of thermal imaging and finite element modelling (FEM) methods, determined that the maximum temperature gradient and maximum cooling rate during the LENS^{TM} processing of WC-Co cerments reach 10^3 K/mm and 10^3 K/s, respectively. Similar temperature gradients ($10^2 \sim 10^3$ K/mm) and cooling rates ($10^3 \sim 10^4$ K/s) values established in the LENS^{TM} process have also been reported elsewhere [97, 132, 133]. In contrast, the selective laser melting (SLM) process (i.e. one type of AM process) normally creates a steeper temperature gradient and a more rapid quenching effect, reaching the order of $10^3 \sim 10^5$ K/mm and $10^4 \sim 10^6$ K/s, respectively [102, 134].

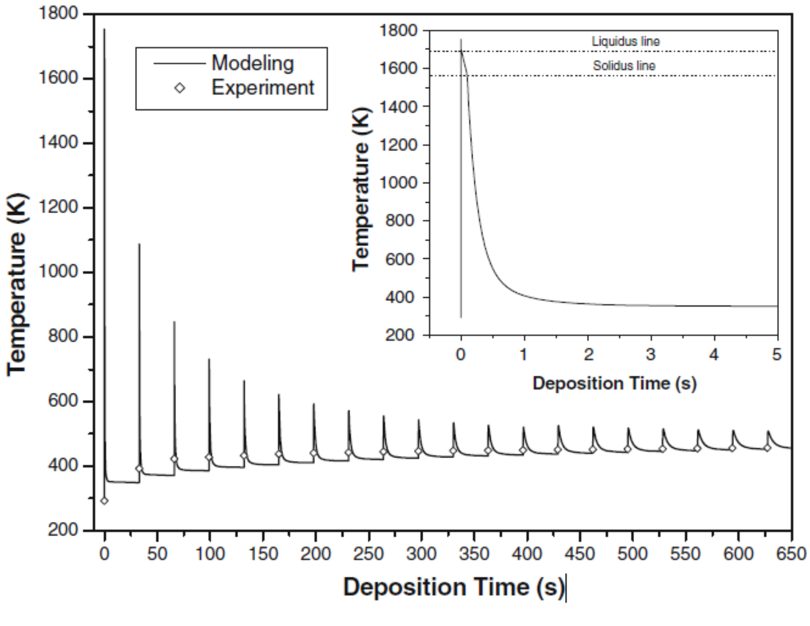

Fig. 2.8 Temperature evolution of the first deposited layer during the LENS^{TM} processing (in total of 20-deposited layers) of H13 tool steel [98].

2.5.2.2 Microstructure formation

The highly localized melting and solidification process intrinsic to the AM process creates a large temperature gradient (*G*) within the melt pool and hence promotes the formation and subsequent epitaxial growth of columnar dendrites during solidification. To be more specific, columnar grain structures, typically with crystallographic textures, are more common, as evidenced from the AM-ed alloys [102, 135, 136]. Within the columnar grains, some solidification substructures, dendritic or cellular, are formed. As compared with the dendritic structures, the cellular ones are more common in the AM-ed alloys because the rapid quenching effects during the AM process suppress the formation of tertiary or even secondary arms [102, 137]. Furthermore, a high density of dislocations is normally formed along the cellular boundaries [93, 102].

However, this is not always the case, and many publications report on microstructure control, e.g. grain structure control [135, 136, 138-148]. As is known, the temperature gradient in the liquid metal (*G*) and the solidification front growth velocity (*V*) concurrently control the grain structures. The *G* and *V* values vary from process to process, and in a specific process they also vary as functions of space and time [133, 135, 142, 143]. Often, the *G* value increases from the top to the bottom along the liquid-solid interface, and the *V* value vice versa. Therefore, equiaxed grains may form and grow in some regions, e.g. the top of the melt pool, with low *G* and high *V* values. However, these equiaxed grains may be remelted when depositing the subsequent layer. The competitive growth between columnar grains and between columnar/equiaxed grains has been studied [149, 150]. One relevant example is shown in Fig. 2.9.

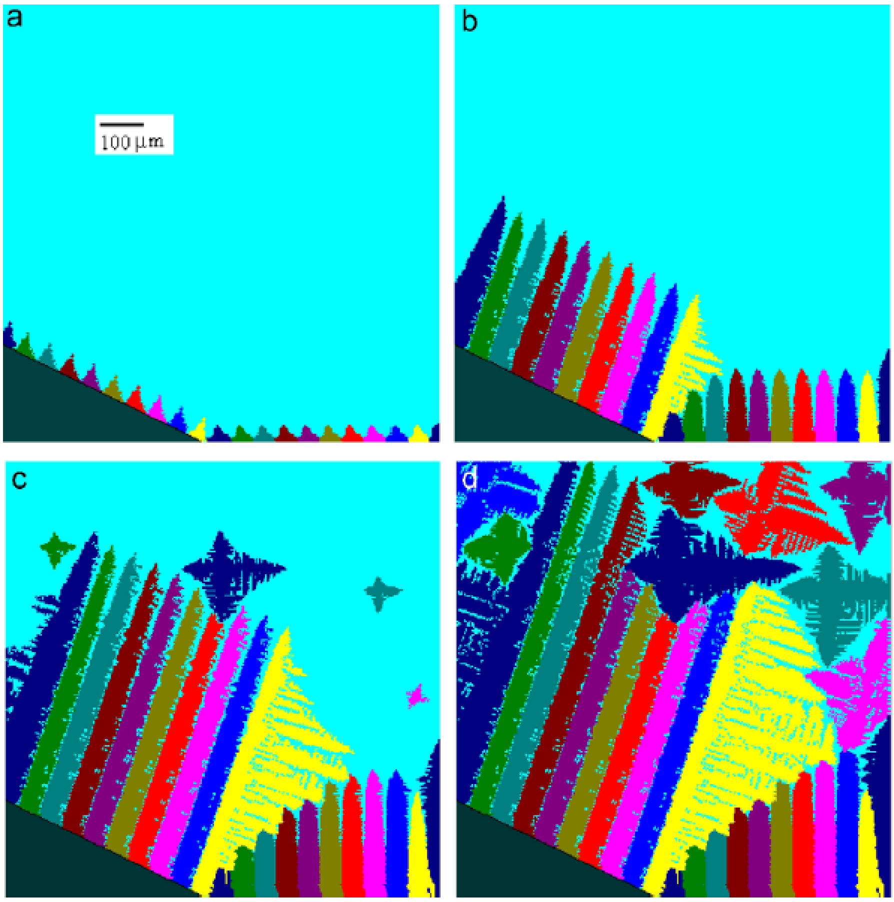

Fig. 2.9 Prediction of grain structures evolution in the weld pool of a Ni-Cr alloy [150].

In some cases, a small region of equiaxed grain structures may be retained [151, 152]. However, it is difficult or even impossible to achieve fully equiaxed grain microstructures [106, 151, 153]. Recent studies focus attention on the tendency of the alloys themselves to form equiaxed grains during the AM process. For instance, Yang et al. [154] and Spierings et al. [155] found that the AM-ed Sc- and Zr-modified Al alloy comprises significant fine equiaxed grains at the melt pool boundaries, and they attributed the increased tendency towards forming equiaxed grain structures to the $Al_3(Sc,Zr)$ particles in the remelting zone acting as heterogenous nucleation sites during solidification. Achieving fully equiaxed grain microstructures for this modified Al alloy is feasible, but closely controlling the processing parameters (e.g. scan speed) and thus the solidification conditions is a prerequisite.

Furthermore, the grain structure formed during the AM process may be altered with the aid of external forces. Although this is not frequently reported in AM literature, such effects of external forces have been extensively reported in casting [156, 157] and welding [158] literature. Zuo et al [156] reported that intensive melt shearing promotes the transformation of the grain structure from columnar to equiaxed and simultaneously refine the grain size of as-casted Mg alloys. Zhang et al. [157] also reported that certain energy/electromagnetic fields (e.g. pulsed electric currents and travelling magnetic field) promote the grain size refinement of the as-casted Al-7%Si alloy. Yuan et al. [158] reported that arc oscillation during welding of Mg alloys promotes the grain structure transition from columnar to equiaxed and facilitates grain refining (Fig. 2.10). Wang et al. [159] reported that ultrasonic treatment during solidification of Sn-Bi alloys facilitates the formation of fine and equiaxed grains. Zhang et al. [160] treated their SLM-ed Ti-6Al-4V specimen surfaces by a ultrasonic impact head once every two layers and finally achieved specimens with alternate columnar and equiaxed grains. Obviously, the equiaxed grains are not formed from the melt and they are attributed to the recrystallization process provoked by the combined effects of compressive plastic deformation in the surface region and subsequent reheating process. Very recently, Todaro et al. [161] applied high-intensity ultrasonic vibration assisted AM to process a series of engineering alloys (e.g. IN625 superalloy), and the microstructures vary to fine equiaxed primary γ grains with a near random crystallographic texture from coarse columnar primary γ grains with a strong <100> texture. Additionally, solidification microstructures can be well controlled by turning the ultrasonic vibration on and off. The relevant results are shown in Fig. 2. 11.

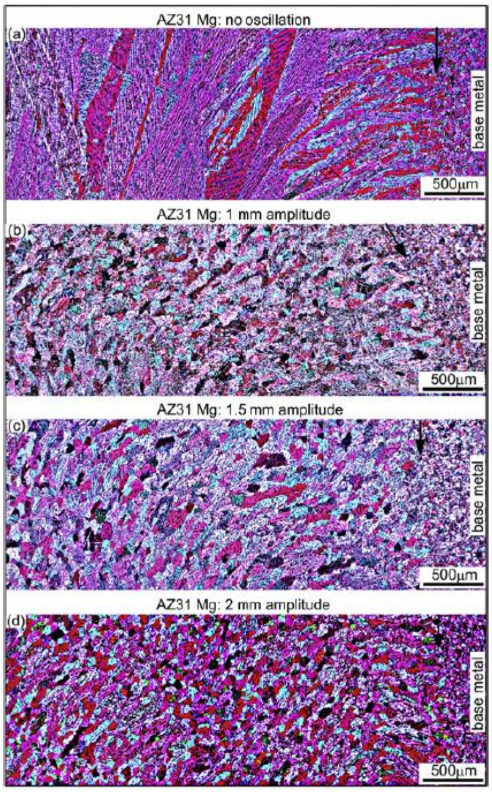

Fig. 2.10 Grain refinement of Mg alloy welds by arc oscillation [158].

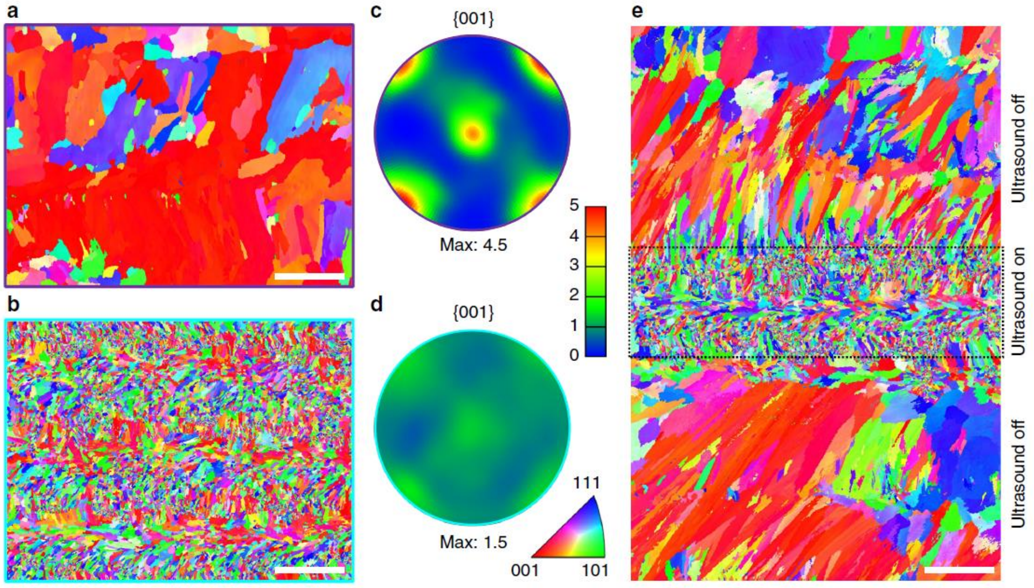

Fig. 2.11 AM of IN625 superalloy without (a, c) and with (b, d) high-intensity ultrasonic vibration assistance [161]. (e) Control of the solidification microstructure by turning the ultrasonic vibration on and off. Scale bars 250 μm.

Promoted dendrite fragmentation is one of the popular mechanisms for the grain structure evolution in the presence of external forces. Dendrite fragmentation during solidification has been in-situ characterized by X-ray diagnostics [162, 163] and studied by phase-field simulation [164]. For example, in a Al-Cu alloy some dendrite fragments were demonstrated to detach from the dendritic tip and move ahead of the solid-liquid interface, and these fragments may grow to form a new grain [162]. The X-ray image sequences are shown in Fig. 2.12. The presence of those external forces is believed to promote the dendrite fragmentation phenomenon during solidification due to multiple effects, e.g. remelting and mechanical breakup [158]. These fragments may serve as new equiaxed grains which block the columnar growth, providing the possibilities of achieving near fully equiaxed grain microstructures.

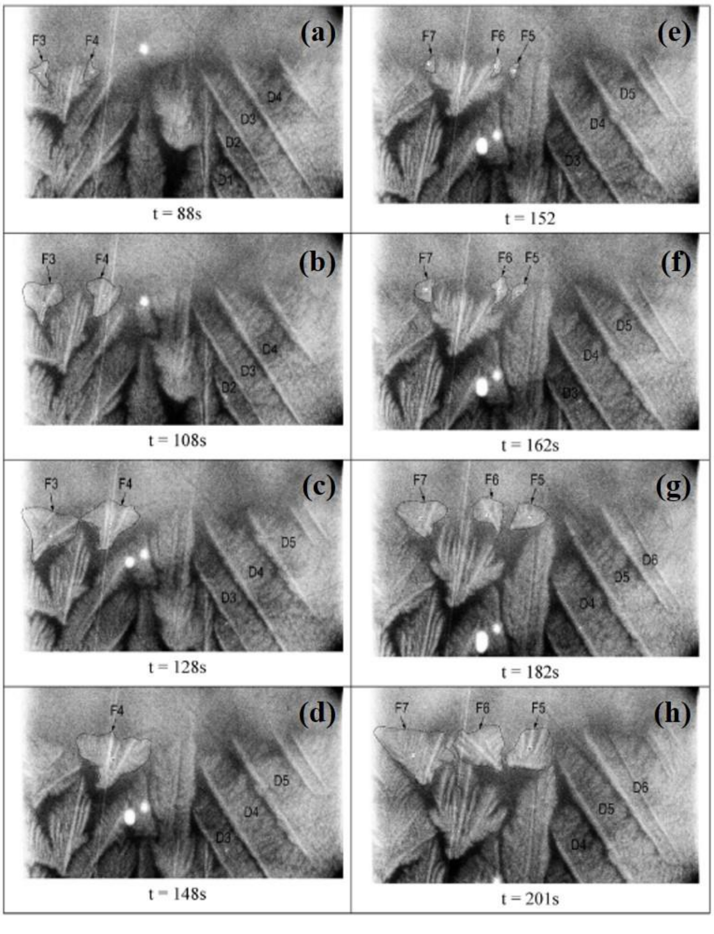

Fig. 2.12 Sequences of X-ray images for a Al-Cu alloy during solidification [162]. F3 and F4 in (a-d) and F5, F6 and F7 in (e-h) are dendrite fragments.

2.5.2.3 Cracking

Cracking is a critical problem for the AM-ed parts because the large-sized cracks severely degrade their mechanical properties. Until now, several cracking mechanisms, e.g. solidification cracking (i.e. hot tearing) [165-168], liquation cracking [169-174], strain-age cracking [175] and ductility-dip cracking [176, 177], have been described in the welding or AM literature. Solidification cracks, also known as hot tears, are formed at the very last stage of solidification when the dendrites have coalesced and the interdendritic melt could initiate a crack under thermal stress [166, 167]. Unlike the solidification cracking occurring in the mushy zone of the melt pool, liquation cracking occurs in the heat affected zone (HAZ) where some low melting temperature phases (e.g. eutectics and carbides) at the grain boundaries are remelted and these liquated regions can initiate cracks [172-174]. Obviously, both cracking phenomenon occur in the presence of a liquid film. In contrast, ductility-dip cracking and strain-age cracking occur in a solid state. As its name suggests, ductility-dip cracking occurs due to reduced ductility triggered at intermediate temperatures [177]. Such a cracking behavior was well documented in Ni-based superalloys cooled down from high temperatures after laser processing. In contrast, strain-age cracking occurs during post ageing heat treatment. Post ageing heat treatment leads to precipitation strengthening but sacrifices ductility. Such a combined effect may trigger strain-age cracking [175]. Some post treatments may be applied to heal the cracks, for example, Zhao et al. [178] reported that the hot isostatic pressing (HIP) process can heal cracks up to a few millimeters in AM-ed parts.

2.5.2.4 Porosity

In addition to cracking, porosity formation is also a problem for the AM process since pores deteriorate the fatigue performance of AM-ed alloys [96]. Porosity in the AM-ed parts can be examined by micro X-ray computed tomography (CT) [105, 179]. Often, two types of pores, i.e. lack-of-fusion defects and gas pores, are observed. Lack-of-fusion defects are typically several hundred micrometers large, irregular and site-specific (i.e. at inter-track and inter-layer locations) [180, 181]. In contrast, gas pores are typically spherical, originating from the gas bubbles in the starting powders [182] or the occasional vaporization of surface materials [183]. Again, the HIP process can be used to heal these pores formed in the AM process to some extent [184]. The effects of the starting powders and post HIP processes on the porosity of the AM-ed specimens can be clearly seen in Fig. 2.13. In addition to cracks and pores, oxide films are also occasionally observed in some specific AM-ed alloys, e.g. Al_2O_3 and Cr_2O_3 oxide films in the AM-ed IN718 alloy [185].

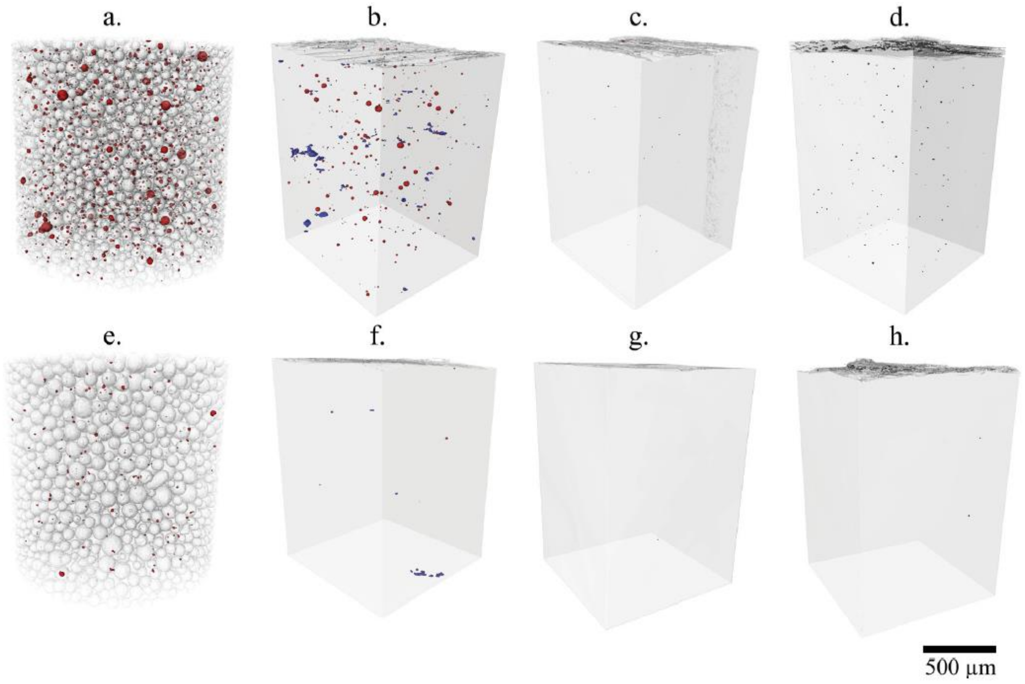

Fig. 2.13 CT results showing porosity evolution in the AM-ed Ti alloys [182]. (a) and (e) powder, (b) and (f) as-built, (c) and (g) HIP-ed, and (d) and (h) HIP-ed plus β solution heat treatment.

2.5.2.5 Residual stress

Often, a complex residual stress field exists in the final AM-ed parts. Such a complex residual stress field is normally undesirable because it causes component distortion and hence a mismatch between the achieved and the design geometries. In some cases, the residual stress field can even lead to the cracking of the AM-ed parts. Furthermore, the residual stress, especially the tensile residual stress, degrades the fatigue and tensile properties of the AM-ed parts. Therefore, it is critical to measure and control the residual stress locked in the AM-ed parts. Multiple techniques have been used to measure the residual stress in the AM-ed parts, e.g. nanoindentation [186, 187], neutron diffraction [187-191], X-ray diffraction [187] and the contour method [187, 188, 190]. In nanoindentation measurement, for example, multiple nanoindentation parameters, e.g. loading curve, unloading curve, material pile-up and hardness, are sensitive to residual stress (tensile or compressive; magnitude), and their relations have been quantitively established in several models. Through these models and measured nanoindentation parameters, the residual stress can be evaluated.

2.5.2.6 Effects of process parameters and post treatments

The fundamental research problems related to the AM process are controlled by a combination of several process parameters, e.g. powder quality, deposition pattern, laser power and laser scan speed. Gas atomized (GA) powders were reported to be more likely to be hollow (entrapped gas), as compared with the plasma rotation electrode preparation (PREP) powders [192]. The entrapped gas in the GA particles may not escape out of the melt pool during the AM process, characterized by high cooling rates, and thus leads to the increased porosity of the final AM parts. The deposition pattern has a pronounced effect on the resulting residual stress. Nickel et al. [193] reported that a raster deposition pattern with the scan vector rotated by 90° between successive layers produces a smaller residual stress and hence a lower deflection. Regarding the final grain structure, it is influenced by several process parameters, e.g. substrate orientation [194, 195].

Besides those AM process parameters, post treatments have been proven to be very effective for tuning the mechanical properties of the AM-ed parts [192, 196-199]. For example, Prashanth et al. [197] reported that annealing heat treatment leads to the increased ductility of SLM-fabricated Al-12Si alloy, despite sacrificing strength, and an improved strength-ductility synergy is achieved. Liu et al. [198] reported that quenching followed by low-temperature tempering promotes the formation of martensite and the dissolution of brittle carbides in AM-ed martensitic stainless steel, leading to an increase of the ultimate tensile strength from 905 to 1283 MPa, without significant ductility decrease. Wu et al. [199] reported that post ultrasonic processing increases the bending strength and bending modulus of AM-ed alloys. Therefore, the process parameters and post treatment need to be determined carefully.

2.5.2.7 AM processing of HEAs

As mentioned before, some HEAs have been printed using various AM processes, and these include CrMnFeCoNi [112-120, 200], Al_xCoCrFeNi [29, 52, 106-111, 201],

$Co_{0.5}CrCu_{0.5}FeNi_{1.5}AlTi_{0.4}$ [123], TiZrNbMoV [122], $Co_{1.5}CrFeNi_{1.5}Ti_{0.5}Mo_{0.1}$ [121], $AlCoCrFeNiTi_{0.5}$ [202], AlCoFeNiSmTiVZr [203], compositionally graded HEAs [124-126, 204], etc. To the best of our knowledge, the first relevant work was done by Brif et al. in 2015 [29]. In their work, they adopted a numerical approach based on the Rosenthal model [205], to establish a relationship between the melt penetration depth and a series of printing parameters during the SLM process. In this way, they identified the printing parameters to ensure that the layers can be fully melted, and they successfully printed the FeCoNiCr HEA with high strength and ductility using the SLM process. In contrast, Sun et al. [201] found that the FeCoNiCr HEA is very prone to solidification cracking during the SLM process, and using the Rappaz-Drezet-Gremaud model (refer to Ref. [206]), they predicted that the decreased grain size can effectively lower the characteristic depression pressure and hence suppress the solidification cracking susceptibility. Haase et al. [207] simulated the equilibrium and non-equilibrium solidification processes to predict the phase formation and elemental redistribution of HEAs during the AM process, and they successfully printed CrMnFeCoNi HEA from the elemental powder blends using the laser metal deposition (LMD) process. Similarly, Zhu et al. [112] also additively manufactured CrMnFeCoNi HEA with hierarchical microstructures and tensile properties that are comparable to those of counterparts processed by conventional metallurgical routes, as shown in Fig. 2.14. It is worth mentioning, however, that the tensile properties of the AM-ed HEA CrMnFeCoNi were reported to span a wide range (yield strength: 200 – 600 MPa; uniform elongation: 20 – 60%) in different open publications [115-120]. This suggests that different printing parameters used in different studies lead to varied microstructures (e.g. grain size). All of these findings indicate that the metallurgy related to the AM process plays an important role in the final AM-ed HEAs. However, relevant investigations are significantly lacking.

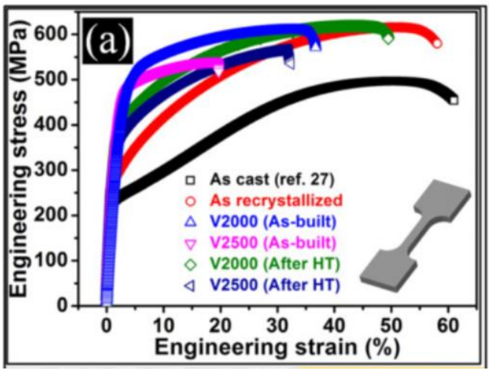

Fig. 2.14 The engineering stress-strain curves of the CrMnFeCoNi with different conditions [112].

Furthermore, the strength-plasticity trade-off of the AM-ed HEAs is still a big problem to resolve. Take CrMnFeCoNi for example, it is the most researched AM-ed HEA up to now. Although it has been printed successfully in some cases with a good combination of strength and ductility that compares to those of wrought-annealed counterparts [112, 113, 117, 120, 179], AM-ed CrMnFeCoNi alloys are basically ductile but not very strong. It should be noted that some refractory HEAs with high-strength and low-plasticity have been also printed. For example, Moorehead et al. [208] synthesised a series of refractory Mo-Nb-Ta-W HEAs via a high-throughput AM process and confirmed their single-phase disordered BCC structures. Similarly, Dobbelstein et al. [204] synthesised a compositional graded refractory HEAs from $Ti_{25}Zr_{50}Nb_{0}Ta_{25}$ to $Ti_{25}Zr_{0}Nb_{50}Ta_{25}$. However, the mechanical behaviour was not studied in both studies. Kunce et al. [122, 209] also additively manufactured several refractory HEAs, e.g. ZrTiVCrFeNi and TiZrNbMoV, but focused on their hydrogen storage properties only. Furthermore, the AlCoFeNiSmTiVZr HEA system has been also printed by the SLM process, but the research focused on the corrosion behaviour studied, with both experimental examination and first principles based calculations [203]. Overall speaking, achieving AM-ed HEAs with a good strength-plasticity synergy is still a challenging task.

2.6 Conclusions

In this chapter, a systematic literature review on the topic of this project was undertaken. Special focus was given to (i) birth, definition and characteristics of HEAs, (ii) typical microstructures and phase formation rules, (iii) mechanical behavior, (iv) manufacturing routes, (v) AM process and several related fundamental research problems and (vi) AM processing of HEAs. In the following chapters, the methodologies, results and discussions are presented.

Chapter 3 Methodology

3.1 Overview

This chapter introduces the common methodologies used in project. Section 3.1 gives an overview, and Section 3.2 introduces the AM facility, i.e. OPTOMEC LENS^{TM} MR-7 System, and printing parameters. Section 3.3 introduces the microstructural and mechanical characterization techniques. Section 3.4 introduces the thermodynamic calculation methods.

3.2 Manufacturing of specimens

3.2.1 OPTOMEC LENS^{TM} MR-7 System

In this project, all the specimens were printed on the platform of the OPTOMEC LENS^{TM} MR-7 System, as shown in Fig. 3.1. This system integrates a high-powered laser system, a powder-feeding line and a computer-controlled motion system. The high-powered laser at a wavelength of 1070 to 1080 nm is delivered through a laser fiber and then through a collimating optic and finally into the system. The high-powered laser beam is directed to the workpiece through a focusing lens mounted in the deposition head (component 7 in Fig. 3.1). The deposition head can be more clearly seen in Fig. 3.2. The typical laser spot size is approximately 600 μm. This machine is also equipped with a pneumatic powder delivery system. The powder delivery line consists of several powder hoppers (component 5 in Fig. 3.1) and a computer-controlled motor inside each hopper. The powder is injected from the powder hopper to the deposition head through the powder delivery line, and finally into the laser-created melt pool. The laser beam focal plane and powder convergence plane are aligned to remain coincident. The motion of the stage (component 8 in Fig. 3.1) enables the deposition of a thin layer, and the motion of the deposition head allows for the continual deposition, layer upon layer. Overall speaking, the LENS^{TM} processing starts with a CAD model, then the slicing up of the model, and finally transmitting the sliced model to a computer controlled manufacturing system. Through this way, a component can be fabricated layer by layer.

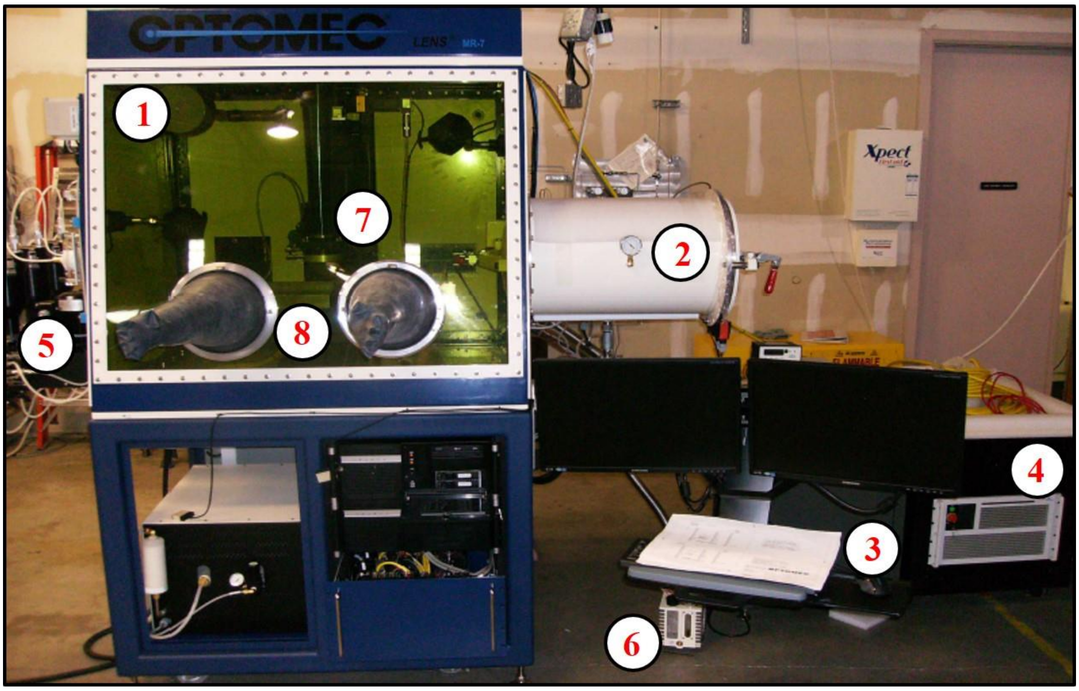

Fig. 3.1 OPTOMEC LENS^{TM} MR-7 System. 1: controlled-atmosphere process chamber; 2: antechamber; 3: Dri-Train; 4: laser control; 5: powder hopper; 6: vacuum pump; 7: four-jet deposition head; 8: stage.

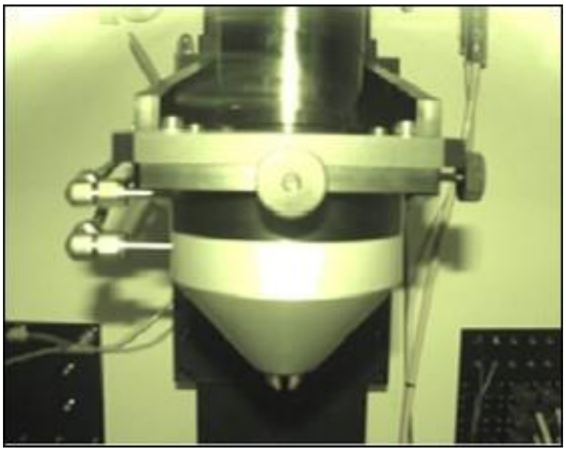

Fig. 3.2 Four-jet deposition head.

The whole manufacturing process is performed in an ultra-high-purity argon gas purged chamber to minimize any potential oxidation. The controlled-atmosphere process chamber (component 1 in Fig. 3.1) is integrated with a Dri-Train (component 3 in Fig. 3.1) which consists of an oxygen and moisture getter as well as a blower. The Dri-Train can be more clearly seen in Fig. 3.3. The argon gas is drawn out of the process chamber and passed over the getter. The getter absorbs the O_2 and H_2O and returns the clean argon gas to the controlled-atmosphere process chamber. For protective purposes, the system is also equipped with a viewing window which blocks the laser at a wavelength of 1070 to 1080 nm.

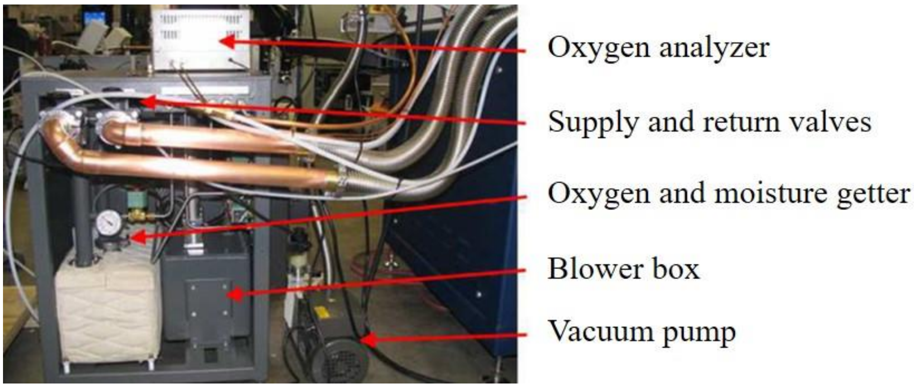

Fig. 3.3 Dri-Train mainly consisting of an oxygen and moisture getter and a blower.

Furthermore, the OPTOMEC LENS^{TM} MR-7 System incorporates a two-wavelength imaging pyrometer located at the top of the system which enables the measurement of temperatures within the melt pool. The two-color or ratio pyrometer measures in two spectral ranges simultaneously and determines the temperature by calculating the radiation ratio. The imaging pyrometer is calibrated using a high-temperature tungsten filament before use, and can provide real-time (25 frames/second) and high resolution (12.1 μm/pixel) temperature measurements over a wide range of temperatures from 1273 to 3073 K. This allows calculation of the temperature gradients and cooling rates. It should be noted that the temperature gradient and cooling rate are two important factors since they determine the as-solidified microstructures formed during the AM process. The schematic of the LENS^{TM} MR-7 system is shown in Fig. 3.4.

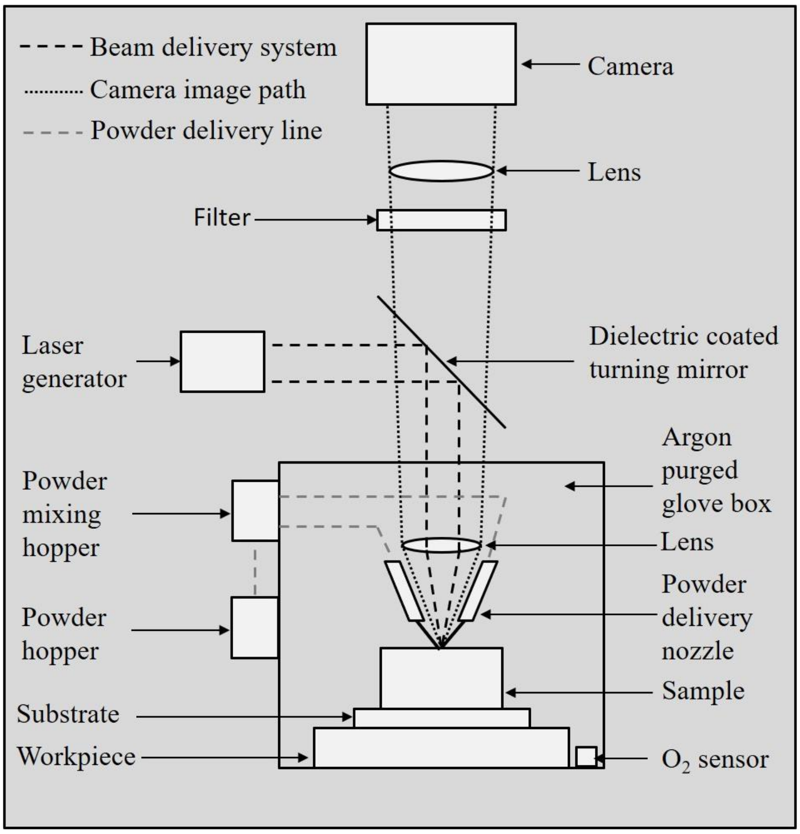

Fig. 3.4 Schematic of the LENS^{TM} MR-7 System.

3.2.2 LENS^{TM} manufacturing

In this project, specimens of CrCoNi, CrMnFeCoNi, AlCoCrFeNiTi$_{0.5}$ and CrMnFeCoNi/AlCoCrFeNiTi$_{0.5}$ were manufactured by the OPTOMEC LENS^{TM} MR-7 System. A total of three prealloyed powders were used in this project: CrCoNi, CrMnFeCoNi and AlCoCrFeNiTi$_{0.5}$ powders. Among them, the CrCoNi and CrMnFeCoNi prealloyed powders were manufactured by the plasma rotating electrode process (PREP), and the AlCoCrFeNiTi$_{0.5}$ prealloyed powders were manufactured by inert gas atomization (GA). Fig. 3.5 shows the SEM images of these three prealloyed powders. It can be seen that the as-manufactured PREP powders are perfectly spherical in shape and are without any satellites, suggesting good flowability (Fig. 3.5 (a) and (b)). The surfaces of the powders are very clean, indicating no oxidation. By contrast, some satellite powders were occasionally observed on the surface of the GA powders (Fig. 3.5 (c)), and their formations are attributed to the welding of smaller particles to larger ones during the flight collision [210]. The particle sizes of these powders were in the range of 50~150 μm, which was in fairly good agreement with the particle size range specified by the LENS^{TM} system.

The above-mentioned powders were used to manufacture specimens on the platform of the LENS^{TM} MR-7 system. Each layer was scanned in a zigzag (bidirectional) way. After one layer was completed, a vertically upwards step of the deposition head was used to scan the next layer, with the scan direction rotated by 90° (cross-hatched). The bidirectional and cross-hatched scan strategy is schematically shown in Fig. 3.6. More details regarding the materials preparation procedures are presented in the respective chapters.

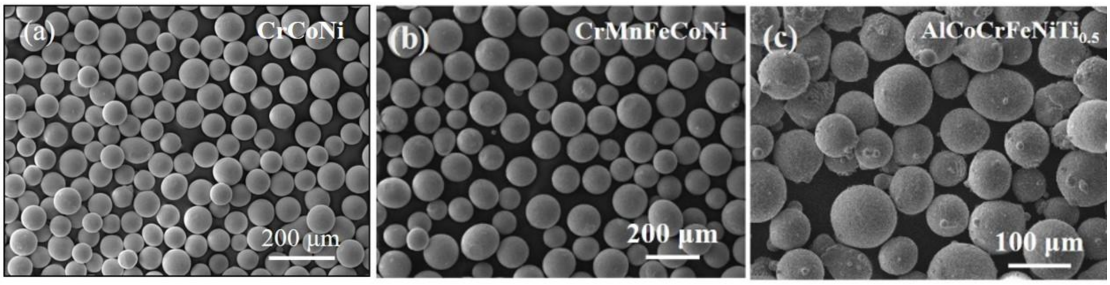

Fig. 3.5 SEM images of (a) CrCoNi, (b) CrMnFeCoNi and (c) $AlCoCrFeNiTi_{0.5}$ prealloyed powders. The CrCoNi and CrMnFeCoNi powders were manufactured by the PREP process, and the $AlCoCrFeNiTi_{0.5}$ powders were manufactured by the GA process.

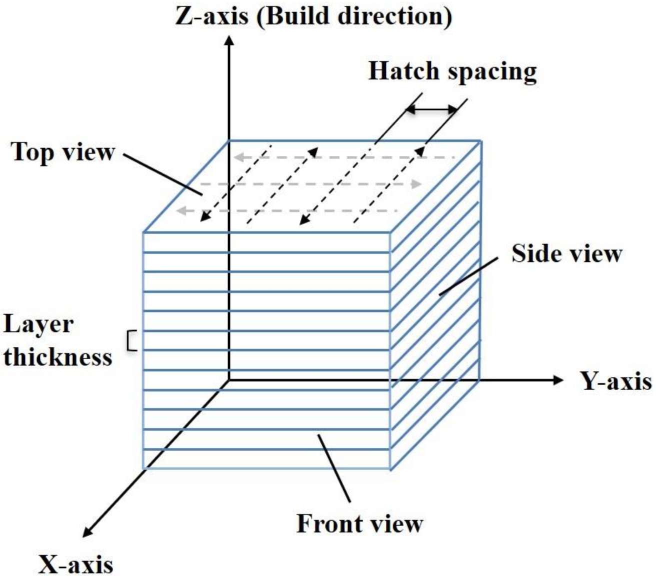

Fig. 3.6 Schematic of the bi-directional and cross-hatched scan strategies. The coordinate system (i.e. X-, Y-, and Z-axis), and the three cross-sections (i.e. top, front and side views) are indicated. The black and gray broken arrows represent the laser scan directions for two consecutive layers, showing the bidirectional and cross-hatched scan strategy used in this study. Furthermore, the layer thickness and the hatch spacing are also schematically shown.

3.3 Microstructural and mechanical characterization

Several microstructural and mechanical characterization techniques were used to study the LENS^{TM}-processed HEAs. These microstructural characterization techniques include X-ray computed tomography (X-ray CT), X-ray diffraction (XRD), optical microscopy (OM), scanning electron microscopy (SEM), energy dispersive X-ray spectroscopy (EDS), electron backscatter diffraction (EBSD) and electron channeling contrast imaging (ECCI). The X-ray CT was performed on the platform of YXLON FF35 CT System in a dual-tube configuration. The tube voltage and tube current were 150 kV and 60 μA, respectively. During the X-ray CT scan, the specimen was rotated from 0 ~ 360° in increments of 0.2°, and hence a total of 1800 projections were generated in a full rotation, and were reconstructed to visualize the internal defects down to 3 μm. For determination of the phase constitution, the XRD measurement was performed on a Rigaku SmartLab X-ray diffractometer, with Cu Kα radiation scanning from 30 to 100 degrees at a scan rate of 5 degrees per minute. The examination surface for the XRD measurement was the XY-plane. Microstructural investigations, through SEM, EDS, EBSD and ECCI, were also performed on the LENS^{TM}-processed HEAs. The color legend indicating the correspondence between the colors in the EBSD inverse pole figure (IPF) map and the crystallographic orientations is shown in Fig. 3.7. The SEM (secondary electron imaging, SE; backscattered electron imaging, BSE), EDS and EBSD characterizations were performed in a Quanta 650 SEM (Thermo Fisher Scientific Inc., USA) at an acceleration voltage of 20 kV, while the ECCI investigation was performed in the same microscope but with an increased acceleration voltage of 30 kV. Samples for SEM, EDS, EBSD, and ECCI investigations were cut from the LENS^{TM}-deposited specimen by electrical discharge machining (EDM), and then successively ground with emery paper up to 4000 grit size, and finally polished with diamond suspension and colloidal silica-based slurry down to 0.05 μm particle size.

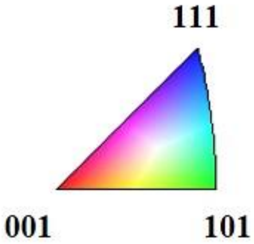

Fig. 3.7 The color legend indicating the correspondence between the colors in the EBSD IPF map and the crystallographic orientations.

Additionally, mechanical tests, including Vickers hardness tests, compressive tests and tensile tests, were also carried out. The Vickers hardness test was performed on the polished surface under a load of 500 g for 15 s. An average value of at least five indentations on each sample was used. Both tensile and compressive tests were carried out on a servo-hydraulic 810 Material Test System (MTS) at room temperature. Rectangular dog-bone shaped specimens, for tensile testing, were machined from the LENS^{TM}-deposited specimen, with their longitudinal axes (i.e. tensile axis) along the X direction. Compressive test samples were machined from the LENS^{TM}-processed HEAs, with the compressive axis parallel or perpendicular to the build direction.

3.4 Thermodynamic calculations

3.4.1 Philosophy: minimum Gibbs free energy

The CALculation of PHAses Diagrams (CALPHAD) approach is based on the minimum Gibbs free energy principle. For a specific alloy system, the Gibbs free energy of each phase is described by a mathematical model that is a function of several state variables, e.g. temperature, pressure, composition, thermal expansivity, molar volume, heat capacity and entropy. The sum of the total Gibbs free energy of each phase is the Gibbs free energy of the alloy system. With the CALPHAD method, we can calculate the phase formation, phase fraction and phase composition for a specific alloy system. The reliability of CALPHAD calculation lies in the reliable description of Gibbs free energy of all possible phases and the reliable settings of the multiple state variables. In this project, the CALPHAD calculation was performed on the platform of the Thermo-Calc software that is a sophisticated package used to perform thermodynamic calculations. Furthermore, we use the TCHEA thermodynamic database that is newly developed for HEAs and provides more reliable thermodynamic parameters.

3.4.2 TCHEA thermodynamic database

TCHEA is a thermodynamic database for HEAs and is developed within a 20-element framework including Re, Ti, V, Ta, Mo, Mn, Cr, Fe, Al, C, N, Co, Hf, Nb, Cr, Ni, W, Zr, Si and Ru. All binary and 135 ternary systems within this 20-element framework are evaluated to the full range of temperatures and compositions. Furthermore, 308 ternary systems are tentatively assessed. TCHEA includes nearly all possible stable phases and 266 intermetallic and solid solution phases. TCHEA can be extrapolated to higher-order systems (HEAs) and hence can help to predict the formed phases of HEAs.

3.4.3 Scheil simulation

Thermo-Calc is primarily used to perform equilibrium calculations that assume infinite diffusion in both the liquid and solid phases. These calculations benefit in the prediction of the equilibrium microstructures of HEAs. However, the rapid quenching effects associated with the AM process may result in microstructures that deviate significantly from the equilibrium microstructures. Fortunately, in addition to equilibrium calculations, the Scheil Calculator in the Thermo-Calc software allows us to perform simulations of Scheil (or Scheil-Gulliver) solidification processes. The Scheil solidification processes are simulated based on three assumptions: (i) equilibrium exists at the liquid-solid interface; (ii) infinite diffusion occurs in the liquid, i.e. the liquid is homogeneous at all times; (iii) no diffusion occurs in the solid. The Scheil solidification simulation results in an estimation of the solidification range and solidification sequence of HEAs. This is beneficial to the prediction of the as-solidified microstructures of HEAs formed during the AM process.

Chapter 4 Microstructural evolution and cracking behavior of a ternary equi-atomic CrCoNi alloy produced using laser engineered net shaping

4.1 Introduction

Chapter 2 indicates that the additive manufacturing (AM) process has shaping and microstructure advantages over conventional metallurgical routes, and in addition to some commercial alloys [15, 211-214], the AM process has recently been used for manufacturing high entropy alloys (HEAs) [29, 52, 106-126, 200-202, 204]. Based on the sparse existing literature on the AM processing of HEAs [115-120], chapter 2 also indicates that different printing parameters may lead to varied microstructures (e.g. grain size, etc.) and mechanical properties of HEAs, and that the cracking susceptibility of HEAs also needs to be paid attention. Until now, relevant investigations on these problems are very much lacking.

In this chapter, we performed a systematic study on the microstructural evolution and cracking behavior of a ternary equiatomic CrCoNi alloy (also referred to as medium entropy alloy, MEA) during the AM process. The CrCoNi alloy is a good starting point for research because of its simpler compositions as compared to those of HEAs. Furthermore, the research outcomes are predicted to provide guidelines for screening process parameters and achieving desirable microstructures of HEAs. By varying laser scan speeds, melt pool solidification behavior and solidification microstructures can be studied. Furthermore, the cracking mechanism for the CrCoNi alloy during the AM process is elucidated.

4.2 Experimental

4.2.1 Materials preparation

CrCoNi prealloyed powders were used to manufacture a series of cuboid specimens (8 mm by 8 mm by 8 mm) using the bidirectional and cross-hatched scan strategies on the platform of the LENS^{TM} MR-7 system. The LENS^{TM} processing parameters, including Z increment t, hatch spacing h and laser power P, were kept constant for these cuboid specimens, as summarized in Table 4.1. The laser scan speed V_b (10, 30 and 50 mm/s) was varied to study its effects on the metallurgy, and the corresponding specimens were designated as V_{10}, V_{30} and V_{50} specimens. During the fabrication of the cuboid specimens, the melt pool was continuously monitored by the ThermaViz system which incorporates a two-wavelength imaging pyrometer as well as image acquisition and analysis software. More details regarding the materials preparation are given in chapter 2.

Table 4.1 The LENS^{TM} processing parameters used for the CrCoNi alloys in this chapter.

Processing parameters	Values (units)
Z increment (t)	102 (μm)
Hatch spacing (h)	457 (μm)
Laser power (P)	400 (W)
Laser scan speed (V_b)	10, 30 and 50 (mm/s)
Scan strategy	Bidirectional and cross hatched

4.2.2 Material characterization and thermodynamic calculations

In order to study the pores and the cracks, the LENS^{TM}-processed cuboid specimens were cut along the YZ-plane, ground, polished and then examined by a Leica optical microscope. For determination of the phase constitution, X-ray diffraction (XRD) measurement was performed. To reveal the grain morphology, the electron backscatter diffraction (EBSD) measurement was performed on the polished YZ-plane. Scanning electron microscopy (SEM) was used to examine the microstructural features, e.g. melt pool boundaries, grain boundaries and solidification substructures. In order to visualize these microstructural features, the specimens were electrolytically etched in a solution of 10 mL HNO_3 + 5 mL $C_2H_4O_2$ +85 mL H_2O. To reveal the crystallographic defects (e.g. dislocations and stacking faults), the LENS^{TM}-processed specimen was characterized by the electron channeling contrast imaging (ECCI) technique. In addition to these experimental characterizations, the solidification behavior (e.g. phase formation) of the CrCoNi alloy was simulated by the CALPHAD (CALculation of PHAse Diagram) method, on the platform of Thermo-Calc software 2019a equipped with TCHEA v2.1.1 thermodynamic database.

4.3 Results

4.3.1 Metallurgical defects

The optical micrographs of the CrCoNi alloy deposited at various laser scan speeds V_b are shown in Fig. 4.1. It can be seen from these micrographs that spherical pores are formed in the V_{10} and V_{30} specimens. Furthermore, in the V_{30} specimen a crack is formed. In contrast, the formation of such spherical pores is obviously suppressed in the V_{50} specimen, but the cracking phenomenon is much more pronounced. The observed spherical pores in this study are not lack-of-fusion defects that were reported to be several hundred micrometers large, irregular and site-specific (i.e. at inter-track and inter-layer locations) [180, 181]. In this study, these spherical pores are believed to be gas pores in nature, and may originate from the gas pores in the starting powders [182] and the occasional vaporization of surface materials [183]. Obviously, the increase in the laser scan speed leads to a lower heat input and hence reduces the probability of surface vaporization. This is believed to be the main reason for the reduced gas pores in the V_{50} specimen. As compared to the gas porosity, the cracks are more critical defects in this study that run several hundred micrometers. The cracking phenomenon is discussed in section 4.4.2 in detail.

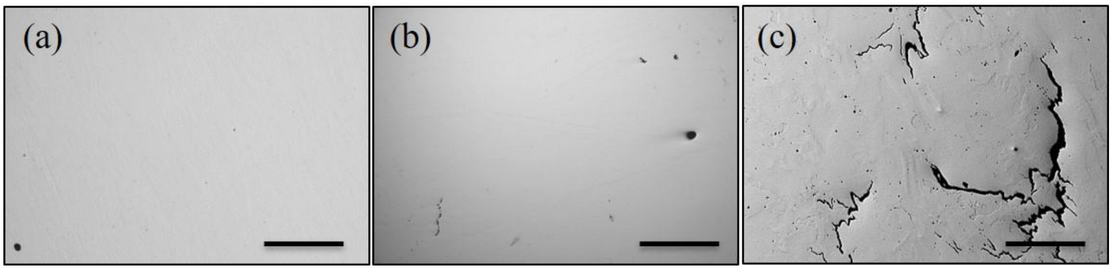

Fig. 4.1 Optical micrographs of the CrCoNi specimens processed at (a) 10, (b) 30 and (c) 50 mm/s. The scale bars are 300 μm.

4.3.2 Phase formation

The XRD patterns in Fig. 4.2 suggest that the LENS^{TM}-processed CrCoNi alloys are characterized by a single-phase FCC microstructure, which is in good agreement with their counterparts processed by conventional routes [24]. Such a simple single-phase microstructure can be discussed with the aid of the thermodynamic calculations, as shown in Fig. 4.3. Under the assumption of the infinite diffusion of all the elements in both the solids and liquids (i.e. equilibrium solidification), only FCC phases solidify from the melt, i.e. L → L + FCC → FCC. This is also true for Scheil-Gulliver solidification that assumes the infinite diffusion of all the elements in the liquid and no diffusion of all the elements in the solid. However, Scheil-Gulliver solidification overestimates the effect of micro-segregation and hence predicts a lower solidus temperature, i.e. 1678 K for Scheil-Gulliver case vs. 1707 K for equilibrium case.

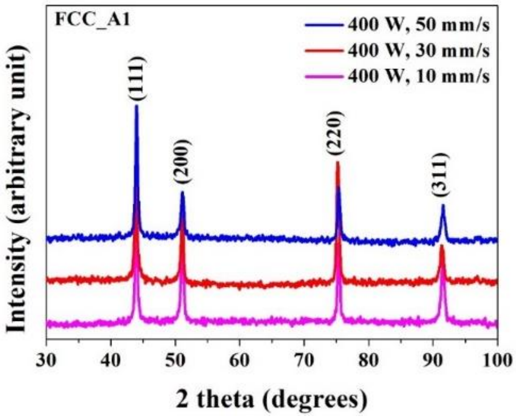

Fig. 4.2 XRD patterns of the CrCoNi specimens processed at various laser scan speeds. Only FCC peaks are indexed.

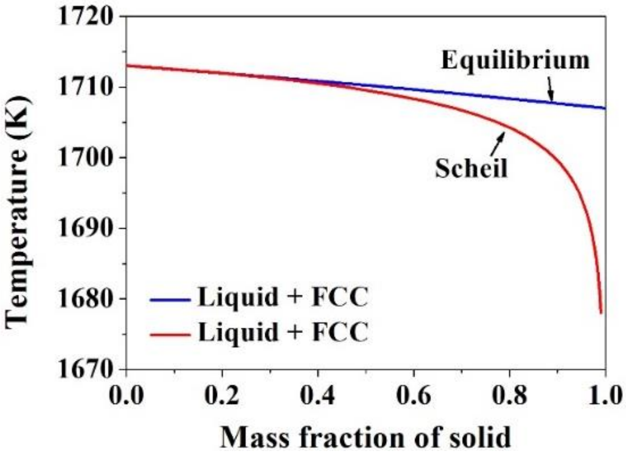

Fig. 4.3 Thermodynamic prediction of the solidification path of the CrCoNi alloy based on both equilibrium and Scheil-Gulliver assumptions.

4.3.3 Microstructure formation

Fig. 4.4 shows the EBSD IPF, image quality (IQ) and kernel average misorientation (KAM) maps of the V_{10} and V_{50} specimens, with the examination surface being the YZ-plane (Y-axis aligned horizontally; Z-axis, i.e. build direction, aligned vertically). The high angle grain boundaries (HAGBs, >15°, in black) and low angle grain boundaries (LAGBs, 2° – 15°, in blue) are highlighted in the IPF and IQ maps. For the KAM maps, only HAGBs (in black) are highlighted. It can be observed from the IPF map in Fig. 4.4 (a) that the grain structure, delineated by HAGBs, is overall columnar in the front view of the V_{10} specimen. The longitudinal axes of these elongated grains deviate from the build direction and are along various directions. Furthermore, the longitudinal axes of some grains rotate 90° at certain locations. The growth directions of these elongated grains can be discussed in terms of the melt pool boundaries. In the IQ map (Fig. 4.4 (b)), the melt pool boundaries are superimposed by the black broken lines. It should be noted that the melt pool boundaries are occasionally visible but not always clearly identifiable in the IQ map. Therefore, the V_{10} specimen was etched after EBSD characterization in order to reveal the melt pool boundaries. It can be clearly seen from the IQ map in Fig. 4.4 (b) that the elongated grains grow across the melt pool boundaries, suggesting an epitaxial growth mode. Furthermore, the longitudinal axes are approximately perpendicular to the local melt pool boundaries, i.e. approximately along the maximum heat flux direction. The rotation of the longitudinal axes occurs only when the grains run across the melt pool boundaries and their old longitudinal axes obviously deviate from the normal of the local melt pool boundaries. A typical columnar grain that rotates 90° is marked by red arrows in Fig. 4.4 (b). In contrast, the grain structure of the V_{50} specimen is much more heterogenous. Both columnar and equiaxed grains can be observed in the front view (Fig. 4.4 (d) and (e)). Elongated and equiaxed grains are formed alternately, as marked in Fig. 4.4 (e). These elongated grains form a convergent pattern (i.e. towards a centerline). In the adjacent area, the grains seem equiaxed for the current view.

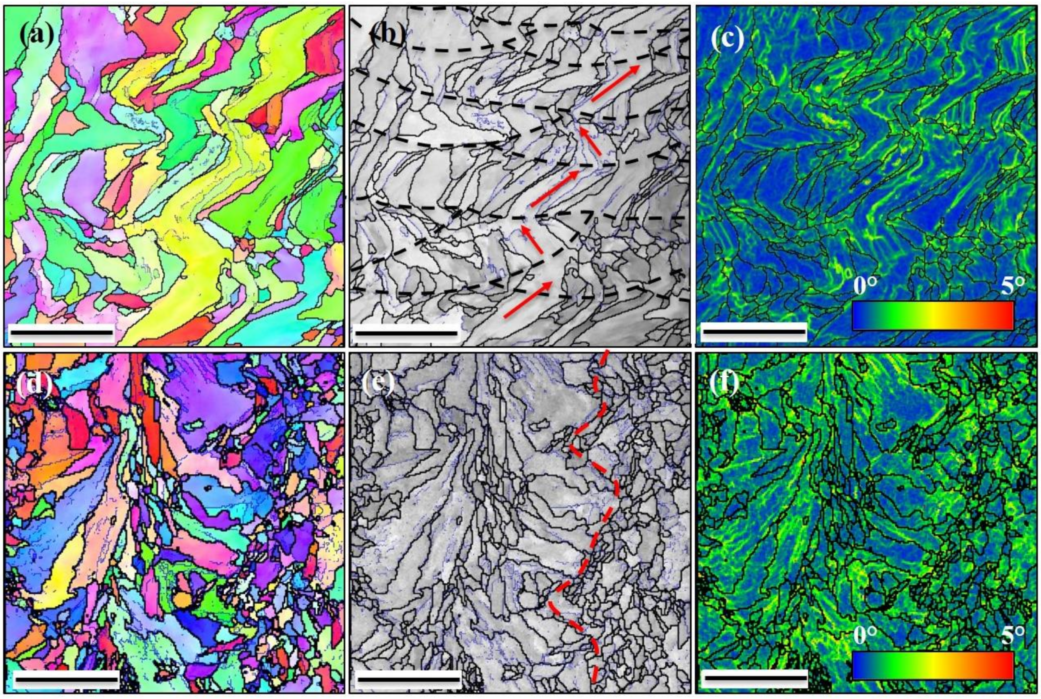

Fig. 4.4 EBSD characterization of the (a) – (c) V_{10} and (d) – (f) V_{50} specimens (front view). (a) and (d) are IPF maps, (b) and (e) are IQ maps, and (c) and (f) are KAM maps. In the IPF and IQ maps, the HAGBs and LAGBs are highlighted in black and in blue, respectively. In the KAM maps, only the HAGBs are highlighted. The black dashed lines in (b) represent the melt pool boundaries. A typical columnar grain that rotates 90° is marked by red arrows in (b). In the front view, the grains exhibits both columnar and equiaxed morphologies, as marked in (e). The reference axis for the IPF maps is the Z-axis that is aligned vertically upwards. All the scale bars are 300 μm.

Furthermore, it should be noted that the grains in the IPF maps are colored based on their orientations with respect to the build direction (Fig. 4.4 (a) and (d)). A continuous color change and thus a local misorientation are frequently observed within individual grains, especially across the LAGBs (sub-grain boundaries). The local misorientation is directly evidenced in the KAM maps, as shown in Fig. 4.4 (c) and (f). By comparing the IPF and KAM maps, a more direct correlation between the misorientation and the LAGBs is confirmed. More specifically, the formation of the LAGBs introduces a large local misorientation. This is reasonable because the sub-grains grow together to form a single grain by the introduction of a LAGB. Such a growth process leads to a larger misorientation at LAGBs than in other regions within individual grains. In this study, the total lengths of the LAGBs in the V_{10} and V_{50} specimens were measured to be ~ 15 and 33 mm, respectively, in an equal investigated area of 1 mm by 1 mm. The much denser LAGBs in the V_{50} specimen inevitably leads to a more frequent local misorientation, as compared to the V_{10} specimen (Fig. 4.4 (c) and (f)).

To study the intragrain microstructural features, the V_{10} and V_{50} EBSD specimens were electrolytically etched and then examined by OM and SEM, and the micrographs are shown in Fig. 4.5. The jagged grain marked by red arrows in Fig. 4.4 (b) is also included in Fig. 4.5 (a) and is shown in Fig. 4.5 (b) at higher magnifications. It is clear that the intragrain solidification substructures are basically cellular, and these cellular structures may rotate by 90 degrees when encountering the melt pool boundaries. Furthermore, the rectangular region in Fig. 4.5 (b) is within a single grain although it comprises two celluar structures (Fig. 4.5 (c)). These two cellular structures can be attributed to different view angles. In contrast, the V_{50} specimen exhibits adjacent columns of melt pools, with one columnar and one equiaxed (Fig. 4.5 (d)). The intragrain solidification substructures are also cellular, but much finer as compared with those in the V_{10}

specimen (Fig. 4.5 (e) and (f)). The origin of the microstructure scale is discussed in section 4.4.1.

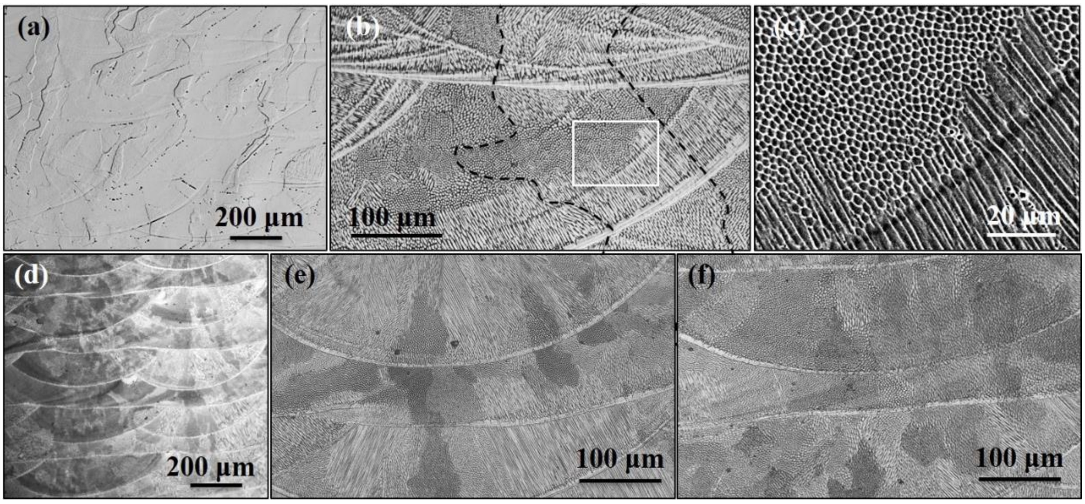

Fig. 4.5 Micrographs of the (a) – (c) V_{10} and (d) – (f) V_{50} specimens, relating the grain structure to the melt pool solidification. (c) shows the characteristics of the rectangular area in (b).

The laser scan speed also influences the formation of the crystallographic defects, as can be observed from the typical ECCI images in Fig. 4.6. The V_{10} specimen contains discrete dislocations (Fig. 4.6 (a)), and in contrast the dislocations in the V_{50} specimen are much denser (Fig. 4.6 (b)). Two slip traces are clearly shown, forming an angle of 60 degrees. Furthermore, stacking faults are frequently observed in the V_{50} specimen, as marked by the white arrows in Fig. 4.6 (b). Such a high density of crystallographic defects originates from the plastic strain, suggesting the presence of the residual stress in the final specimen. The residual stress in the AM-ed parts is frequently reported, and has been attributed to the thermal stress introduced during solidification and subsequent cooling [119]. Obviously, the much denser dislocations plus the formation of the stacking faults in the V_{50} specimen indicate a much higher thermal stress induced during the LENS^{TM} process.

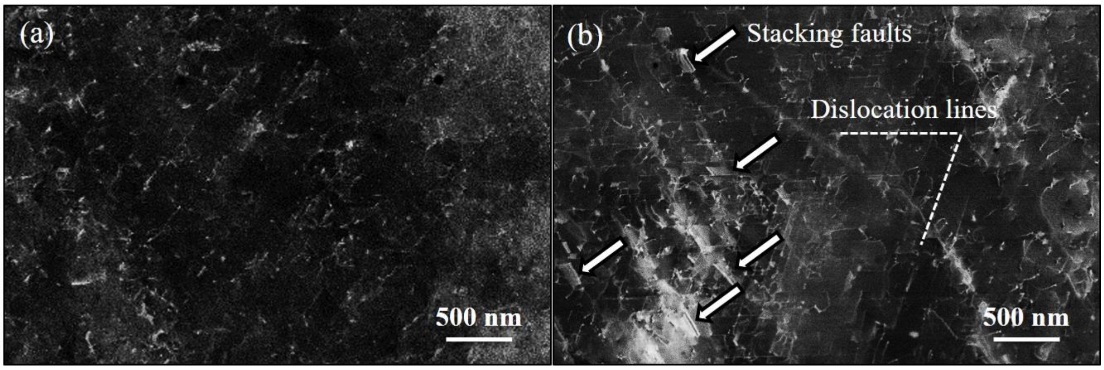

Fig. 4.6 ECCI images of the (a) V_{10} and (b) V_{50} specimens, showing the crystallographic defects. Stacking faults and denser dislocations were observed in the V_{50} specimen. Two slip traces are formed with an angle of 60 degrees, as indicated by the broken white lines in (b). The stacking faults are also indicated by the arrows in (b).

4.4 Discussion

4.4.1 Origin of variation in microstructural scale

The imaging pyrometer on the LENS^{TM} MR-7 system in-situ measures the temperature in the vicinity of the melt pool, as shown by the two-dimensional color-coded thermal image in Fig. 4.7 (a). The whole melt pool can be roughly divided into two halves by the melt pool center (approximately the hottest point at the peak temperature). For the present case, the left half is heating and the right half is cooling. In this study, we focus more on the tail of the melt pool, which not only cools but also solidifies. In order to determine the temperature gradient and the cooling rate at the tail of the melt pool, the temperature profile corresponding to the cooling half is extracted from the thermal image along the black line (i.e. laser scan direction) in Fig. 4.7 (a). The temperature gradient and cooling rate (i.e. the product of the temperature gradient and laser scan speed) vary in the melt pool, and we focus on those values at the tail of the melt pool, as shown in Fig. 4.7 (b) and (c).

Calculations of the temperature gradient and cooling rate were also performed for the V_{30} and V_{50} specimens, and the effect of the laser scan speed on the temperature gradient and cooling rate is summarized in Fig. 4.7 (d). The increase of the laser scan speed leads to the increase of the temperature gradient and the cooling rate. Furthermore, it should be noted that the cooling rate is estimated to be as high as 10^4 K/s, which may prohibit the formation of secondary and ternary arms and hence promote the formation of the observed cellular substructures (Fig. 4.5 (c)). Similar findings have been also reported in Ref. [137].The cellular spacing λ decreases with the increase of the laser scan speed V_b (Fig. 4.7 (e)). Such a tendency is attributed to the variation in the cooling rate, which is clearly shown in Fig. 4.7 (f). The cellular spacing decreases as the cooling rate increases. Many conventional alloys (e.g. steels) also show a similar trend during the AM process [137, 215], and by fitting the experimental data in this study, a new equation $\lambda = 8.81 \cdot (CR)^{-0.13}$ describing the quantitative relationship between the cellular spacing λ (µm) and the cooling rate CR (K/s) was established for the CrCoNi alloy.

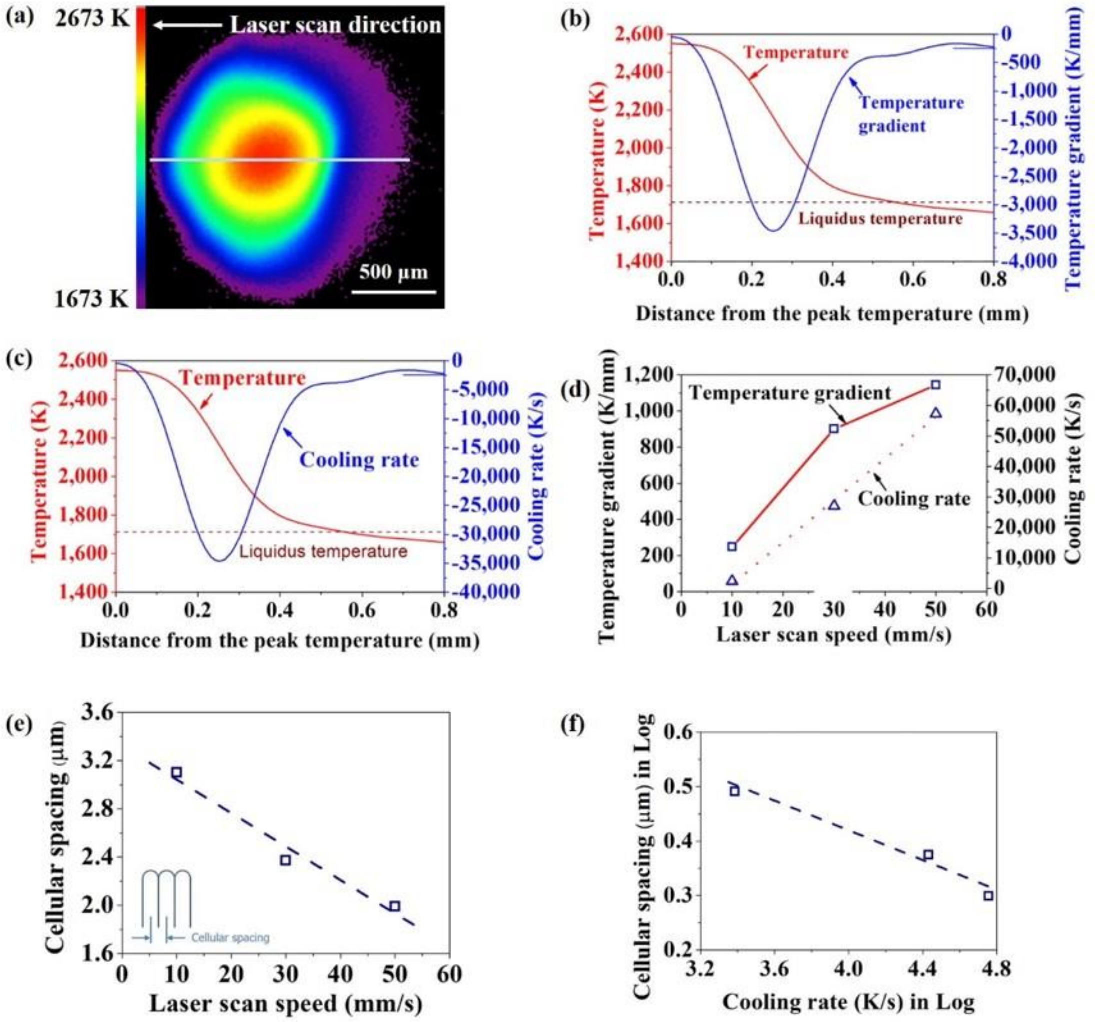

Fig. 4.7 (a) Typical color-coded thermal image for the V_{10} specimen. (b) Estimation of the temperature gradient at the mushy zone for the V_{10} specimen. (c) Estimation of the cooling rate at the mushy zone for the V_{10} specimen. (d) Temperature gradient and cooling rate plotted against the laser scan speed. (e) Effect of laser scan speed on the cellular spacing. (f) Correlation of the cellular spacing with the cooling rate.

4.4.2 Cracking mechanism

4.4.2.1 Cracking characteristics

It has been observed from Fig. 4.1 that the cracking phenomenon is very frequent in the V_{50} specimen, with several hundred micrometers long cracks running in various directions. To further understand the cracking behavior, the cracked region of the V_{50} specimen was examined by EBSD, and the result is shown in Fig. 4.8. It can be seen that the cracks propagate along the HAGBs, i.e. these cracks are intergranular (Fig. 4.8 (a)). In contrast, the LAGBs and the sub-grain interior remain uncracked. Such a phenomenon suggests that the HAGBs are more sensitive to cracking. Due to the unique grain growth behavior in the V_{50} specimen, the HAGBs run in various directions and so do the cracks. In the vicinity of the cracks, large plastic deformations were detected (Fig. 4.8 (b)). It should be noted that each alloy has intrinsic (i.e. high or low) susceptibility to cracking. Furthermore, the presence of a sufficiently high thermal stress is an external condition. The combination of these two factors is a necessary condition for cracking, and these two factors are discussed in the subsequent sections.

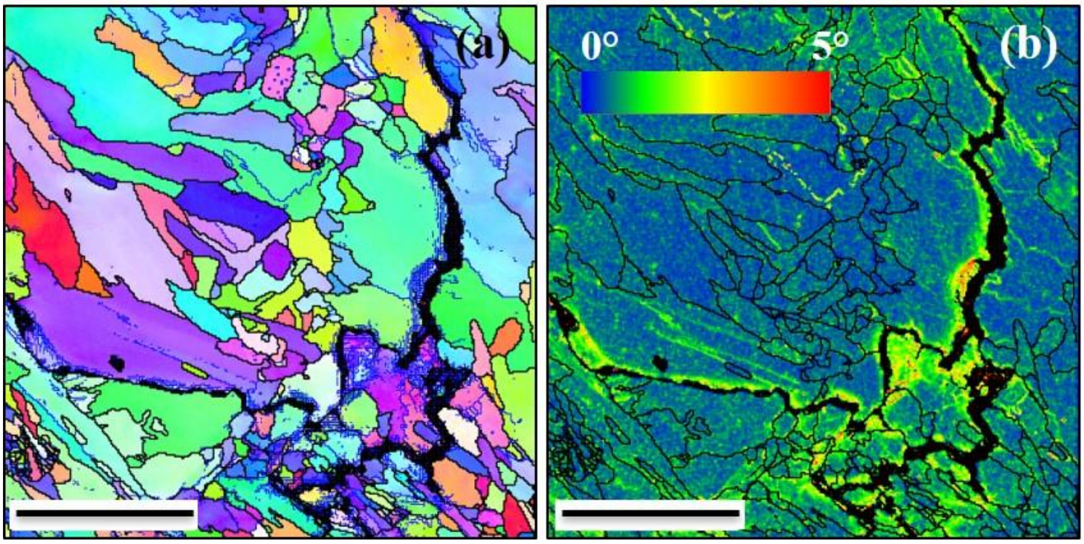

Fig. 4.8 EBSD (a) IPF map and (b) KAM map of a cracked region in the V_{50} specimen (front view). The HAGBs are highlighted in black in both maps. The LAGBs are highlighted in blue in the IPF map. The Z-axis (i.e. the build direction) is vertically upwards, and the Y direction is horizontal. The reference axis for both IPF maps is the build direction. All the scale bars are 200 μm.

4.4.2.2 Origin of cracking

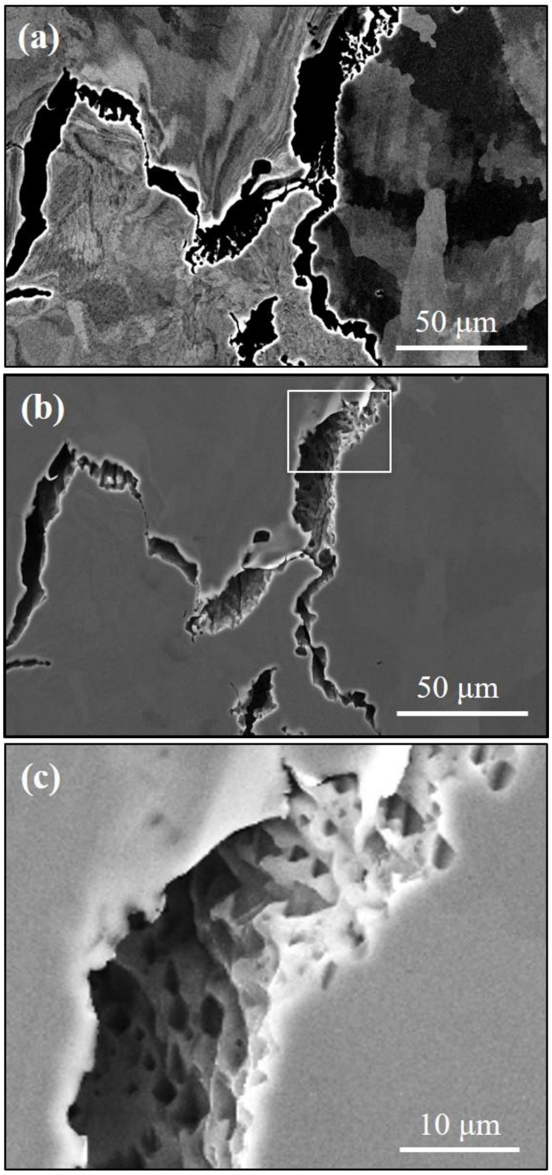

Fig. 4.9 (a) BSE and (b) SE micrographs of a cracked region of the V_{50} specimen. (c) is a magnified view of the characteristics in (b).

Several cracking mechanisms have been reported in the welding and AM literature, e.g. solidification cracking [166, 167], liquation cracking [172-174], ductility-dip cracking [177] and strain-age cracking [175]. Solidification cracking, also known as hot tearing, occurs in the mushy zone of the melt pool at the very last stage of solidification when the dendrites have coalesced and the interdendritic melt can initiate a crack under thermal stress [166, 167]. In contrast, liquation cracking occurs in the heat affected zone, and such cracks typically originate from the liquation of certain low melting temperature phases (e.g. eutectics and carbides) at the grain boundaries [172-174]. Obviously, these two cracking phenomenon occur in the presence of a liquid film. In contrast, ductility-dip cracking and strain-age cracking occur at a fully solid state although these two cracking mechanisms are triggered during different processes. As its name suggests, ductility-dip cracking originates from a significantly reduced ductility that typically occurs in an intermediate temperature range [177]. Such a cracking behavior has been well documented in Ni-based superalloys when cooled down from high temperatures after laser processing. Post ageing heat treatment is occasionally needed, and this leads to the precipitation phenomenon. Although precipitation strengthens the alloys, it normally leads to the decrease in ductility and the increase in stress. Such a combined effect may also cause the cracking phenomenon, i.e. strain-age cracking [175].

In this study, to probe into the cracking behavior, the cracked region of the V_{50} specimen was examined and is shown in Fig. 4.9. Severe deformation was observed in the vicinity of the cracks, indicating a large thermal stress and hence a high strain level (Fig. 4.9 (a)). Furthermore, the cracks were very jagged (Fig. 4.9 (a) and (b)), and a high magnification SEM micrograph in Fig. 4.9 (c) shows that the cracked surface exhibits obvious protruding dendritic structures. These microstructural features lead to the judgement that these intergranular cracks are formed in the presence of a liquid film [216]. In other words, it is only when cracking occurs in the presence of a liquid film that these solidification substructures are retained on the cracked surface. Hence, the two types of solid-state cracking behavior, i.e. ductility-dip cracking and strain-age cracking, could be safely excluded for the present case. As discussed before, the liquation cracking also occurs in the presence of the liquid film, but originates from the liquation of some grain boundary low melting point phases. For example, the IN738 (or IN738LC) superalloy was reported to form multiple phases at the grain boundaries, e.g. MC-type carbides, γ-γ' eutectic, M_3B_2 boride and Ni_7Zr_2 zirconium compound, and the liquation of these phases were found to be the origin of micro-fissuring in the heat affected zone [172-174]. However, the CrCoNi alloy exhibits a simple single-phase FCC solid solution structure, and no traces of liquation were observed in this study. Therefore, liquation cracking can be also excluded. These observations and discussions finally lead us to point to solidification cracking, i.e. hot tearing.

4.4.2.3 Solidification cracking susceptibility

Metals and alloys all exhibit solidification cracking susceptibility to a certain extent, and such a susceptibility can be evaluated by a material constant, i.e. the critical temperature range $\Delta T_{\mathrm{CRT}} = T\ (f_{\mathrm{s}} = 0.95) - T\ (f_{\mathrm{s}} = 1)$. As proposed in Ref. [217], this critical temperature range determines the total strain ε at the very last stage of solidification, according to $\varepsilon = \alpha \cdot \Delta T_{CRT} + 0.05 \cdot \beta^{1/3}$, where α is the thermal expansion coefficient of the alloy and β is volume shrinkage coefficient of the liquid during solidification. Obviously, this equation indicates that a larger ΔT_{CRT} value results in a larger total strain ε occurred at the very last stage of solidification. According to our Scheil solidification simulation result (Fig. 4.3), the CrCoNi alloy solidifies in a very narrow ΔT_{CRT} range of 16 K that is much smaller than those of non-weldable Ni-based superalloys [217] and is comparable to those of 316L stainless steels [201]. Therefore, the CrCoNi alloy should be classified as a weldable/printable alloy, which can be also observed from our good-quality V_{10} specimen. The severe cracking in our V_{50} specimen can be attributed to extreme external conditions, i.e. large temperature gradient and high thermal stress. As can be seen in Fig. 4.7 (d), the increase in laser scan speed dramatically increases the temperature gradient and hence thermal stress. Such a tendency can be also evidenced from the ECCI images of the CrCoNi specimens processed with different laser scan speeds, as seen in Fig. 4.6. When the thermal stress is high enough, it can not only pull but rip the coalescence cells at the very last stage of solidification. As a direct result, solidification cracks form in the V_{50} specimen.

4.5 Conclusions

In this study, the ternary equiatomic CrCoNi alloy was additively manufactured by the LENS^{TM} process with varied laser scan speeds, and special focus was given to the microstructural evolution and cracking behavior. The main conclusions are as follows:

(1) The LENS^{TM}-processed CrCoNi exhibits a single-phase FCC solid solution structure as evidenced by XRD and rationalized by Scheil's solidification simulation. The laser scan speed has no pronounced effects on phase formation.

(2) The increased laser scan speed generates more heterogenous grain structures. To be more specific, the grain structure varies from columnar to columnar plus equiaxed when the laser scan speed increases from 10 to 50 mm/s. Furthermore, the increased laser scan speed achieves more pronounced quenching effects and hence generates finer celluar spacing. A quantitative relationship between the cooling rate and celluar spacing has been established. The increased laser scan speed also generates more dislocations

and promotes the formation of the stacking faults.

(3) The CrCoNi alloy shows a low susceptibility to solidification cracking during the AM process and crack-free CrCoNi alloys can be successfully printed by the LENS^{TM} process. However, the high laser scan speed creates a large thermal gradient and hence a high thermal stress that can still trigger solidification cracking of the CrCoNi alloy. The research outcomes described in this chapter indicate that the selection of the printing parameters is a compromise, which can lead to desirable microstructures (e.g. heterogenous grain structure, fine microstructure scale, etc.) and can also trigger the formation of defects (e.g. cracking, etc.).

Chapter 5 Additive manufacturing of fine-grained and dislocation-populated quinary equi-atomic alloy CrMnFeCoNi by laser engineered net shaping

5.1 Introduction

Chapter 4 reports a thorough study on the microstructural evolution and cracking behavior of a simple ternary equi-atomic CrCoNi alloy during the additive manufacturing (AM) process. The research extends to a quinary equi-atomic high entropy alloy (HEA) CrMnFeCoNi in this chapter [1, 84, 218]. The HEA CrMnFeCoNi exhibits a good fracture toughness of $200\ \mathrm{MPa{\cdot}m^{1/2}}$ at liquid-nitrogen temperature, that is superior to most metal alloys [1]. To date, however, the majority of CrMnFeCoNi alloys are manufactured by casting processes and are therefore dominated by coarse-grained (CG, up to hundreds of micrometers) microstructures that produce low yield stress [116]. To achieve fine-grained (FG, 500 nm to a dozen or so micrometers) microstructures, complex cold forging and/or rolling and subsequent annealing processes are normally needed [1, 84]. Some severe plastic deformation (SPD) techniques (e.g. high pressure torsion, HPT) and mechanical alloying have even been used to prepare the bulk CrMnFeCoNi alloys with ultrafine-grained (UFG, < 500 nm) or even nanocrystalline (NC, < 100 nm) microstructures [9, 91, 219, 220]. The UFG/NC CrMnFeCoNi alloys are strengthened effectively, possibly due to the nanoscale and interfacial effects, but the uniform tensile ductility decreases dramatically below a few per cent, or even approaching zero [219, 220]. Details of the nanoscale and interfacial effects have been discussed in [221]. The reduced ductility can be attributed to the weakened capacity for sustainable work hardening, and thus the early formation of necking that terminates the uniform plastic deformation [221-223]. Overall, a good combination of the tensile yield strength and useful uniform elongation is currently achieved in the FG regime. However, conventional metallurgical routes (e.g. cold-deformation and subsequent annealing) enabling the achievement of FG microstructures are relatively complex. Furthermore, only simple geometries can be achieved, and normally post machining is required. All these disadvantages are intrinsic to these conventional routes, and it is therefore difficult or even impossible to avoid.

The AM process increases the design and manufacturing flexibilities and therefore has great potential for applications in the metal manufacturing industry. Components with complex geometries can be near-net-shaped by the AM process and no post machining is required. Furthermore, dies are not needed for the AM process. In addition to the above-mentioned advantages, the AM process has the potential to achieve uniquely fine as-solidified microstructures due to the rapid cooling effects [147, 224, 225]. This enables the AM process to manufacture complex shaped components and prepare FG microstructures in a single-step, which are not accessible in conventional metallurgical processes. Selective laser melting (SLM), a very popular laser powder-bed-fusion (PBF) AM process, has been used to print the CrMnFeCoNi alloy, with a good combination of strength and ductility [112, 113, 179]. The laser powder-blown AM process has also been employed to manufacture the CrMnFeCoNi alloys. Some of the powder-blown AM-ed CrMnFeCoNi alloys are not strong enough [115, 116, 118], maybe due to the inappropriate processing parameters and thus the coarse microstructures. Recently, a good combination of strength and ductility has been also achieved in the powder-blown AM-ed CrMnFeCoNi alloys [117, 120]. However, a more systematic investigation is needed to better understand the solidification conditions, microstructural formation and tensile behavior of the AM-ed CrMnFeCoNi alloy.

In this chapter, the CrMnFeCoNi alloy was additively manufactured by the laser engineered net shaping (LENS^{TM}) process, that also adopts the powder feeding mechanism. The solidification conditions, phase formation, as-deposited microstructures, and tensile behavior of the LENS^{TM}-deposited CrMnFeCoNi alloy are investigated, and its tensile properties are compared with various CrMnFeCoNi alloys processed by conventional and alternative AM processes. The strengthening mechanisms and the origin of reduced ductility, as compared with the wrought-annealed counterparts, are discussed.

5.2 Experimental

5.2.1 Specimen fabrication by the LENS^{TM} process

A series of small CrMnFeCoNi samples (10 mm by 10 mm by 8 mm) using various process parameters were first additive manufactured. Based on the minimum defects criterion, the following optimum process parameters were determined: a laser power of 400 W, a scan speed of 5 mm/s, a linear heat input (i.e. the applied laser power divided by the laser scan speed) of 80 J/mm, and a hatch spacing of 460 μm. With the above optimized process parameters, a large CrMnFeCoNi specimen (55 mm by 20 mm by 5 mm) was built, as shown in Fig. 5.1. Then dog-bone specimens were obtained by electrical discharge machining (EDM) and polishing, with the gauge dimensions of 10 mm by 3 mm by 0.9 mm. During the fabrication, the melt pool was monitored by the Thermaviz system, which incorporates a two-wavelength imaging pyrometer as well as image acquisition and analysis software. More details regarding the materials preparation are given in chapter 2.

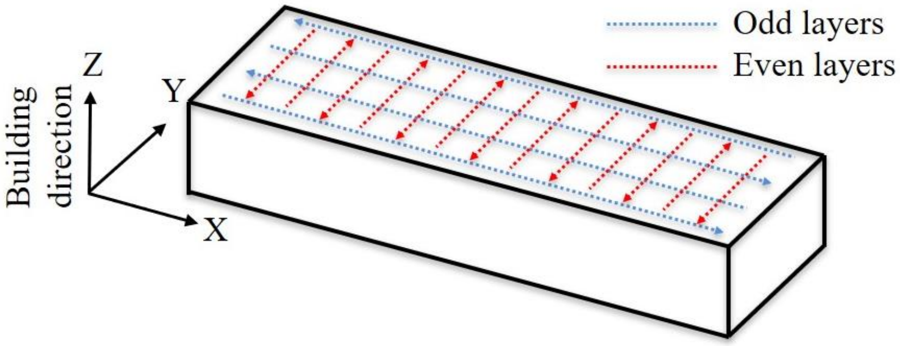

Fig. 5.1 The schematic of the CrMnFeCoNi tensile specimen. The bidirectional and cross-hatched scan strategy was used. The blue and red arrows indicate the laser scan direction for odd and even layers, respectively. The building direction Z is aligned vertically upwards.

5.2.2 Material characterization and thermodynamic calculations

The density of the LENS^{TM}-deposited specimen was measured by the Archimedes method. The internal defects inside the LENS^{TM}-deposited specimen were examined by the dual-tube micro-focus X-ray computed tomography (CT) System YXLON FF35 CT. The residual stress (in-plane stress σ_x) in the LENS^{TM}-deposited specimen was measured on a X-ray diffractometer with a Cr Kα radiation. The diffraction angle 2θ = 128° for the {220} crystal plane family was used to have high diffraction peak, and the residual stress value was calculated by $sin^2\varphi$ method.

The tensile test was carried out on rectangular dog-bone shaped specimens at an engineering strain rate of 10^{-3} s^{-1}. The gauge length of the tensile specimen was 10 mm, and the gauge width and gauge thickness were 3 and 0.9 mm, respectively, after final polishing. Microstructural analysis before and after the tensile test was performed with the aid of X-ray diffraction (XRD), optical microscopy (OM), scanning electron microscopy (SEM) equipped with energy dispersive X-ray spectroscopy (EDS) and electron backscatter diffraction (EBSD), and electron channeling contrast imaging (ECCI) techniques. Furthermore, the solidification path and solidification segregation of the CrMnFeCoNi alloy were simulated by Scheil's model with the aid of Thermo-Calc software and TCHEA thermodynamic database for HEAs.

5.3 Results

5.3.1 Densification

The density of the LENS^{TM}-deposited CrMnFeCoNi alloy was measured to be 7.953 g/cm^3 by the Archimedes method, leading to a relative density of 99.67% (assuming the theoretical density of the CrMnFeCoNi alloy is 7.980 g/cm^3). Fig. 5.2 (a)-(d) give the X-ray CT 2D and 3D images of the LENS^{TM}-deposited CrMnFeCoNi alloy, also showing no obvious pores and thus very dense specimen. Based on the X-ray CT data, the porosity (i.e. defect volume ratio) was determined to be 0.25%, indicating a relative density of 99.75%. This value is slightly higher than the relative density value determined by the Archimedes method because some very small pores cannot be detected by X-ray CT due to its resolution restriction. Fig. 5.2 (e) shows the pore size distribution in the LENS^{TM}-deposited CrMnFeCoNi alloy. It can be seen that the pore size follows a normal distribution, and the average size of the pores is approximately 6 μm. Most importantly, no extremely large pores were detected, which are definitely detrimental to the ductility.

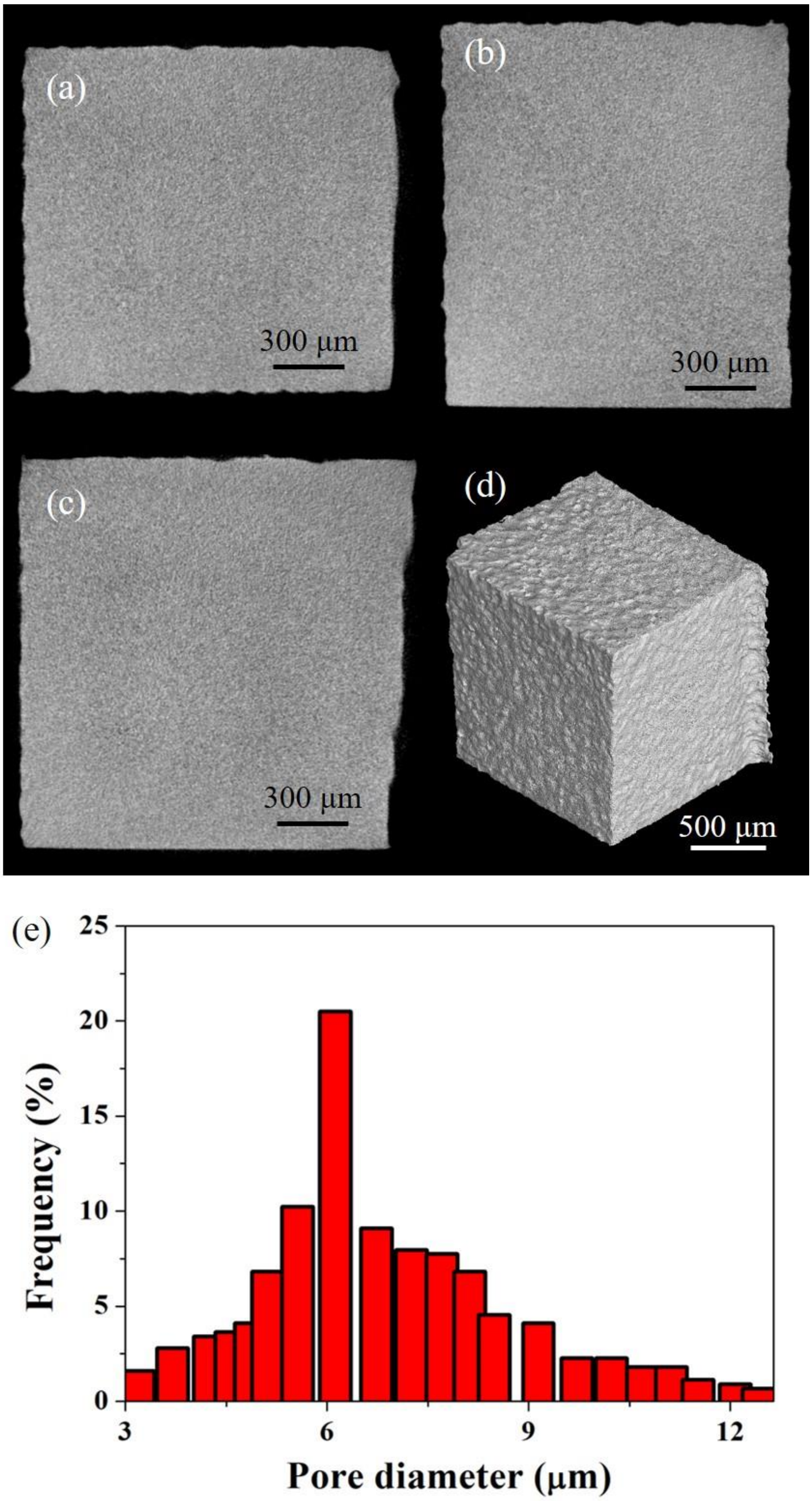

Fig. 5.2 X-ray CT characterization of internal pores in the LENS$^{\text{TM}}$-deposited CrMnFeCoNi alloy. (a) Top view; (b) Right view; (c) Front view; (d) 3D view; (e) Pore size distribution

5.3.2 Solidification conditions

Fig. 5.3 (a) gives a typical thermal map of the melt pool looking down from the top during the LENS^{TM} processing, with the laser scan direction indicated by the white arrow. The map was colorized to show the temperature (in Kelvin) down to the liquidus temperature, i.e. 1613 K, of the CrMnFeCoNi alloy [226]. Therefore, the whole melt pool, i.e. inside the purple outline, was visible. The temperature reached a peak value, approximately in the melt pool center, and decreased with the distance from the melt pool center. Temperature data were extracted and are plotted along the white dashed line, i.e. along the laser scan direction and through the hottest (peak temperature) point in the melt pool, as shown in Fig. 5.3 (b). The zero value on the X axis indicated the hottest point. The temperature curve was divided, using the hottest point, into two parts, with these two parts experiencing the heating and cooling processes, respectively. We paid more attention to the cooling part in this study. The liquidus temperature T_L of the equiatomic CrMnFeCoNi alloy was indicated by the horizontal dashed line in Fig. 5.3 (b), and the crossover point between the cooling part and the liquidus temperature was the boundary between the liquids and the mushy zone, i.e. the region where liquids and solids co-existed, and solidification was occurring. The solidification conditions in the vicinity of this crossover point are important for as-solidified microstructure formation and were investigated in this study.

From the cooling part of the temperature curve, the temperature gradient and cooling rate curves were calculated accordingly and are plotted in Fig. 5.3 (c) and (d), respectively. The temperature gradient curve was obtained by differentiating the temperature curve with distance, and the cooling rate curve was obtained by multiplying the temperature gradient by the laser scan speed, i.e. 5 mm/s. The temperature gradient and cooling rate curves exhibited the same trends, both of which decreased initially and then increased with the distance from the hottest point. The temperature gradient, G_{liquidus}, and cooling rate, CR_{liquidus}, values at the crossover point were calculated to be 347 K/mm and 1732 K/s, respectively.

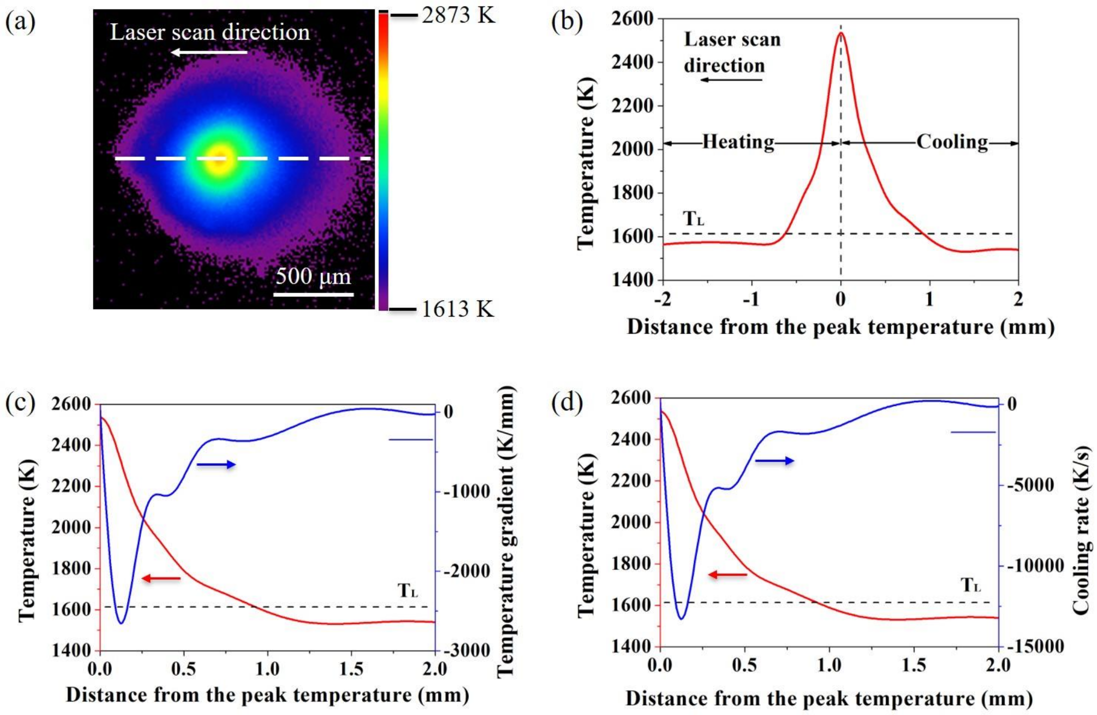

Fig. 5.3 (a) A typical colorized thermal map of the melt pool looking from the top; (b) Temperature curve which was along the laser scan direction and through the hottest point in the thermal map in (a); (c) Temperature (red line) and temperature gradient (blue line) curves; (d) Temperature (red line) and cooling rate (blue line) curves. The liquidus temperature T_L=1613 K is indicated by the black broken line in (b)-(d).

5.3.3 Phase formation

Fig. 5.4 (a) shows the XRD pattern of the LENS$^{\text{TM}}$-deposited CrMnFeCoNi specimen, with the XY-plane examined. Only a single disordered face centered cubic (FCC) structured phase was detected, which is in good agreement with its counterparts manufactured by conventional metallurgical routes [1, 11, 218] and alternative AM processes [116]. The single-phase characteristic was rationalized by the solidification path simulated by Scheil's model with the aid of the high entropy alloys database, as shown in Fig. 5.4 (b). According to the simulated solidification path, only a single FCC phase solidified from the liquid, i.e. L→L+FCC→FCC. It should be noted that, at lower temperatures, the single-phase structure has been proven to be thermodynamically unstable, and multiple precipitates may be formed in the matrix [68-70]. However, a very long annealing time was a prerequisite to establish the thermodynamic equilibria and lead to the precipitate formation, which could not be fulfilled in the present case. Therefore, the single-phase disordered solid solution structure in the just solidified state was retained down to room temperature. Furthermore, we observed that the predicted liquidus temperature (i.e. 1596 K) by Scheil's model was in good agreement with the measured value of 1613 K [226].

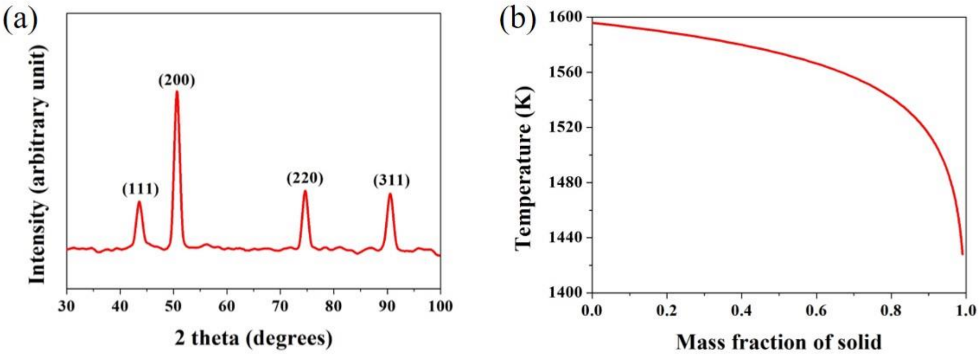

Fig. 5.4 (a) XRD pattern of the LENS^{TM}-deposited CrMnFeCoNi specimen, with the XY-plane examined; (b) Solidification path (L→L+FCC→FCC) of the CrMnFeCoNi alloy calculated by Scheil's model with the aid of the high entropy alloys database. Both results confirm the single-phase disordered FCC structure of the LENS^{TM}-deposited CrMnFeCoNi alloy.

5.3.4 As-deposited microstructures

Fig. 5.5 shows the longitudinal cross-sectional, i.e. the XZ plane, microstructures of the CrMnFeCoNi alloy in the as-deposited state. The layer-by-layer deposition patterns are visible, with the melt pool boundaries and layer boundaries indicated, as shown in Fig. 5.5 (a). The average layer thickness was determined to be 154 μm based on optical micrographs. The deposition patterns are closely related to the laser scan strategy [136, 227-229]. For the bidirectional and cross-hatched scan strategy used in the present study, the as-deposited specimen exhibits a periodic deposition pattern with a cycle of two layers, i.e. the layers 1, 3, and 5 correspond to the laser scan along the X direction, and the layers 2, 4 and 6 correspond to the laser scan along the Y direction. The distance between two adjacent melt pool bottoms corresponds to a hatch spacing of 460 μm. The enlarged optical micrograph shows that the melt pool solidification was dominated by columnar growth, approximately along the maximum heat flux direction that was perpendicular to the melt pool boundaries (Fig. 5.5 (b)). As the LENS^{TM}-deposited CrMnFeCoNi alloy exhibited a single-phase FCC solid solution structure (Fig. 5.4), each columnar grain could be seen as a tiny FCC-structured single crystal. Fig. 5.5 (c) and (d) give the inverse pole figure (IPF) and kernel average misorientation (KAM) maps of a same region of 900 μm by 900 μm, respectively. The grains in the IPF map were colorized based on their orientations with respect to the building direction (i.e. the Z axis). The high angle grain boundaries (HAGBs, misorientation > 15°) were highlighted in black in the IPF and KAM maps, and based on the HAGBs, the average grain size (i.e. the average width) of the columnar grains was estimated to be 13 μm. Furthermore, a large color variation was observed within the individual grains (Fig. 5.5 (c)), indicating the large local misorientation across the grains. This was further evidenced in the KAM map.

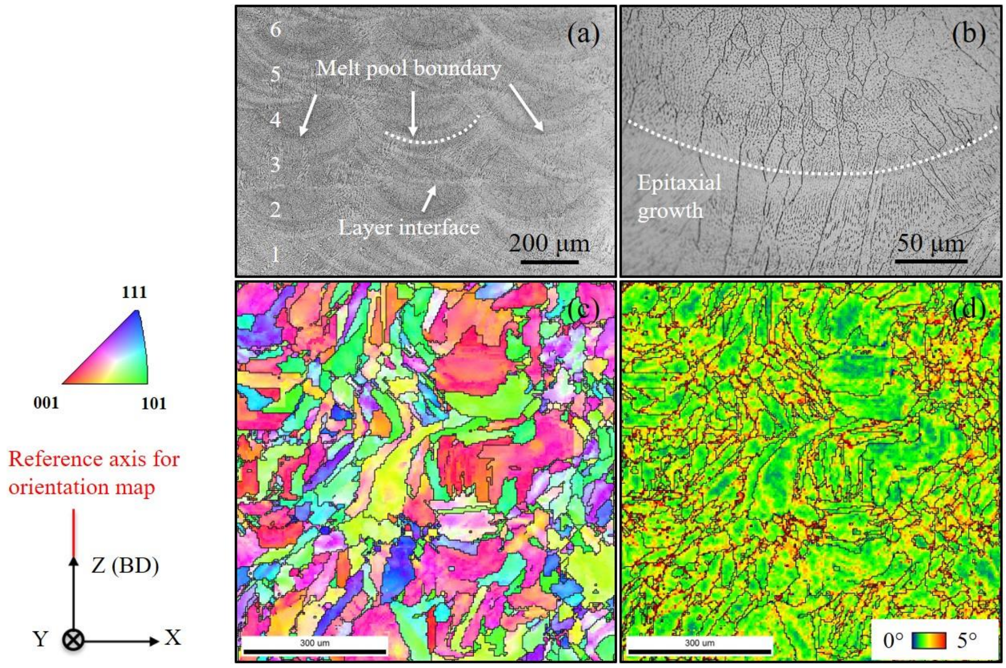

Fig. 5.5 The longitudinal cross-sectional (i.e. the XZ plane) microstructures of the CrMnFeCoNi alloy in the as-deposited state. (a) and (b) Optical micrographs showing the layer-by-layer deposition patterns and the epitaxial growth mode, respectively; (c) and (d) IPF and KAM maps of a region of 900 μm by 900 μm, respectively. The high angle grain boundaries (HAGBs, misorientation > 15°) were highlighted in black in (c) and (d). The reference axis for the IPF map is the building direction.

As for the large local misorientation within the grains, we attribute it to the solidification substructures and high dislocation densities in the as-deposited specimen, as revealed by the ECCI images in Fig. 5.6. It can be seen from Fig. 5.6 (a) that within columnar grains some micron sized (2 ~ 5 μm) solidification substructures were formed as indicated by the white arrows. These substructures were either cellular or pillar shaped, which were view-angle-dependent. High densities of dislocations (i.e. the white lines) were observed within these substructures, as shown in Fig. 5.6 (b) and (c). It should be mentioned that the residual stress in the LENS^{TM}-deposited CrMnFeCoNi alloy was measured to be approximately 182 MPa (the average value of residual stresses measured at three points). The existence of residual stress indicates the plastic deformation inside the specimen, which coincides with the observed high density of dislocations. These dense dislocations are deemed associated with the mechanical behavior in a specific way and are discussed later.

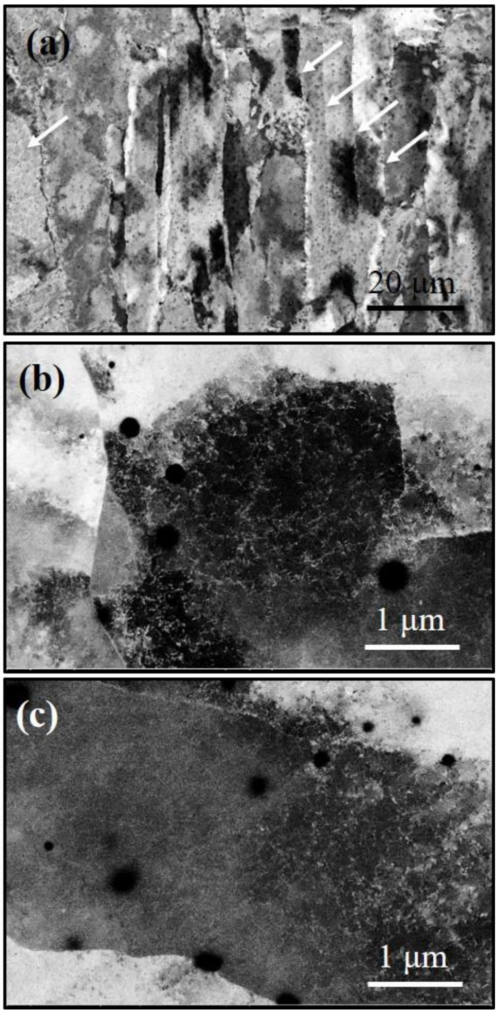

Fig. 5.6 ECCI images of the LENS^{TM}-deposited CrMnFeCoNi alloy showing (a) solidification substructures and (b-c) high dislocation densities. Some solidification substructure boundaries are indicated by the white arrows in (a). The dislocations in (b) and (c) appear bright as compared with the matrix under the current diffraction conditions.

Fig. 5.7 (a) gives the elemental distribution in a region containing several solidification substructures. It can be seen that Mn and Ni segregated at the substructure walls, and Co, Cr, and Fe segregated in the substructure interiors. The elemental concentration in the remaining liquid as a function of the temperature was simulated by Scheil's model with the aid of the high entropy alloys database, and is shown in Fig. 5.7 (b). It can be seen that with the decrease of the temperature, the concentrations of Mn and Ni in the remaining liquid increased, and the concentrations of Fe, Cr, and Co showed the opposite trend. Based on the simulated results, the solidification process of the CrMnFeCoNi alloy can be regarded as a process of rejecting Mn and Ni atoms into the remaining liquid, leading to the enrichment of Fe, Cr, and Co atoms in the first solidified regions, i.e. substructure interiors, and the enrichment of Mn and Ni atoms in the later solidified regions, i.e. substructure walls. Clearly, the simulated and experimental results agree well with each other.

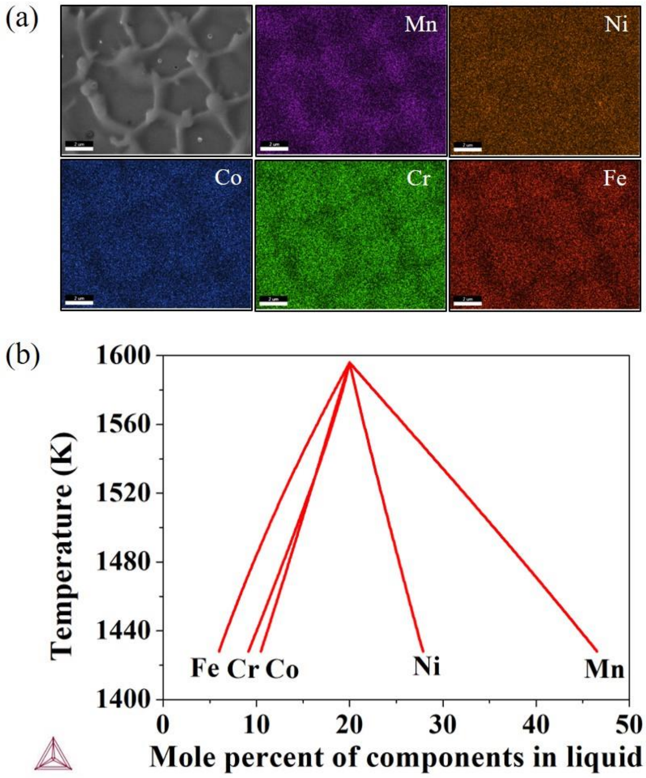

Fig. 5.7 Elemental micro-segregation of the CrMnFeCoNi alloy during solidification. (a) EDS elemental mapping of a region of several solidification substructures; (b) Compositional evolution of the remaining liquid simulated by Scheil's model with the aid of the high entropy alloys database. All scale bars in (a) are 2 μm. Both elemental mapping and simulated compositional evolution show the segregation of Co, Cr and Fe at first solidified regions (i.e. solidification substructure interiors), and the segregation of Mn and Ni at later solidified regions (i.e. solidification substructure walls) during solidification.

5.3.5 Tensile behavior

The typical engineering tensile stress-strain curve at ambient temperature of the LENS^{TM}-deposited CrMnFeCoNi alloy is shown in Fig. 5.8 (a). The engineering yield strength, i.e. the stress at which 0.2% plastic deformation occurs, σ_y, and the strain to failure, ε_f, were measured to be 517 MPa and 26%, respectively. Furthermore, uniform tensile elongation was measured to be 17% which is the engineering strain value corresponding to the maximum point, i.e. the ultimate tensile stress, on the engineering stress-strain curve. When the maximum point was reached, nonuniform plastic deformation begins, and geometric instability, i.e. necking phenomenon, occurs. Clearly, the uniform tensile elongation is an important measure of the ductility of an alloy. Fig. 5.8 (b) gives the typical SEM secondary electron image of the tensile fracture surface. The ductile fracture characteristic can be confirmed from a vast number of fine dimples on the fracture surface.

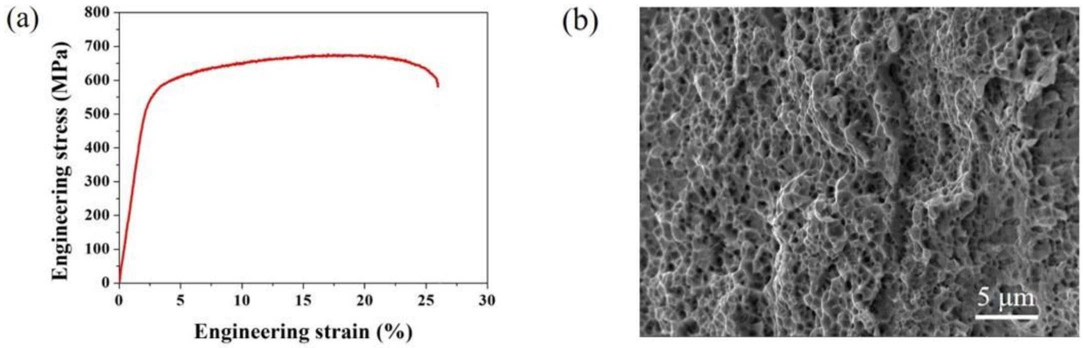

Fig. 5.8 Tensile behavior of the LENS^{TM}-deposited CrMnFeCoNi specimen at room temperature. (a) Engineering stress-strain curve; (b) Fracture surface.

Fig. 5.9 shows the microstructure of the LENS^{TM}-deposited CrMnFeCoNi alloy that was tensile tested to fracture. The deformed microstructures investigated both by EBSD and by ECCI were approximately 3 mm far from the fracture surface to avoid the necking region, and therefore the investigated regions experienced uniform plastic deformation during the tensile test. Twins were occasionally observed in the IPF map and further confirmed by the misorientation profile, as shown in Fig. 5.9 (a) and (b). Due to the absence of twins of any types, i.e. growth, annealing, or deformation/mechanical, prior to straining, these twins are formed during the tensile process and are classified as deformation twins. Fig. 5.9 (c) and (d) give the ECCI images of these deformation twins at different magnifications. It can be seen that the thickness of these deformation twins was about 50 nm. It is also noted that the step size 1 μm for EBSD characterization is larger than the nanotwin thickness, and therefore the nanotwins seem not continuous and intact in the IPF map (Fig. 5.9 (a)). However, since the electron beam size is far below 50 nm, the crystallographic information could still be obtained when the beam hits the twin region, and thus the combination of the misorientation profile in Fig. 5.9 (b) and the ECCI investigations in Fig. 5.9 (c) and (d) can confirm the twin relationship. In view of the slight degree of the twinning, the deformation process is reckoned to be dominated by dislocation activities which are shown in Fig. 5.9 (e). The deformation mechanisms and their contributions to the uniform tensile ductility are discussed in detail later.

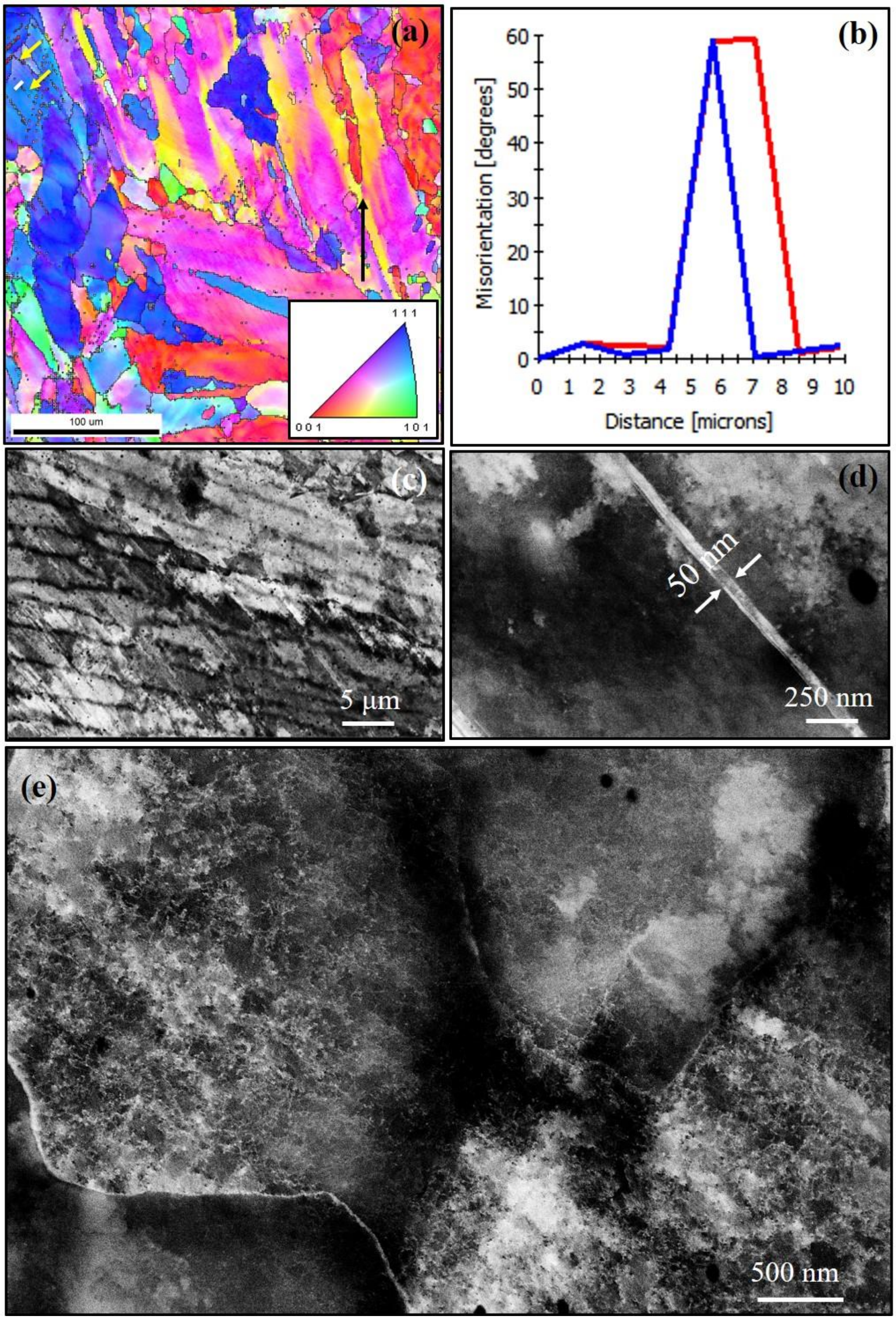

Fig. 5.9 Microstructures of the LENS^{TM}-processed CrMnFeCoNi alloy tensile tested to fracture. (a) EBSD IPF map with the reference axis (black arrow) aligned vertically upwards. Deformation twins are indicated by the yellow arrows; (b) Misorientation profile plotted over the white solid line in the IPF map (red line: point-to-point; blue line: point-to-origin); (c) and (d) ECCI images at different magnifications showing nanoscale deformation twins; (e) ECCI image showing the dislocation substructures in the deformed microstructure.

5.4 Discussion

5.4.1 Formation of the as-deposited microstructures

The as-deposited microstructures at multiple length scales, i.e. columnar grains, solidification substructures, and dislocation substructures, are formed. Clearly, the columnar growth, rather than the equiaxed growth, dominates the melt pool solidification of the CrMnFeCoNi alloy. This is consistent with the AM-processed conventional alloys, such as Ni-based superalloys [228] and titanium alloys [230], and is mainly attributed to the intrinsically high thermal gradient, i.e. 347 K/mm in the present study. Furthermore, the average grain size (13 μm) in the LENS^{TM}-deposited CrMnFeCoNi alloy is much finer than that reported for CrMnFeCoNi alloys (100 ~ 300 μm grain size [115, 116]) processed by other powder-blown AM processes. This is largely due to two reasons. First, the linear heat input used in the present study is much lower than that reported in the literature (80 J/mm in this work vs 120 ~ 850 J/mm in Refs. [115, 116]). The lower linear heat input normally results in a higher cooling rate, which facilitates the formation of finer microstructures. Furthermore, the grain size and the crystallographic orientation of the substrate are also believed to play an important role in grain growth and selection during solidification, and hence the final grain size [143]. However, this is not discussed in the present thesis due to insufficient microstructural details of the substrate. In addition, a very high density of dislocations is formed in the LENS^{TM}-deposited CrMnFeCoNi alloy, which is also reported for the AM-processed 316L stainless steel [231-233], and Inconel 718 superalloy [234]. The formation of such dense dislocations is possibly due to the development of the internal stress, and hence the internal strain, as the parts rapidly cool down to the ambient temperature after solidification. The gradually accumulated thermal strain in the AM-processed parts has to be accommodated, at least partially, by the dislocations. The effect of the accumulated dislocations on the yield strength is discussed later. Finally, elemental segregation at the micrometer scale is observed, with the cellular interior enriched in Co, Cr and Fe, and the cellular wall enriched in Mn and Ni. This is consistent with the observed dendritic segregation in the as-cast counterparts despite different solidification substructures, i.e. celluar for LENS^{TM}, and dendritic for casting [226, 235, 236].

5.4.2 Strengthening mechanisms

5.4.2.1 The yield strength of the LENS^{TM}-deposited CrMnFeCoNi alloy

The yield strength of a polycrystalline alloy is known to be the critical applied stress which can activate the dislocation motion in the vast majority of the grains and thus lead to the onset of the macro plastic deformation. This critical applied stress value (i.e. the yield strength) is determined by the microstructural features, i.e. base-metal lattice, interstitial or substitutional solute atoms, nanotwins, precipitates, grain boundaries, and initial dislocations. As the LENS^{TM}-deposited CrMnFeCoNi alloy is nanotwin-free, the contribution from the nanotwins can be disregarded. It should be noted, however, that the nano-twinning behavior after yielding point was observed in this study (Fig. 5.9), but it does not contribute to the yield strength but to the work hardening, and is discussed later. Furthermore, the precipitation phases have been found in many alloys, such as Ni-based alloys and steels, and several models (e.g. Friedel's shear cutting model [237], and Mohles' dislocation dynamics model [238]) have been proposed to evaluate its contribution to the overall yield strength. However, as indicated by the XRD pattern and calculated solidification path (Fig. 5.4), the LENS^{TM}-deposited CrMnFeCoNi alloy exhibits a single-phase FCC structure, and therefore the precipitation hardening mechanism doesn't operate in this alloy, and its corresponding contribution can be also disregarded.

As for the solute atoms, they are normally discussed in dilute solid solution alloys with a single base metal, i.e. the solvent lattice, plus a certain amount of interstitial and substitutional solute atoms. These interstitial or substitutional solute atoms generate a local stress field which hinders the dislocation motion and therefore strengthen the alloy. However, in the present case, the CrMnFeCoNi alloy is a concentrated solid solution system with five elements in equiatomic ratios. All these five elements occupy the FCC lattice randomly, and no distinct solvent lattice and solute atoms exist. Therefore, for the CrMnFeCoNi alloy, the resistance from the solute atoms which is normally discussed in conventional alloys has to be converted to the lattice friction stress. Based on the above analysis, the yield strength of the LENS^{TM}-deposited CrMnFeCoNi alloy can be predicted by adding the contributions from the base-metal lattice friction, grain boundaries, and initial dislocations:

$$\sigma_{\mathrm{y}} = \sigma_{\mathrm{o}} + \Delta\sigma_{\mathrm{GBS}} + \Delta\sigma_{\mathrm{DS}} \tag{5.1}$$

where σ_{o}, $\Delta\sigma_{\mathrm{GBS}}$, and $\Delta\sigma_{\mathrm{DS}}$ represents yield stresses resulting from the lattice friction, grain boundary strengthening, and dislocation strengthening, respectively. But as discussed earlier, the σ_{o} value here is the resistance from a complex lattice of all these five constituent atoms rather than from the base metal. The σ_{o} value of the CrMnFeCoNi alloy at 293 K has been experimentally determined to be 125 MPa, in Ref. [218] and 194 MPa, in Ref. [239], respectively. In this study, their average value of 160 MPa is adopted. In the following, the contributions from grain boundary strengthening and dislocation strengthening are assessed based on classical equations and microstructural details achieved experimentally in Section 5.3.

Grain boundary strengthening mechanism operates in all polycrystalline alloys, and the grain refinement introduces higher concentrations of incoherent grain boundaries which more strongly block the dislocation motion and therefore strengthen the alloy. For microcrystalline alloys, the yield stress resulting from the grain boundary strengthening effect, $\Delta\sigma_{\mathrm{GBS}}$, can be estimated by [218]:

$$\Delta\sigma_{\mathrm{GBS}} = k \cdot d^{-0.5} \tag{5.2}$$

where k=494 MPa·μm$^{0.5}$ is the Hall-Petch coefficient for slipping at 293 K [218], and d is the average grain size. The $\Delta\sigma_{\mathrm{GBS}}$ value is calculated to be 137 MPa for the grain size of 13 μm in this study. In addition to the grain boundary strengthening effect, the high density of initial dislocations in the AM-ed alloys is also frequently regarded as an effective strengthening mechanism [93, 112]. The yield stress resulting from the dislocation strengthening effect, $\Delta\sigma_{\mathrm{DS}}$, can be estimated according to the Taylor hardening law [240]:

$$\Delta\sigma_{\text{DS}} = M\alpha Gb\sqrt{\rho} \tag{5.3}$$

where the Taylor factor M was estimated to be 3.06 [241], α=0.2 is a constant for FCC structured alloys, the shear modulus G was measured to be 80 GPa at 293 K [7, 242], b is the magnitude of the Burgers vector (<110>/2) of the full dislocation and was determined to be 0.2539 nm [243], and ρ is the initial dislocation density, i.e. the total length of dislocations per unit volume of the material. As indicated by Eq. (5.3), increasing the dislocation density, ρ, increases the $\Delta\sigma_{\text{DS}}$ value, due to the stronger interactions between the stress fields of dislocations. As shown in Fig. 5.6, the CrMnFeCoNi alloy in the as-deposited state exhibits a high density of dislocations, and the dislocation density, ρ, can be roughly estimated by following equations [244, 245]:

$$\rho = 2\sqrt{3}\varepsilon/(Db) \tag{5.4}$$

$$\beta cos\theta = K\lambda/D + 4\varepsilon sin\theta \tag{5.5}$$

where ε is the micro-strain, D is the crystallite size, b is again the magnitude of the Burgers vector (<110>/2) of the full dislocation, β is the full width at half maximum (FWHM) of the analyzed peaks from the XRD profile after subtracting the instrumental line broadening, θ is the Bragg angle of the analyzed peaks, K is a dimensionless shape factor with a value of 0.89, and λ is the X-ray wavelength that equals to 0.154056 nm for Cu-K_α radiation.

Based on Eqs. (5.4) and (5.5), the dislocation density ρ in the LENS$^{\text{TM}}$-deposited

CrMnFeCoNi alloy is estimated to be 3×10^{14} m^{-2}. Putting the estimated ρ value into Eq. (5.3), the yield stress resulting from the initial dislocations is estimated to be 215 MPa. The calculated yield strength (i.e. $\sigma_O+\Delta\sigma_{GBS}+\Delta\sigma_{DS}$=512 MPa) resulting from the lattice friction resistance, fine-grain strengthening effect, and dislocation strengthening effect agrees well with the measured value of 517 MPa. It also indicates that the yield strength of the LENS^{TM}-deposited CrMnFeCoNi alloy originates from multiple strengthening mechanisms, especially the dislocation strengthening mechanism whose contribution accounts for ~ 42% of the total yield strength. In other words, the highly dense dislocations of the LENS^{TM}-deposited CrMnFeCoNi alloy contribute to its yield strength significantly.

5.4.2.2 Compared with conventionally manufactured CrMnFeCoNi alloys

Section 5.4.2.1 discusses the yield strength of the LENS^{TM}-deposited CrMnFeCoNi alloy based on classical equations (i.e. Hall-Petch relationship, and Taylor hardening law) and experimentally achieved microstructural details (i.e. grain size and dislocation density). The variation of microstructural details, which can be achieved by changing the processing route, affects a lot the yield strength of an alloy. Fig. 5.10 shows a summary of the tensile yield strength versus uniform tensile elongation of the CrMnFeCoNi alloy manufactured by various routes. These include casting [116, 235], cold deformation, i.e. cold forging and rolling, followed by annealing [1, 218, 239], high pressure torsion followed by post-deformation annealing (HPT+PDA) [220], mechanical alloying followed by spark plasma sintering (MA+SPS) [219], selective laser melting (SLM) [112, 113, 179], and various laser powder-blown AM processes (i.e. laser metal deposition (LMD) [116], laser additive manufacturing (LAM) [115, 118], laser aided additive manufacturing (LAAM) [120], laser 3D printing [117], and

LENS™, i.e. the present work). It should be noted that different universities, labs or companies may use different terminologies to denominate the laser powder-blown AM process, however, they all build a part by remelting the surface of previous layers and simultaneously feeding metal powders into the remelted region, i.e. melt pool. Therefore, these processes can be classified into the same type in essence (i.e. using the laser as the heat source, and feeding powders by nozzles), and therefore in Fig. 5.10 we unify them as laser powder-blown AM process. These CrMnFeCoNi alloys are grouped into three categories, i.e. coarse-grained (CG, up to hundreds of micrometers), fine-grained (FG, 500 nm to a dozen or so micrometers), and ultrafine-grained or even nanocrystalline (UFG, < 500 nm; NC, < 100 nm), depending upon their grain sizes. It can be seen from Fig. 10 that the yield strength of the CrMnFeCoNi alloy approximately ranges from 170 to 1600 MPa, depending on the processing route and the resultant microstructure.

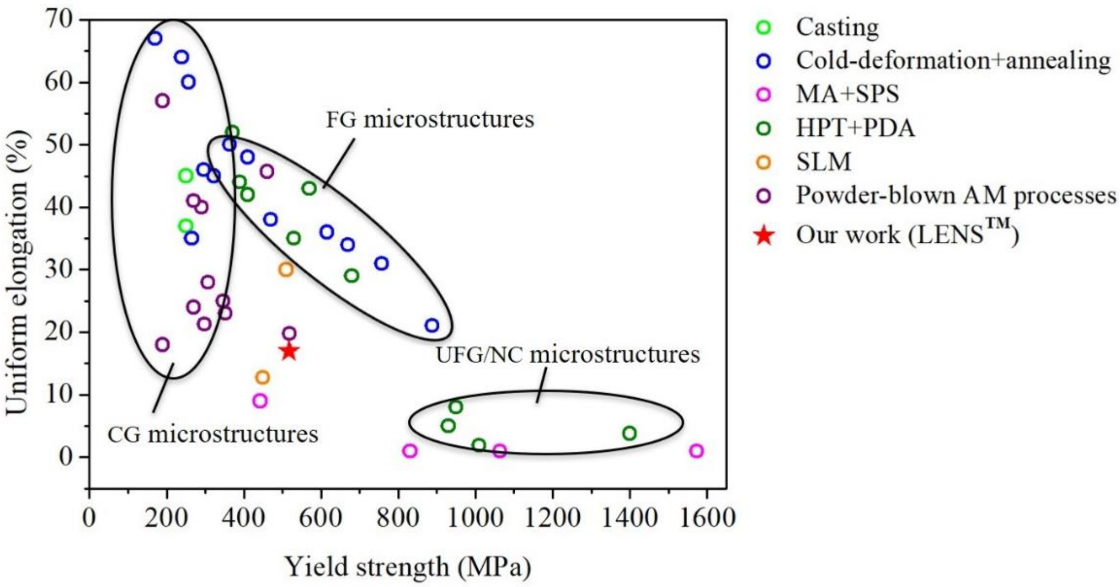

Fig. 5.10 A summary of tensile yield strength versus uniform tensile elongation for CrMnFeCoNi alloys manufactured via various routes, including casting [116, 235],

cold deformation, i.e. cold forging and rolling, followed by annealing [1, 218, 239], high pressure torsion followed by post-deformation annealing (HPT+PDA) [220], mechanical alloying followed by spark plasma sintering (MA+SPS) [219], selective laser melting (SLM) [112, 113, 179], and various laser powder-blown AM processes [115-118, 120], and LENS^{TM}, i.e. the present work). From a microstructural perspective, these alloys are classified into CG, FG, UFG/NC CrMnFeCoNi alloys.

For the as-casted CrMnFeCoNi alloy, besides the lattice friction stress, only the grain boundary strengthening mechanism contributes to its yield strength. And considering its coarse grains, the yield strength of the as-casted CrMnFeCoNi alloy is extremely low based on Eq. (5.2). Until now, most of the CrMnFeCoNi alloys are fabricated by cold deformation followed by annealing, and this specific kind of the CrMnFeCoNi alloy is referred to as wrought-annealed CrMnFeCoNi alloy in this study. For the wrought-annealed CrMnFeCoNi alloy, the grain boundary strengthening mechanism also operates, and its contribution to the yield strength is determined by the grain size. As reported in published works [1, 218, 239], the grain size of the wrought-annealed CrMnFeCoNi alloy may range from 155 to 0.5 μm, and the yield stress resulting from the grain boundary strengthening mechanism is therefore calculated to be from 40 to 865 MPa based on Eq. (2), i.e. $\Delta\sigma_{GBS}$=40 ~ 865 MPa. Furthermore, as the high dislocation density introduced during cold deformation is dramatically decreased during the recrystallization annealing treatment, the dislocation density is extremely low in the as-annealed state [84, 218]. The dislocation density in the as-annealed alloy is normally of the order of 10^{11} ~ 10^{12} m^{-2} [246]. Even when adopting the upper limit of 10^{12} m^{-2}, the calculated $\Delta\sigma_{DS}$ is only 12 MPa, which is much lower than that of the LENS^{TM}-deposited CrMnFeCoNi alloy. The total yield stress of the wrought-annealed

CrMnFeCoNi alloy resulting from all possible strengthening mechanisms is therefore calculated to be 212 to 1037 MPa, i.e. $\sigma_0+\Delta\sigma_{GBS}+\Delta\sigma_{DS}=212 \sim 1037$ MPa, which well agrees with the experimental values (Fig. 5.10). For the CrMnFeCoNi alloys fabricated by HPT+PDA or MA+SPS processes [219, 220], the grain size can be further reduced and even fallen into UFG and NC regimes. For this case, the dependence of the yield stress resulting from the grain boundary strengthening mechanism on the grain size cannot be precisely predicted by Eq. (5.2) that well applies to the microcrystalline alloys. But the strengthening effect is almost continuously observed when reducing grain sizes down to ~ 10 nm, and the yield strength of such UFG/NC CrMnFeCoNi alloys reaches above ~ 1000 MPa. Despite of the excellent yield strength, their uniform tensile elongation is very low. Overall speaking, a relatively good combination of the tensile yield strength and uniform tensile elongation is achieved in the FG regime. Fortunately, the LENS^{TM}-deposited CrMnFeCoNi alloy in this work also exhibits a FG microstructure, i.e. 13 μm grain size, and this is largely attributed to the rapid cooling rate, i.e. 1732 K/s, during melt pool solidification. Furthermore, it can be clearly seen that the high initial dislocation density activates an additional strengthening mechanism, i.e. dislocation strengthening, and therefore endows the LENS^{TM}-deposited CrMnFeCoNi alloy with a higher tensile yield strength than the wrought-annealed FG counterparts with similar grain sizes. By contrast, however, the uniform tensile elongation is lowered, which is discussed in section 5.4.3.

5.4.3 Origin of reduced ductility

5.4.3.1 Evaluation of work hardening capability

As analyzed in section 5.4.2, the yield strength of the LENS^{TM}-deposited CrMnFeCoNi alloy compares favorably with its wrought-annealed counterparts with similar grain sizes. However, its uniform tensile elongation is lowered, as can be seen from Fig. 5.10. Actually, reduced ductility is also commonly reported for the laser-based additively manufactured conventional alloys, e.g. 316L stainless steel [247], and titanium alloys [248, 249]. However, this phenomenon is not well understood to date. In this study, we compare the work hardening capabilities of the LENS^{TM}-deposited and wrought-annealed CrMnFeCoNi alloys. Fig. 5.11 shows the true stress versus logarithmic strain curves that are calculated from the engineering ones, and the plots of the true work hardening rate (WHR, h), i.e. the derivative of the true stress with respect to the logarithmic strain, as a function of the logarithmic strain. The data for the wrought-annealed CrMnFeCoNi alloy (17 μm grain size) is extracted from Ref. [84]. It can be seen from Fig. 5.11 that the WHR values are initially high but decrease with the logarithmic strain for both alloys. However, the WHR value of the LENS^{TM}-deposited CrMnFeCoNi alloy, by contrast, drops more rapidly during straining. This leads to the earlier intersection of the WHR- and true stress-logarithmic strain curves at a lower strain level. The crossover point indicates that the WHR value equals to the true stress, and at this critical point, the strain localization, i.e. the necking phenomenon, occurs according to the Considère’s criterion [250]. In other words, the relatively inadequate work hardening capability of the LENS^{TM}-deposited CrMnFeCoNi alloy leads to its earlier necking and hence reduced uniform tensile elongation, i.e. 17% of the LENS^{TM}-deposited CrMnFeCoNi alloy vs ~ 35% of the wrought-annealed counterpart.

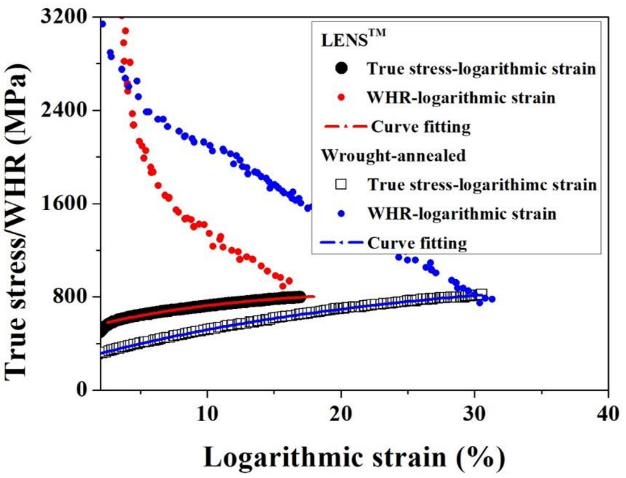

Fig. 5.11 Measured true stress-logarithmic strain curves, work hardening rate (WHR) curves, and curve fitting results for the LENS^{TM}-deposited and wrought-annealed CrMnFeCoNi alloys. The measured true stress-logarithmic strain curve and the WHR curve for the wrought-annealed CrMnFeCoNi alloy is abstracted from Ref. [84]. The true stress-logarithmic strain data for both alloys are fitted by Eq. (5.12).

5.4.3.2 Origin of work hardening

The mechanisms underlying the relatively inadequate work hardening capability needs to be clarified in terms of the evolution of the deformation substructures, i.e. the dislocation and nanotwin substructures, during straining. These deformation substructures can act as efficient barriers to hinder the gliding dislocations and therefore harden the alloys. In other words, the evolution of these deformation substructures governs the work hardening capability. As reported by Laplanche et al. [84], the dislocation density of the wrought-annealed CrMnFeCoNi alloy increases dramatically during straining, and these dislocations tend to tangle or even form dislocation cells (DCs) to minimize the elastic energy per unit length of the dislocation line. Such highly dense dislocation substructures effectively block the dislocation motion and therefore contribute to the work hardening capability. In addition to the dislocation multiplication, nanoscale deformation twins are reported to form after ~20% logarithmic strain, corresponding to ~720 MPa true stress [84]. As deformation progresses further, the volume of the deformation twins increases and the twin spacing decreases. As is well known, the arrangements of atoms on both sides of the twin boundaries are mirror reflections, and the formation of the twin boundaries leads to a continuous grain refinement process and thus a reduction in the mean free path of the dislocations, i.e. the dynamic Hall-Petch effect [251]. The combined effects of the dislocation multiplication and nanoscale deformation twinning lead to the substantial work hardening capability and thus the significant uniform tensile ductility of the wrought-annealed CrMnFeCoNi alloy.

5.4.3.3 The onset of twinning

As for the twining behavior, it is not always observed during the tensile test of the wrought-annealed CrMnFeCoNi alloy. For instance, deformation twins are not observed in the FG (503 nm grain size, which nearly falls into the UFG regime) wrought-annealed CrMnFeCoNi alloy which has been strained to failure at a logarithmic strain of nearly 30% [239]. Fortunately, the desirable twinning behavior is observed during the straining process of our LENS^{TM}-deposited CrMnFeCoNi alloy. To determine the onset of the deformation twins, the twinning stress, i.e. the critical true stress beyond which the twinning behavior is activated, is estimated in this study. The twinning stress has been found to be grain size dependent in conventional alloys [252-255], and a Hall-Petch type relationship is normally followed [252]:

$$\sigma_{\mathrm{tw}} = \sigma_{\mathrm{tw,o}} + k_{\mathrm{tw}} \cdot d^{-0.5} \tag{5.6}$$

where σ_{tw} is the twinning stress, $\sigma_{\mathrm{tw,o}}$ is the twinning stress for a single crystal, k_{tw} is the Hall-Petch coefficient for twinning, and d is again the average grain size. The $\sigma_{\mathrm{tw,o}}$ value can be estimated by [255]:

$$\sigma_{\mathrm{tw,o}} = M\gamma_{\mathrm{SF}}/b_{\mathrm{s}} \tag{5.7}$$

where M is again the Taylor factor, γ_{SF} is the stacking fault energy (SFE) that was determined to be 18 ~ 27 mJ/m^2 for the CrMnFeCoNi alloy [256, 257], b_{s}=0.1466 nm [243] is the magnitude of the Burgers vector (<112>/6) of the Shockley partial dislocation. Combining Eqs. (5.6) and (5.7), we get:

$$\sigma_{\mathrm{tw}} = M\gamma_{\mathrm{SF}}/b_{\mathrm{s}} + k_{\mathrm{tw}} \cdot d^{-0.5} \tag{5.8}$$

Eq. (5.8) indicates that the twinning stress σ_{tw} increases with the decrease in the grain size d. Assuming the twinning stress σ_{tw}=720 MPa for a grain size d=17 μm [84], the Hall-Petch coefficient for twinning, k_{tw}, is determined to be 1164 MPa·μm$^{0.5}$ that is more than two times higher than the Hall-Petch coefficient for slipping, i.e. 494 MPa·μm$^{0.5}$. This trend is consistent with previous studies that report the ratio of the Hall-Petch coefficient for twinning to that for slipping ranges from 1 ~ 4 for FCC-structured alloys [252, 258]. The much larger Hall-Petch coefficient for twinning indicates that the twinning stress is more strongly grain size dependent as compared with the grain size dependency of the yield strength. The twinning stress for the CrMnFeCoNi alloy with grain sizes of 13 and 0.503 μm is calculated to be 761 and 2083 MPa, respectively, according to Eq. (5.8). For the aforementioned FG wrought-annealed CrMnFeCoNi alloy with grain size of 503 nm, the estimated twinning stress is surprisingly high and is not reached till fracture, and therefore the nanoscale deformation twins are not observed.

For our LENS^{TM}-deposited CrMnFeCoNi alloy, the estimated twinning stress of 761 MPa is reached at a lower logarithmic strain of ~ 13%. The earlier activation of the deformation twins in the LENS^{TM}-deposited CrMnFeCoNi alloy is believed to be a direct result of two opposite effects. The higher twinning stress and the lower work hardening rate of the LENS^{TM}-deposited CrMnFeCoNi alloy make it more difficult to generate twinning. However, this adverse effect is fully compensated by its higher yield strength (i.e. 517 MPa of the LENS^{TM}-deposited CrMnFeCoNi alloy vs 265 MPa of the wrought-annealed counterpart), which results in its earlier reaching of the twinning stress 761 MPa, at a lower logarithmic strain level. As discussed earlier, the formation of these nanoscale deformation twins introduces additional intragrain interfaces which act as “strong” obstacles for gliding dislocations, and the earlier activation of these deformation twins is undoubtedly desirable. We observe that, however, the onset of twinning in the LENS^{TM}-deposited CrMnFeCoNi alloy is already very close to its necking instability point, i.e. 15.7% logarithmic strain, which implies that its uniform plastic deformation capability has been almost exhausted before the onset of twinning. Therefore, the lowered uniform tensile elongation of our LENS^{TM}-deposited CrMnFeCoNi alloy is believed to result from the evolution of dislocations (i.e. another work hardening contributor) during the course of straining.

5.4.3.4 The role of dislocation evolution in uniform tensile ductility

As can be seen by comparing Figs. 5.6 and 5.9, the dislocations are only slightly denser in the as-deformed microstructure of the LENS^{TM}-deposited CrMnFeCoNi alloy, which differs with the dramatically increased dislocation density reported for the wrought-annealed counterpart [84]. In other words, the net increase in the dislocation density during the straining process is smaller for the LENS^{TM}-deposited CrMnFeCoNi alloy as compared with the wrought-annealed counterpart. The evolution of the dislocation density during the straining process is concurrently determined by the accumulation and annihilation of the dislocations. According to a time-proven approach proposed by Kocks and Mecking [259-261], the evolution of the dislocation density with the strain, $d\rho/d\varepsilon$, can be estimated by:

$$d\rho/d\varepsilon = M(k_1\sqrt{\rho} - k_2\rho) \tag{5.9}$$

where the dislocation storage rate coefficient, k_1, is associated with the dislocation accumulation due to the dislocation-dislocation interactions (e.g. the interactions between the gliding dislocations and forest ones), and the dynamic recovery coefficient, k_2, is associated with the dislocation annihilation by several possible mechanisms (e.g. the climb of edge dislocations, and the cross-slip of screw dislocations). These two parameters k_1 and k_2 are microstructural dependent constants. The increased dislocation density ρ would lead to an increased flow stress σ, as given by the Taylor equation (Eq. (5.3)), but the $\Delta\sigma_{DS}$ in Eq. (5.3) is substituted by the flow stress σ here [240]:

$$\sigma = M\alpha Gb\sqrt{\rho} \tag{5.10}$$

Combining Eqs. (5.9) and (5.10) provides the flow stress as a function of the strain in the plastic regime:

$$\sigma = (\alpha GbMk_1/k_2)\,[1 - exp(-k_2M\varepsilon/2)] \tag{5.11}$$

Eq. (5.11) satisfactorily describes a large amount of true stress-logarithmic strain experimental data in the plastic regime of conventional alloys with CG microstructures [262]. To extend Eq. (5.11) to FG or even UFG microstructures, the grain boundary strengthening needs to be considered, and therefore a grain size dependent constant σ_1 is suggested and introduced into Eq. (5.11) as follows [263]:

$$\sigma = \sigma_1 + (\alpha GbMk_1/k_2)\,[1 - exp(-\,k_2M\varepsilon/2)] \tag{5.12}$$

Eq. (5.12) can be used successfully to describe a variety of alloys over a wide range of grain sizes [264]. Going one step further, the plastic instability corresponding to the onset of the nonuniform plastic deformation is derived by linear stability analysis [262-264]:

$$(h/\sigma)\,(1 - 1/m) + [k_2M/(2m)]\,(1 - \sigma_1/\sigma) \leq 1 \tag{5.13}$$

where the parameter m is associated with but not exactly the strain rate sensitivity introduced by Hart [265]. The parameter h is the aforementioned work hardening rate and given by:

$$h = d\sigma/d\varepsilon = (\alpha GbM^2k_1/2)\,exp(-\,k_2M\varepsilon/2) \tag{5.14}$$

It can be seen from Eq. (5.14) that both the dislocation storage rate coefficient, k_1, and the dynamic recovery coefficient, k_2, affect the work hardening capability of an alloy. Nevertheless, we want to emphasize that the parameter k_2 exhibits a more pronounced effect because it resides in the exponential function. Replacing the flow stress, σ, and the strain hardening coefficient, h, in Ineq. (5.13) with the expressions in Eqs. (5.12) and (5.14), respectively, and substituting the equality sign for the inequality sign leads to the necking strain ε_N [262-264]:

$$\varepsilon_\mathrm{N} = [2/(k_2M)] \cdot \ln\{[1 + (k_2M/2)(1 - 2/m)]/[1 + \sigma_1k_2/(\alpha GbMk_1) - k_2M/(2m)\} \quad (5.15)$$

For a variety of alloys and testing conditions, $1/m$ <<1, and therefore Eq. (5.15) can be reduced to:

$$\varepsilon_\mathrm{N} = [2/(k_2M)] \cdot \ln\{[1 + (k_2M/2)]/[1 + \sigma_1k_2/(\alpha GbMk_1)]\} \quad (5.16)$$

Eq. (5.16) can be used to estimate the onset of necking during the course of the monotonic tension. It can be again seen from Eq. (5.16) that the dynamic recovery rate coefficient k_2 governs the necking phenomenon. By contrast, the other intrinsic model variables, i.e. k_1 and σ_1, are less significant as they affect the necking strain logarithmically. To further highlight the important role of the parameter k_2 in the necking strain ε_N, the lower and the upper bound estimates based on Eq. (5.16) are given by:

$$2/(k_2M) < \varepsilon_\mathrm{N} < 2\ln\,[1 + k_2M/2]/(k_2M) \quad (5.17)$$

This double inequation is valid for any reasonable combinations of the model variables, and it clearly shows that the estimated necking true strain ε_N is in a very narrow band, with the upper and lower bounds governed by the k_2 value alone. The non-linear Eq. (5.12) is fitted to the measured true stress-logarithmic strain curve in the plastic regime, and very good fitting is achieved by adjusting the fitting parameters, i.e. the intrinsic model variables, as shown in Fig. 5.11. The necking true strain, ε_N, is estimated accordingly, based on Eq. (5.16), to be 16.2% which agrees well with the measured value 15.7%. Good fitting is also achieved for the wrought-annealed CrMnFeCoNi alloy, and the k_2 values for the LENS^{TM}-deposited and wrought-annealed CrMnFeCoNi alloys are 5.4 and 2.67, respectively. The larger k_2 value of the LENS^{TM}-deposited CrMnFeCoNi alloy indicates a promoted dynamic dislocation recovery process, and hence a less significant net increase in the dislocation density during straining, which is consistent with what we observed experimentally. As a direct result, the work hardening capability is somewhat weakened, which is believed to be the main reason for the reduced uniform tensile elongation of the LENS^{TM}-deposited CrMnFeCoNi alloy.

5.5 Conclusions

The primary goal of this chapter is to investigate the potential of the LENS^{TM} process in the manufacture of the quinary equi-atomic HEA CrMnFeCoNi. To investigate the potential, the CrMnFeCoNi alloy was additively manufactured by the LENS^{TM} process, and the solidification conditions, phase formation, as-deposited microstructures, and tensile behavior are investigated. Furthermore, the tensile yield strength and uniform tensile elongation are modeled, and the underlying mechanisms for the improved yield strength and lowered ductility, as compared with the wrought-annealed counterparts with similar grain sizes, are discussed. The following conclusions could be drawn:

(1) The LENS^{TM}-deposited CrMnFeCoNi alloy exhibits a single-phase disordered face centered cubic structure, as evidenced by XRD, and rationalized by Scheil’s solidification simulation with the aid of the high entropy alloys database.

(2) Multi-scale as-deposited microstructures, i.e. columnar grains, solidification and dislocation substructures, are formed. Furthermore, elemental segregation is observed and rationalized by Scheil's simulation.

(3) The LENS^{TM}-deposited CrMnFeCoNi alloy exhibits a tensile yield strength that is comparable to that of finer-grained wrought-annealed counterparts. This is largely attributed to the high dislocation density, in the LENS^{TM}-deposited CrMnFeCoNi alloy, and hence the initial-dislocation strengthening, which are insignificant and can be disregarded in the wrought-annealed counterparts.

(4) The tensile deformation process is mainly accommodated by dislocation activities with the assistance of deformation twinning. The promoted dislocation recovery process during straining leads to a weakened work hardening capability, and hence a reduced uniform tensile elongation, as compared with the wrought-annealed counterparts. Overall, however, the capability of the LENS^{TM} process to manufacture the high-performance CrMnFeCoNi alloy for engineering applications is confirmed in this chapter.

Chapter 6 Additive manufacturing of senary non-equi-atomic alloy $AlCoCrFeNiTi_{0.5}$ by laser engineered net shaping

6.1 Introduction

To date, the predominantly studied additively manufactured (AM-ed) high entropy alloys (HEAs) are $Al_xCoCrFeNi$ [29, 52, 106-111] and CrMnFeCoNi [112-120] alloys. They were manufactured by various AM processes with different processing parameters. Other work includes AM of $Co_{1.5}CrFeNi_{1.5}Ti_{0.5}Mo_{0.1}$ [121], TiZrNbMoV [122], $Co_{0.5}CrCu_{0.5}FeNi_{1.5}AlTi_{0.4}$ [123] and compositionally graded HEAs, i.e. $AlCo_xCr_{1-x}FeNi$ ($0 \leq x \leq 1$) [124], $Al_xCrCuFeNi_2$ ($0 < x < 1.5$) [125] and $AlCrFeMoV_x$ ($0 < x < 1$) [126]. It is typically reported that these AM-ed HEAs are predominantly characterized by columnar and textured microstructures, see e.g. Refs. [106, 111, 112, 114], despite the fact that equiaxed grains are achievable at specific heights/compositions of the compositionally graded HEAs [124-126]. The predominantly columnar and textured microstructures are not surprising and are consistent with those of AM-ed conventional alloys [151, 153, 213, 228, 266-270]. It is widely acknowledged that, for a specific alloy, the temperature gradient G and solidification velocity V concurrently determine the volume fraction ϕ of the equiaxed crystals at solidification front, and hence concurrently control the solidification microstructure during the AM process (i.e. $\phi > 49\%$, fully equiaxed; $\phi < 0.66\%$, fully columnar; $0.66\% < \phi < 49\%$, mixed) [271]. Such effects can be quantitively described by Gäumann’s model [272], which takes into accounts high velocity effects and is hence applicable to rapid solidification, e.g. the AM process. In most cases, the G - V combinations (high G, low V) associated with the AM process lead to a ϕ value far below 49% and even below 0.66%, indicating that columnar grain microstructures, typically with crystallographic textures, are formed. Such morphological and crystallographic textures may result in mechanical anisotropy [266, 273], which reduces the freedom in component design.

In this chapter, the AM-ed $AlCoCrFeNiTi_{0.5}$ was given special focus, which is a prototype HEA with multi-phase microstructures (i.e. disordered A2-structured precipitates embedded in ordered B2-structured matrix) and excellent wear resistance [12, 59, 274]. We found that the fully equiaxed grain microstructure with random textures is formed in this AM-ed $AlCoCrFeNiTi_{0.5}$ HEA. A large density of nucleation sites is estimated from the final solidification microstructure, and microstructural features provide insights into the origin of these nucleation sites. Furthermore, the volume fraction ϕ values of equiaxed crystals at solidification front for various G - V combinations established in this chapter are evaluated, with the aid of Gäumann's model [272], to provide a theoretical basis for our experimental findings. This chapter provides guidelines to produce fully equiaxed and randomly textured alloys by the AM process.

6.2 Experimental

A series of $AlCoCrFeNiTi_{0.5}$ cuboid specimens (8 mm by 8 mm by 6 mm) were manufactured from the prealloyed powders using different laser powers and laser scan speeds (300 ~ 600 W and 5 ~ 20 mm/s, respectively). A bidirectional scan path with a hatch spacing of 460 μm and a cross-hatched scan were adopted during the manufacturing process. The thermal history of the melt pool was recorded by a two-wavelength imaging pyrometer. The phase identification was performed with the aid of X-ray diffraction (XRD). The microstructural analysis was performed with the aid of scanning electron microscopy (SEM), electron backscatter diffraction (EBSD), and energy dispersive X-ray (EDS) techniques. For SEM, both backscattered electron (BSE) imaging and secondary electron (SE) imaging were used. The thermodynamic calculations were conducted by the CALPHAD (CALculation of PHAse Diagram) method, on the platform of the Thermo-Calc software 2019a equipped with a HEA database. The compression tests were performed on the cylindrical samples, with the dimensions of $\phi 2 \times 4$ mm. More details regarding the materials preparation and characterization have been given in chapter 2.

6.3 Results

6.3.1 Evaluation of *G* and *V* values

Fig. 6.1 (a) shows a representative color-coded temperature image of the melt pool surface for the AlCoCrFeNi$Ti_{0.5}$ alloy deposited at a laser power of 400 W and a scan speed of 5 mm/s. The white arrow represents the laser scan direction. It can be observed from the thermal image that the peak temperature region is approximately located in the melt pool center. The temperature profile was evaluated along the white dashed line in Fig. 6.1 (a), which passes the peak temperature in the melt pool and is in the laser scan direction, and is shown in Fig. 6.1 (b). The broken black line indicates the liquidus temperature T_L = 1620 K (calculated by Thermo-Calc software) of the AlCoCrFeNi$Ti_{0.5}$ alloy. The zero value on the X axis indicates the peak temperature point, which divides the melt pool into heating and cooling regions. Obviously, the latter region needs to be paid more attention. The G value in the cooling region was calculated accordingly, and its profile is shown in Fig. 6.1 (c). It can be seen that the G value is not a constant in the melt pool, and in this paper we adopt the G value at the melt pool boundary, at which solidification occurs. The melt pool boundary is represented by the crossover point between the temperature curve and the horizontal liquidus temperature line. As shown in Fig. 6.1 (c), the G value was estimated to be approximately 150 K/mm.

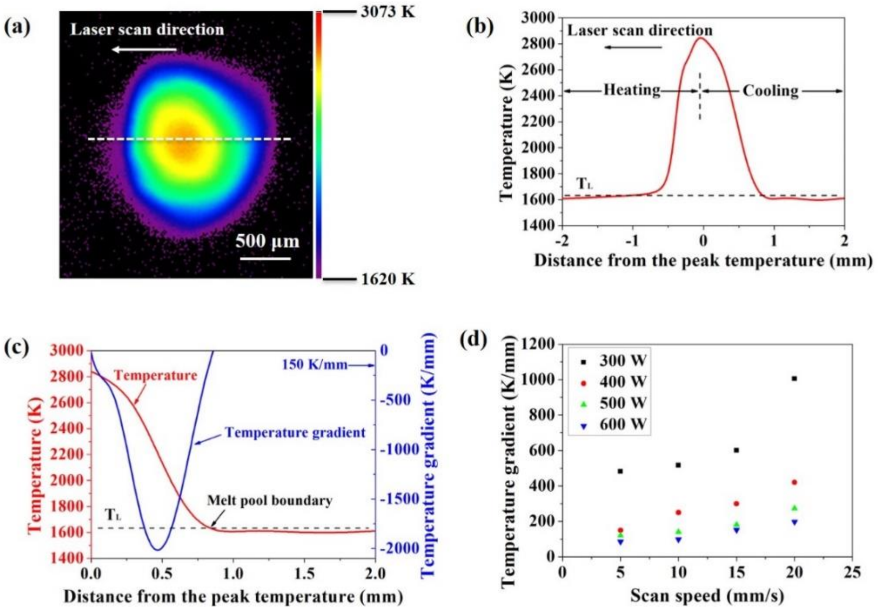

Fig. 6.1 (a) A representative color-coded temperature image of the melt pool surface for the AlCoCrFeNiTi$_{0.5}$ alloy deposited at a laser power of 400 W and a scan speed of 5 mm/s. The laser scan direction is indicated by a white arrow. (b) Temperature profile along the white dashed line shown in (a), which passes the peak temperature in the melt pool and is in the laser scan direction. The hottest point divides the temperature profile into heating and cooling regions. (c) Temperature profile and corresponding temperature gradient profile in the cooling region. The broken black lines in (b) and (c) indicate the liquidus temperature $T_{\mathrm{L}} = 1620$ K. (d) A summary of temperature gradients corresponding to various laser scan speeds and laser powers.

The same method was also used to evaluate the *G* values corresponding to various laser scan speeds and laser powers used in this study, and the results are summarized in Fig. 6.1 (d). It can be clearly seen that increase in laser scan speed or decrease in laser power contributes to a larger *G* value, i.e. a stronger temperature gradient. In summary, the manipulation of the laser scan speeds and laser powers creates a wide range of *G* values (i.e. 85 to 1005 K/mm). As for the *V* value at the trailing edge of the melt pool, it is approximately equal to the advance rate of the liquidus isotherm, i.e. the laser scan speed, which is in the range of 5 ~ 20 mm/s.

6.3.2 Equiaxed grain microstructure

Fig. 6.2 (a) gives the inverse pole figure (IPF) image of an area of 700 μm by 700 μm taken in the XZ-plane of the LENS^{TM}-processed $AlCoCrFeNiTi_{0.5}$ specimen deposited at a laser power of 400 W and a laser scan speed of 5 mm/s. Each individual grain in the IPF image was color-coded according to the relationship between its crystallographic orientation and the building direction (BD), which was aligned vertically upwards. Obviously, there is no preferred crystallographic texture developed in the specimen because the grains were randomly color coded. Furthermore, it is interesting to note, from the IPF image, that the grains show perfect equiaxed morphologies in the XZ-plane. To fully reveal the grain microstructure in 3D space, the XZ-, YZ- and XY-planes were characterized by BSE imaging, and the results are shown in Fig. 6.2 (b). It can be clearly seen that the grains exhibit equiaxed morphologies in all of these three planes, and it is thus confirmed that fully equiaxed grain microstructures in 3D space are formed, rather than columnar grain microstructures which are more common for the AM-ed alloys [213, 228, 266-270]. The statistics show that grains with aspect ratio values larger than 0.3, which can be regarded as equiaxed grains, account for more than 95.5% of all grains in the scanned area (Fig. 6.2 (c)). The aspect ratio in the present paper refers to the ratio of the minor axis length to the major axis length of an ellipse fitted to an irregular grain. Moreover, the statistical grain size is Gaussian distributed with a mean value of 12 μm, as shown in Fig. 6.2 (d). It should be noted that the laser scan speed and laser power (5 ~ 20 mm/s, and 300 ~ 600 W, respectively) were also varied to deposit the $AlCoCrFeNiTi_{0.5}$ alloy, and a wide range of G and V values have been established (Fig. 6.1 (d)). However, similar fully equiaxed grain microstructures have been achieved, without any exception, despite a variation in grain size, as shown in Fig. 6.2 (e)). With the increase of the linear heat input (i.e. the quotient of the laser power and laser scan speed), the cooling rate (i.e. the product of G and V) decreases, which leads to coarser grains. It can be also observed that a critical linear heat input value may exist in this study, beyond which the cooling rate is steady in general and therefore the grain size variation is less pronounced. Anyway, it is confirmed in the present study that fully equiaxed grains dominate the solidification microstructure of the $LENS^{TM}$-deposited $AlCoCrFeNiTi_{0.5}$ alloy. To be more precise, it is the equiaxed solidification, rather than columnar solidification, that dominates the solidification process of the $AlCoCrFeNiTi_{0.5}$ alloy. Furthermore, it should be mentioned that the $LENS^{TM}$-deposited $AlCoCrFeNiTi_{0.5}$ specimens deposited at various laser powers and laser scan speeds show similar phase constitution and microstructure details. Therefore, only one specimen is shown in Sections 6.3.3. and 6.3.4. Unless otherwise stated, the specimen shown was deposited at a laser power of 400 W and a laser scan speed of 5 mm/s.

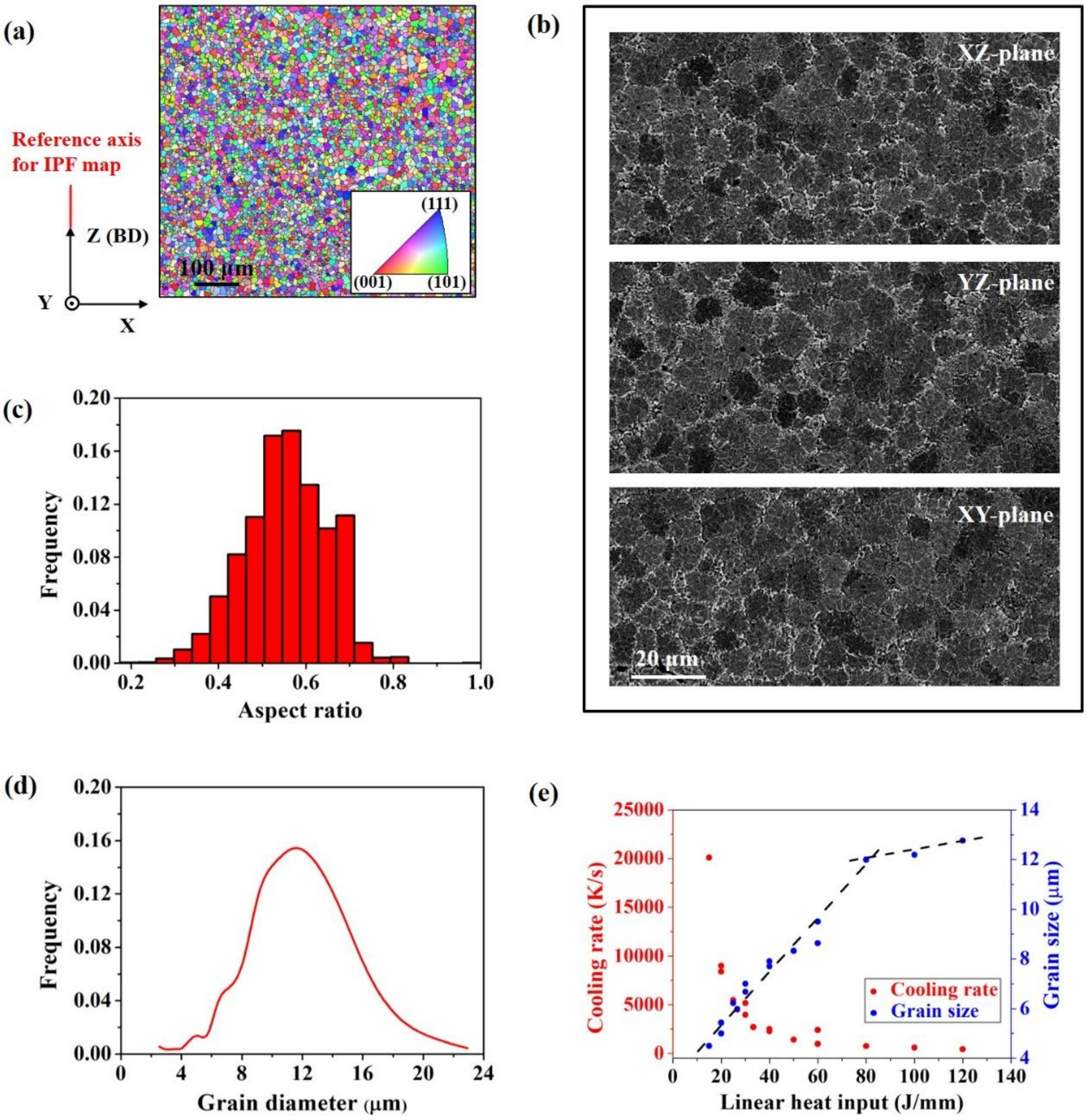

Fig. 6.2 (a) EBSD-IPF map of the XZ-plane, showing equiaxed grains in this section. (b) BSE images of XZ-, YZ- and XY-planes, confirming fully equiaxed grain microstructures in 3D space. (c) and (d) Statistics of the grain shape aspect ratio and grain size, respectively. (e) Cooling rate and grain size variations with linear heat inputs.

6.3.3 Phase constitution

Fig. 6.3 gives the XRD analysis of the LENS^{TM}-processed AlCoCrFeNiTi$_{0.5}$ alloy, with the examination surface being the XY-plane. Two BCC phases were detected: one is the ordered BCC-structured (B2) phase, and the other one is the disordered BCC-structured (A2) phase. More specifically, the microstructure of the LENS^{TM}-processed AlCoCrFeNiTi$_{0.5}$ specimen consists of B2 and A2 phases, which is consistent with that of the as-casted counterpart [12]. The lattice constants of the B2 and A2 phases were calculated to be a = 0.2912 nm and a = 0.2801 nm, respectively. Furthermore, it is observed from the inset that the diffraction peaks originating from the same crystal plane are very close to each other, due to the similar lattice constants of the two phases, in addition to a (100) superlattice peak at $2\theta \approx 30.7°$ originating from B2 phases.

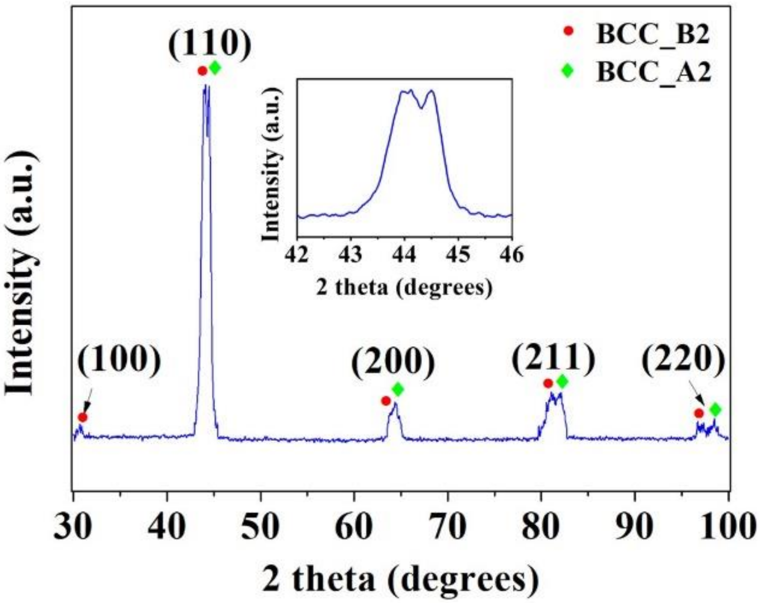

Fig. 6.3 XRD analysis of the LENS^{TM}-processed AlCoCrFeNiTi$_{0.5}$ alloy, with the examination surface being the XY-plane. The co-existence of ordered BCC-structured (B2) and disordered BCC-structured (A2) phases is confirmed. The inset shows an enlarged view of the strongest peak (110).

6.3.4 Microstructural details and compressive properties

Fig. 6.4 shows the microstructural details of the LENS^{TM}-deposited AlCoCrFeNiTi$_{0.5}$ specimen in the SEM BSE imaging mode. It can be clearly seen that the equiaxed grains are delineated by intergranular discrete bright phases (Fig. 6.4 (a)). Furthermore, the dendritic structure within each equiaxed grain can be seen. BSEs originate from the incident electrons which are back-scattered out of the specimen by specimen atoms. Therefore, phases with heavier elements (i.e. higher atomic number elements) more strongly backscatter electrons and appear brighter, in a BSE image, than phases with lighter elements (i.e. lower atomic number elements). To be more precise, the aforementioned bright phases must contain more heavier elements. Some eutectic structures were also observed, with lamellar or rod morphologies clinging to the edges of proeutectic dendrites (Fig. 6.4 (b)). Such eutectic structures and proeutectic dendrites belong to a single grain. Furthermore, eutectic cells were also observed at the grain boundaries, rather than adhering to the proeutectic dendrites, and these cells are believed to nucleate and grow independently at the very last stage of solidification. Therefore, these eutectic cells are new grains, which are separated with the adjacent dendrites by grain boundaries. A typical eutectic cell is marked in Fig. 6.4 (a).

Fig. 6.5 shows the EDS elemental distribution analysis of the $AlCoCrFeNiTi_{0.5}$ alloy. Recalling the phase identification and microstructural details, the bright phases are Cr-Fe-rich A2 phases, and the dark phases are the Ni-Al-Ti-rich B2 phases. Certainly, the eutectic structure is a mixture of B2 and A2 phases. It should be mentioned that in the dark B2 dendrites some bright needle-like precipitates are also formed (Fig. 6.4 (b)), although they are not detected by EDS due to its resolution limit. Similar decomposed microstructure is observed in the as-casted counterpart, and is attributed to spinodal decomposition of B2 dendrites into B2 plus A2 coexisting phases (i.e. a solid-state phase transformation process in nature) [59]. The microstructural evolution during solidification is discussed in section 6.4.1. Fig. 6.6 shows the typical compressive stress-strain curve of the LENS^{TM}-deposited AlCoCrFeNiTi$_{0.5}$ alloy tested at room temperature. It can be seen that this alloy exhibits a high yield strength and a high fracture strength, and fails at a strain of ~20%. The high strengths of the LENS^{TM}-deposited AlCoCrFeNiTi$_{0.5}$ alloy have been attributed to the hard B2+A2 phases.

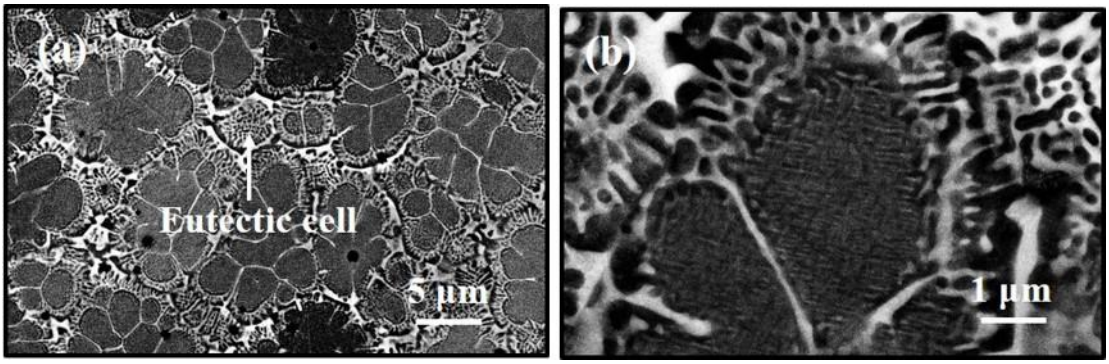

Fig. 6.4 BSE images of the LENS^{TM}-deposited AlCoCrFeNiTi$_{0.5}$ specimen showing microstructural details. (a) Low magnification BSE micrograph, showing equiaxed grains delineated by intergranular bright phases. A eutectic cell at grain boundary is also marked. (b) High magnification BSE image showing eutectic structures clinging to proeutectic dendrites.

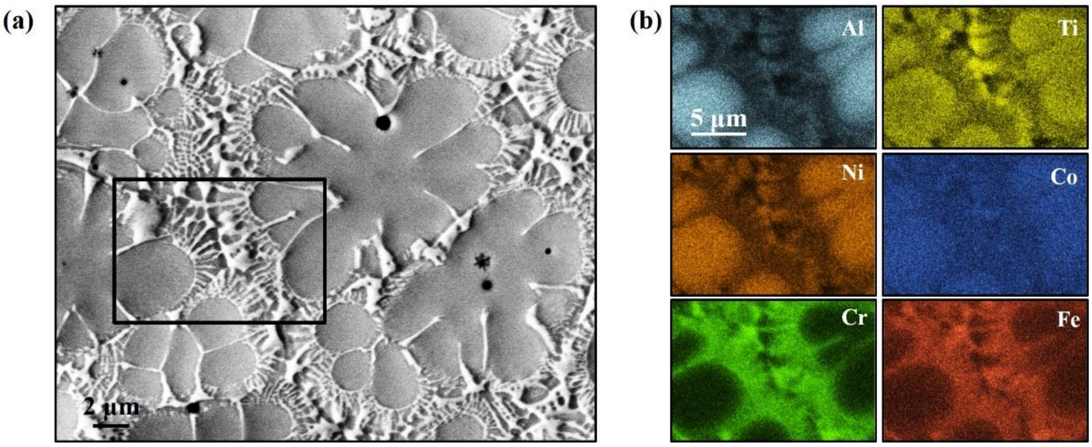

Fig. 6.5 EDS elemental distribution analysis of the AlCoCrFeNiTi$_{0.5}$ alloy. (a) SE image. (b) EDS elemental distribution of the rectangular region indicated in (a).

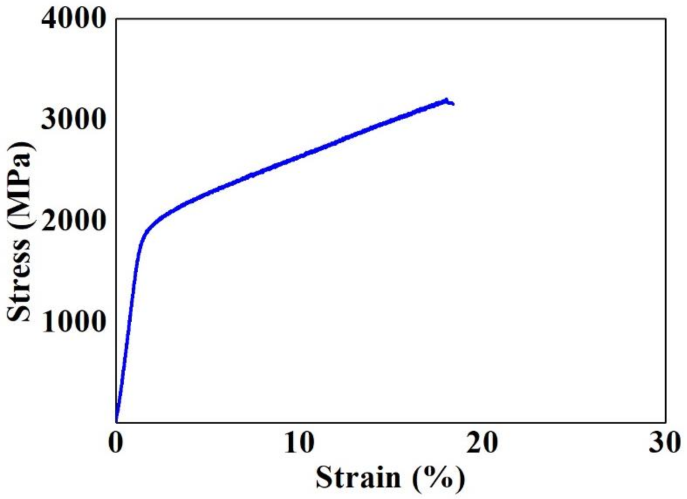

Fig. 6.6 Typical compressive stress-strain curve of the LENS^{TM}-deposited AlCoCrFeNiTi$_{0.5}$ alloy tested at room temperature.

6.4 Discussion

6.4.1 Microstructural evolution during solidification

The microstructural evolution during solidification is simulated using Scheil's model on the platform of Thermo-Calc software equipped with a HEA database. It should be noted that Scheil's solidification process is simulated, assuming no diffusion of any elements in the solid but infinite diffusion of all elements in the liquid. Fig. 6.7 (a) shows the mass fraction of the phases as a function of temperature during solidification. According to this diagram, the solidification mode is L→L + B2→L + B2 + A2. More specifically, when the temperature is above 1400 K (and below 1620 K), only the B2 phases solidify from the molten alloy, and the B2- and solid-curves coincide. At this stage, Cr, Fe, and Ti atoms are rejected into the remaining molten alloy, as can be seen in Fig. 6.7 (b). This means that the first solidified region is enriched in Ni and Al, and the later solidified region is enriched in Cr, Fe, and Ti. At 1400 K, only 12.6% molten alloy is left, and it reaches the eutectic composition. With further decrease of temperature, the B2 and A2 phases are predicted to solidify concurrently, i.e. the eutectic reaction L→B2 + A2.

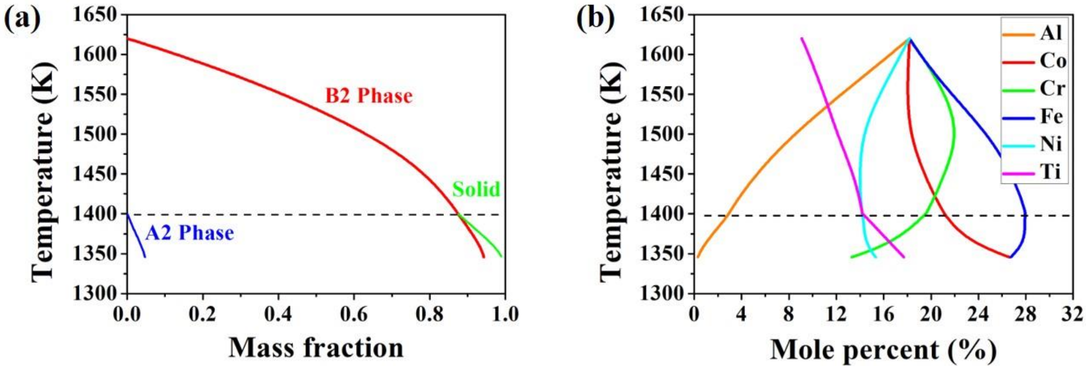

Fig. 6.7 Scheil's solidification simulation for the $AlCoCrFeNiTi_{0.5}$ alloy. (a) Mass fraction of phases plotted as a function of temperature. Solid refers to B2 plus A2 phases, and above 1400 K, B2- and solid-curves coincide. The solidification mode is L→L + B2→L + B2 + A2. (b) Compositional evolution of the liquid during solidification. The black dashed lines in (a) and (b) indicate the eutectic temperature.

6.4.2 Equiaxed grain formation mechanism

6.4.2.1 Density of nucleation sites vs. temperature gradient

The LENS^{TM}-deposited $AlCoCrFeNiTi_{0.5}$ alloy exhibits a fully equiaxed grain microstructure at various G - V combinations. This is surprising, and not consistent with commonly reported AM-ed HEAs [106, 111, 112, 114] and AM-ed conventional alloys [151, 153, 213, 228, 266-270]. As mentioned before, the G - V combinations associated with the AM process facilitate columnar solidification, and hence promote the formation of columnar grain microstructures [272]. More specifically, it is the very large G value that is responsible for the columnar solidification during the AM process. However, according to classic solidification theory, the high density of nucleation sites counteracts the large G value, and may lead to the formation of fully equiaxed grain microstructures [135, 142, 143, 271, 272, 275, 276]. There have been two experimental studies, to the best of our knowledge, demonstrating this counteracting effect [154, 277]. One example is the AM-ed Sc- and Zr-modified aluminum alloy prepared by Yang et al. [154]. After careful manipulation of the processing parameters (e.g. lower scan speed and higher platform temperature) and hence the solidification conditions (e.g. lower G value), they additively manufactured nearly equiaxed grain microstructures, thanks to the $Al_3(Sc,Zr)$ particles as heterogenous nucleation sites during solidification [154, 155]. Another example is shown in the paper by Martin et al. [277]. They decorated aluminum alloy powders with certain nanoparticles, which act as effective heterogenous nucleation sites and hence facilitate the formation of fully equiaxed grain microstructures during the AM process. These two experimental studies are very consistent with the classic solidification theory, and both experimental and theoretical studies show that a high density of nucleation sites makes it possible to form fully equiaxed grain microstructures in the AM process, despite a very extreme G value. Further investigations are therefore performed in our study to evaluate the density of nucleation sites in the $AlCoCrFeNiTi_{0.5}$ alloy and probe into their possible origins.

6.4.2.2 Nucleation

6.4.2.2.1 Estimation of density of nucleation sites

The density of nucleation sites N_0 can be evaluated by fitting the calculated volume fraction ϕ_{AM} of equiaxed grains in the final AM-ed specimen to the measured one. The calculated volume fraction ϕ_{AM} can be given by the following equation [143]:

$$\phi_{\mathrm{AM}} = 1 - \exp\left\{\frac{-4\pi N_0}{3\cdot\left[\sqrt[n]{\frac{G^n}{Va}}\cdot(n+1)\right]^3}\right\} \tag{6.1}$$

where a and n are material constants. This equation is valid for G in the order of 10^3 K/mm and V in the order of 10 mm/s. The measured volume fraction $\phi_{\mathrm{AM}} = 95.5\%$ of the equiaxed grains in the LENS$^{\mathrm{TM}}$-manufactured specimen has been determined by EBSD analysis. Therefore, the density of nucleation sites N_0 is estimated to be a minimum of 3×10^9 /mm^3 (i.e. $N_0 \geq 3 \times 10^9$ /mm^3), assuming $a = 1.25 \times 10^3$ K$^{3.4}$ s/mm and $n = 3.4$, as shown in Fig. 6.8. In other words, only when the N_0 value reaches or exceeds 3×10^9 /mm^3, fully equiaxed grain microstructures can be achieved. Therefore, 3×10^9 /mm^3 is a very conservative N_0 value. Anyway, this conservatively estimated $N_0 = 3 \times 10^9$ /mm^3 is already very large as compared with those of previously researched alloys, such as the Al alloys (e.g. Al - 3 wt.% Cu, $N_0 = 1$ /mm^3 [272]), Cu alloys (e.g. Cu with rare earth microalloying, $N_0 = 5$ /mm^3 [278]), and Ni-based superalloys (e.g. CMSX-4, $N_0 = 2 \times 10^6$ /mm^3 [143]).

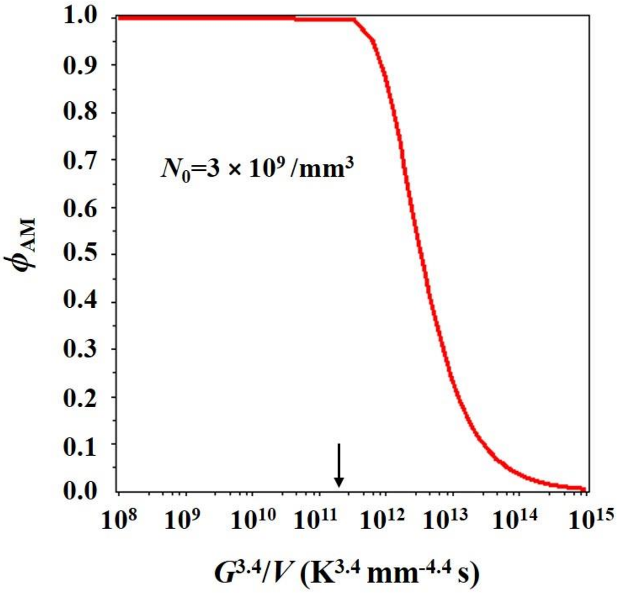

Fig. 6.8 Determination of the density of nucleation sites N_0 by fitting the calculated volume fraction ϕ_{AM} of equiaxed grains in the final AM-ed specimen to the measured one. The G and V values used are approximately corresponding to the melt pool bottom. The black arrow indicates the maximum $G^{3.4}/V$ value established in this work.

6.4.2.2.2 Origin of nucleation sites

Fig. 6.5 (a) shows that the A2 phases frequently isolate the dendritic arms from their primary stalks, and even split individual grains in two, i.e. a dendrite fragmentation phenomenon during solidification. Such fragmented dendrites should be formed in the very last stage of solidification, when only a minor amount of liquid exists. Therefore, these fragments cannot move freely and have to remain close to their primary stalks. Fig. 6.9 (a), (b), and (c) show the image quality (IQ), kernel average misorientation (KAM), and IPF maps, respectively. In the IPF map, high angle grain boundaries (HAGBs, misorientation > 15°) and low angle grain boundaries (LAGBs, 2° < misorientation < 15°) are highlighted in black and red, respectively. Fortunately, this examined region contains a split grain and a LAGB is formed inside (i.e. the red line in Fig. 6.9 (c)). That means the fragments formed at the last stage of solidification merely experience a small degree of rotation and are not responsible for the new grain formation. However, dendrite fragmentation is predicted to be more frequent at the earlier stage of solidification, and fragments are able to move freely within the mushy zone, or even move out of the mushy zone and into the hot liquid. When these fragments flow out of the mushy zone and contact the hot liquid, they start to dissolve or even disappear. However, the fragments that are merely partially dissolved or are still within the mushy zone can be effective nucleation sites for new grains. According to the results of Scheil's solidification simulation, the solidification range of the experimental

$AlCoCrFeNiTi_{0.5}$ alloy is 275 K, which is quite large for fragments to survive. Such freely mobile dendrite fragments are more effective "nucleant agents" as compared with deliberately introduced nucleating agents (e.g. $Al_3(Sc,Zr)$ nucleants in aluminum alloys) because dendrite fragments exhibit exactly the same crystal structure and lattice parameter as the solidifying alloys. Furthermore, dendrite fragmentation is a multiplication process, rather than a gradual consumption process, which can produce increasingly more "nucleant agents". More direct observation of dendrite fragmentation and subsequent growth into new grains can be found in the literature dealing with casting and welding processes [162, 163, 279]. Overall, we believe that the frequent dendrite fragmentation is the main origin of the large density of nucleation sites of the $AlCoCrFeNiTi_{0.5}$ alloy.

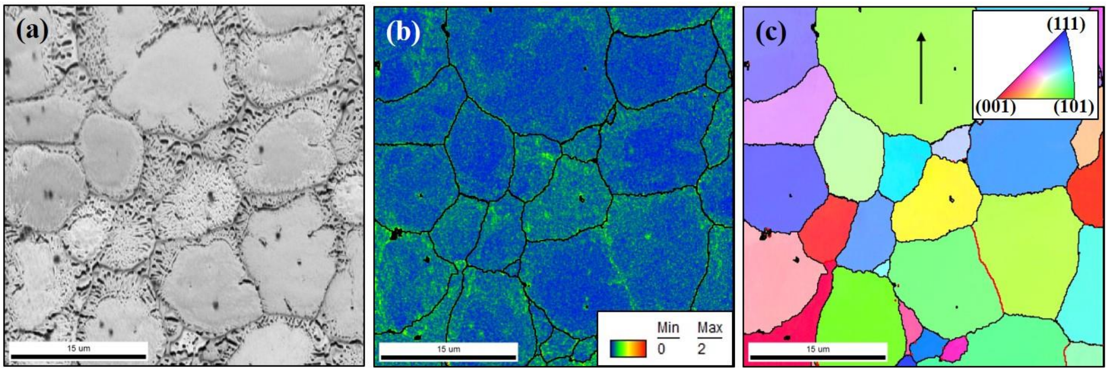

Fig. 6.9 (a) IQ map. (b) KAM image. (c) IPF map with HAGBs and LAGBs highlighted in black and red, respectively. Note figures (a), (b) and (c) were obtained from the same region of 40 μm by 40 μm.

6.4.2.3 Equiaxed grain microstructure formation: A theoretical analysis

To further understand the formation of the equiaxed grain microstructure, the volume fraction ϕ of the equiaxed crystals at solidification front is estimated for various G - V

combinations established in this study, with the aid of Gäumann's model [272]. This model considers high velocity effects, and can be used for rapid solidification, e.g. AM processes. The basic physics behind this model is that during columnar dendritic solidification, the solutes pile up in front of the moving solid-liquid interface, assuming a distribution coefficient of < 1. Therefore, the local concentration field and the local equilibrium solidification temperature ahead of the solidification interface will be affected. In this case, a constitutionally undercooled region will be established at the dendrite tip, possibly leading to the nucleation and growth of equiaxed crystals. When the volume fraction ϕ of these equiaxed crystals exceeds a critical value (i.e. 49%, as proposed by Hunt [271]), the columnar growth will be prohibited and a fully equiaxed grain microstructure will be achieved.

Gäumann's model [272] assumes the columnar dendrite growth at marginal stability, and therefore the dendritic tip radius R_{tip} can be given by:

$$\frac{\Gamma}{\sigma^* R_{\mathrm{tip}}^2} = \sum_{i=1}^{n-1} m_{\mathrm{V,i}} \zeta_{\mathrm{C,i}} G_{\mathrm{C,i}} - G \tag{6.2}$$

where Γ is the Gibbs-Thomson coefficient, $\sigma^*=1/(4\pi^2)$ is a stability constant, $m_{\mathrm{V,i}}$ is the liquidus slope of component i which is velocity dependent, $\zeta_{\mathrm{C,i}}$ is the stability parameter of component i, $G_{\mathrm{C,i}}$ is the concentration gradient of component i in the liquid at the dendritic tip. The parameters $m_{\mathrm{V,i}}$, $\zeta_{\mathrm{C,i}}$, and $G_{\mathrm{C,i}}$, are given by following equations:

$$m_{\mathrm{V,i}} = m_{\mathrm{i}} \left\{ 1 + \frac{k_{\mathrm{i}} - k_{\mathrm{V,i}}\left[1 - \ln\left(k_{\mathrm{V,i}}/k_{\mathrm{i}}\right)\right]}{1 - k_{\mathrm{i}}} \right\} \tag{6.3}$$

$$\zeta_{\mathrm{C,i}} = 1 - \frac{2k_{\mathrm{V,i}}}{\left[1 + \left(\frac{1}{\sigma^* Pe_{\mathrm{i}}^2}\right)\right]^{1/2} - 1 + 2k_{\mathrm{V,i}}} \tag{6.4}$$

$$G_{\mathrm{C,i}} = -\frac{\left(1 - k_{\mathrm{V,i}}\right) V C_{\mathrm{tip,i}}}{D_{\mathrm{i}}} \tag{6.5}$$

where m_i and k_i are the equilibrium liquidus slope and equilibrium partition coefficient of component *i*, respectively, $k_{V,i}$ is the partition coefficient which is velocity dependent, Pe_i is the solute Péclet number of component *i*, $C_{tip,i}$ is the concentration of component *i* in the liquid at the dendrite tip, D_i is the diffusion coefficient of component *i* in the liquid. The parameters $k_{V,i}$, Pe_i, $C_{tip,i}$, and D_i are given by:

$$k_{\mathrm{V,i}} = \frac{D_{\mathrm{i}} k_{\mathrm{i}} + a_0 V}{D_{\mathrm{i}} + a_0 V} \tag{6.6}$$

$$Pe_{\mathrm{i}} = \frac{V R_{\mathrm{tip}}}{2 D_{\mathrm{i}}} \tag{6.7}$$

$$C_{\mathrm{tip,i}} = \frac{C_{0,\mathrm{i}}}{1 - \left(1 - k_{\mathrm{V,i}}\right) I_v(Pe_{\mathrm{i}})} \tag{6.8}$$

$$D_{\mathrm{i}} = D_{0,\mathrm{i}} \cdot \exp\left(\frac{-Q_{\mathrm{i}}}{R_{\mathrm{g}} T}\right) \tag{6.9}$$

where a_0 is the characteristic length scale for solute trapping, $C_{0,i}$ is the nominal concentration of component *i*, $D_{0,i}$ is the diffusion factor of component *i*, Q_i is the activation energy of component *i*, R_g = 8.314 $\mathrm{J \cdot K^{-1} \cdot mol^{-1}}$ is the gas constant, I_v is the Ivantsov function, $I_v(Pe_{\mathrm{i}}) = Pe_{\mathrm{i}} \cdot \exp(Pe_{\mathrm{i}}) \cdot E_1(Pe_{\mathrm{i}})$, and E_1 is the exponential integral function, i.e. $E_1(Pe_{\mathrm{i}}) = \int_{Pe_{\mathrm{i}}}^{\infty} \frac{e^{-\mathrm{t}}}{t} dt$. Then the dendrite tip temperature T_{tip} can be calculated by:

$$T_{\text{tip}} = T_{\text{m}} + \sum_{i=1}^{n-1} m_{\text{V,i}}\, C_{\text{tip,i}} - \frac{2\Gamma}{R_{\text{tip}}} - \frac{V}{\mu_{\text{k}}} \tag{6.10}$$

where T_m is the melting temperature of pure metal, and μ_k is the linear kinetic coefficient. Solving Eqs. (6.2)-(6.10), we can achieve the dendrite tip temperature T_{tip}, the concentration of each component in the liquid at the dendrite tip $C_{tip,i}$, and the dendrite tip radius R_{tip} for a given G and V. Then the actual temperature profile in the liquid $T(z)$ can be achieved:

$$T(z) = T_{\text{tip}} + G \cdot z \tag{6.11}$$

where z is the distance from the dendrite tip. Furthermore, the concentration profile of component i in the liquid, $C_i(z)$, and the corresponding liquidus temperature profile, $T_{liquidus}(z)$, are given by:

$$C_{\text{i}}(z) = C_{0,\text{i}} + \left(C_{\text{tip,i}} - C_{0,\text{i}}\right) \cdot \frac{E_1\left[Pe_{\text{i}}\left(2z + R_{\text{tip}}\right)/R_{\text{tip}}\right]}{E_1(Pe_{\text{i}})} \tag{6.12}$$

$$T_{\text{liquidus}}(z) = T_{\text{L}} + \sum_{i=1}^{n-1} m_{\text{i}}\, [C_{\text{i}}(z) - C_{0,\text{i}}] \tag{6.13}$$

where T_L is the equilibrium liquidus temperature corresponding to the initial composition. The local undercooling profile, $\Delta T(z)$, ahead of the moving solid-liquid interface is therefore given by:

$$\Delta T(z) = T_{\text{liquidus}}(z) - T(z) \tag{6.14}$$

The equiaxed grains may nucleate and grow in this undercooled region, and their volume fraction can be achieved by estimating the maximum radius of an individual equiaxed grain (i.e. the radius of an individual equiaxed grain when the columnar dendrite passes). The size of each equiaxed grain R_e is given by:

$$R_{\mathrm{e}} = \int_0^{z_{\mathrm{n}}} \frac{V_{\mathrm{e}}(z)}{V} dz \tag{6.15}$$

where z_n is the distance from the solid-liquid interface to the position, where the local undercooling equals the nucleation undercooling, i.e. $\Delta T(z_n)=\Delta T_n$, and $V_e(z)$ is the growth velocity of the equiaxed grains which can be calculated by:

$$V_{\mathrm{e}}(z) = \frac{A \cdot [\Delta T(z)]^2}{\sum_{i=1}^{n-1} C_{\mathrm{i}}(z)} \tag{6.16}$$

If we assume the dendritic equiaxed grains grow in a spherical mode, the extended volume fraction of the equiaxed grains ϕ_e can be given by:

$$\phi_{\mathrm{e}} = \frac{4\pi R_{\mathrm{e}}^3 N_0}{3} \tag{6.17}$$

where N_0 is again the density of nucleation sites. Then the actual volume fraction of the equiaxed grains ϕ can be estimated by Avarami equation:

$$\phi = 1 - \exp(-\phi_e) \tag{6.18}$$

The thermophysical parameters associated with this model were largely achieved using Thermo-Calc software equipped with a HEA database, and are shown in Table 6.1. The ϕ values are calculated to be greater than 49% for various G - V combinations established in this paper, assuming $N_0 = 3 \times 10^9$ /mm^3. This indicates that columnar growth will be completed prohibited, by the large amount of equiaxed crystals at the solidification front, and finally a fully equiaxed grain microstructure can be formed, which supports our experimental findings (Fig. 6.3).

Table 6.1 Thermophysical parameters associated with Gäumann's model (largely achieved by CALPHAD method on the platform of Thermo-Calc software equipped with HEA thermodynamic database).

	Al	Co	Cr	Fe	Ti
$C_{0,i}$ (at.%)	18.2	18.2	18.2	18.2	9.1
k_i	1.675	0.964	0.574	0.665	0.554
m_i (K/at.%)	9.740	2.102	-1.495	-1.841	-4.017
$D_{0,i}$ (m^2/s)	1.51×10^{-7}	2.30×10^{-7}	2.20×10^{-7}	2.29×10^{-7}	2.08×10^{-7}
Q_i (J/mol)	4.63×10^4	6.54×10^4	6.65×10^4	6.51×10^4	6.08×10^4

6.5 Conclusions

The senary non-equi-atomic HEA AlCoCrFeNiTi$_{0.5}$ was additively manufactured by the LENS^{TM} technique in this chapter. The solidification conditions, grain morphology, phase constitution and microstructural details were investigated, and the underlying mechanisms were explained. The following conclusions can be drawn:

(1) The increase of laser traverse speed or the decrease of laser power leads to a larger temperature gradient. Through the manipulation of the laser traverse speed and laser power, we have established a wide range of temperature gradients (i.e. 85 to 1005 K/mm).

(2) The microstructure of the LENS^{TM}-deposited $AlCoCrFeNiTi_{0.5}$ alloy consists of proeutectic B2-structured dendrites delineated by lamellar or rod-like B2/A2 eutectic structures which cling to the proeutectic dendrites. Furthermore, the B2 and A2 phases can nucleate and grow independently at the grain boundaries to form eutectic cells. Such microstructures have been successfully described with the aid of Scheil's solidification model.

(3) Proeutectic B2-structured grains are totally equiaxed and randomly textured. A high density of nucleation sites (a minimum of 3×10^9 /mm^3) is estimated, and attributed to frequent dendrite fragmentation. The volume fraction ϕ values of equiaxed crystals at solidification front are estimated to be greater than 49% for various G - V combinations established in this paper. This indicates that fully equiaxed grain microstructures can be formed, and therefore provides a theoretical basis for our experimental findings.

Chapter 7 Additively manufactured laminated high entropy alloy CrMnFeCoNi/AlCoCrFeNiTi$_{0.5}$ with enhanced strength-plasticity synergy

7.1 Introduction

Conventional metals and alloys typically show a paradox of strength and plasticity. High-entropy alloys (HEAs) are no exceptions, although they define a new compositional space [20]. More specifically, face-centered-cubic (FCC) structured HEAs are ductile, but typically not very strong [1, 11]. In contrast, body-centered-cubic (BCC) structured HEAs are strong, but normally sacrifice plasticity [21, 59, 60]. Our previous chapters of the AM-ed FCC HEA CrMnFeCoNi and BCC HEA AlCoCrFeNiTi$_{0.5}$ also show this trade-off. Lamination could be used to integrate multi-materials (i.e. multi-phases) and so achieve the desired mechanical properties, suggesting an alternative but more flexible approach to prepare high-performance HEAs. Lamination has been reported to bond constituent alloy foils, sheets or plates, through methods such as diffusion bonding [280], reaction bonding [17, 281, 282] and deformation bonding [283-287] processes. Obviously, it is important to use high-quality starting constituent alloys with desirable microstructures (e.g. fine grains). In certain processes (e.g. deformation bonding), fine microstructures can be achieved in-situ due to severe plastic deformation [283-286, 288]. However, such processes are not applicable for certain hard alloys that are brittle and sensitive to cracking. Furthermore, these lamination techniques only generate simple geometries. In contrast, additive manufacturing (AM) produces 3D complex-shaped parts layer-upon-layer and may be an alternative lamination route. What’s more, the highly localized (i.e. localized into melt pools) melting and solidification processes associated with the AM process generate unique microstructures that are not accessible through conventional metallurgical routes. It is therefore possible that complex-shaped parts manufacturing, multiple alloys lamination and desirable microstructures formation can be integrated in the AM process.

In this chapter, we synthesize a laminated HEA CrMnFeCoNi/AlCoCrFeNiTi$_{0.5}$ by alternate deposition on a layered basis, on the platform of LENS^{TM} MR 7 System. This laminated HEA exhibits enhanced strength-plasticity synergy. The as-deposited microstructure is analyzed, and correlated to the high strength and large macroscopic plasticity achieved. This study demonstrates a feasible and flexible way to achieve HEAs with superior mechanical properties.

7.2 Materials and methods

LENS^{TM} processing, a typical laser powder-blown AM process, was also used in this chapter. This process is used to produce a 3D part by blowing metal powders into a small-sized melt pool that is created by a focused laser, as schematically shown in Fig. 7.1 (a). Both constituent powders are perfectly spherical, of a <140 μm diameter (Fig. 7.1 (b) and (c)). To achieve the laminated structure, these two powders were loaded into separate powder feeders, and were alternately blown on a layered basis. Bidirectional scans along the Y-axis for the CrMnFeCoNi lamellae and along the X-axis for the AlCoCrFeNiTi$_{0.5}$ lamellae were used (Fig. 7.1 (d) and (e)), with the following process parameters: laser power 400 W, scan speed 5 mm/s, hatch spacing 460 μm. The melt pool was monitored by a two-wavelength imaging pyrometer that enables high resolution (12.1 μm/pixel) and real-time (25 frames/s) temperature measurements up to 3073 K. The as-deposited laminated HEA was examined using optical microscopy (OM), scanning electron microscopy (SEM) and electron backscatter diffraction (EBSD). Vickers microhardness (HV) tests were performed at a load of 0.5 kgf and a hold of 15 s. The compressive tests were performed on rectangular specimens (1.7 mm by 1.7 mm by 3.4 mm), at room temperature and at a strain rate of 10^{-3} s^{-1}, with the load axis normal or parallel to the laminate plane (i.e. XY-plane).

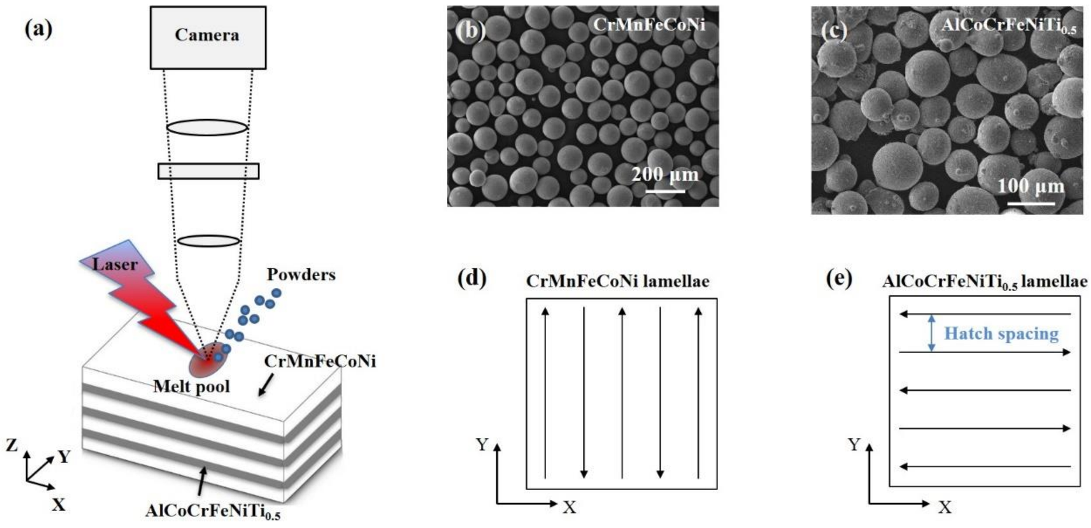

Fig. 7.1 Synthesis of CrMnFeCoNi/$AlCoCrFeNiTi_{0.5}$ laminated HEA via the $LENS^{TM}$ process. (a) Schematic of the lamination process via the $LENS^{TM}$ technique. (b) CrMnFeCoNi and (c) $AlCoCrFeNiTi_{0.5}$ prealloyed powders. Bidirectional scans (d) along the Y-axis for the CrMnFeCoNi lamellae and (e) along the X-axis for the $AlCoCrFeNiTi_{0.5}$ lamellae.

7.3 Results and discussion

Fig. 7.2 (a) shows a well-defined laminated structure, with bright CrMnFeCoNi lamellae and dark $AlCoCrFeNiTi_{0.5}$ lamellae. The CrMnFeCoNi/$AlCoCrFeNiTi_{0.5}$

interfaces are clear, but develop some waviness (i.e. melt pool boundary) that is intrinsic to the AM process. These wavy interfaces lead to nonuniform layer thickness, despite their continuity. The CrMnFeCoNi lamellae and $AlCoCrFeNiTi_{0.5}$ lamellae were measured to be 65% and 35%, respectively, based on their area fractions. The larger area fraction of CrMnFeCoNi is attributed to its higher powder feed rates used in this study. The EBSD inverse pole figure (IPF) map in Fig. 7.2 (b) reveals the formation of columnar grains in the CrMnFeCoNi lamellae and equiaxed grains in the $AlCoCrFeNiTi_{0.5}$ lamellae, leading to an abrupt grain microstructure transition across the interfaces. The formation of columnar grains is very common for the AM-ed conventional alloys [228, 270], and has also been reported for the AM-ed CrMnFeCoNi HEA [112, 119]. This has been attributed to the strong temperature gradient (measured to be 207 K/mm) associated with the AM process. The determination of temperature gradients and cooling rates has been introduced in chapters 4, 5 and 6. Similarly, the equiaxed grains are formed in the $AlCoCrFeNiTi_{0.5}$ lamellae. As analyzed and discussed in chapter 6, the $AlCoCrFeNiTi_{0.5}$ HEA exhibits a strong tendency to form equiaxed grain microstructures, despite the large temperature gradients experienced in the AM process, due to frequent dendrite fragmentation and hence a large density of nucleation sites. The numerous nucleation sites can promote the formation of a large volume fraction of equiaxed crystals ahead of the solidification front, and hence block the growth of columnar grains if any. This is very consistent with our experimental observation that a few slightly elongated grains are formed at the bottom of the $AlCoCrFeNiTi_{0.5}$ lamellae (i.e. near to the CrMnFeCoNi → $AlCoCrFeNiTi_{0.5}$ interfaces), and are soon replaced by equiaxed grains (Fig. 7.2 (b)). Furthermore, rapid quenching effects of the order of 10^3 K/s result in very fine grain microstructures in both constituent alloys. Based on high angle grain boundaries (HAGBs, in black) in the

IPF map, the average columnar grain width in the CrMnFeCoNi lamellae was determined to be 24 μm and the average equiaxed grain diameter in the $AlCoCrFeNiTi_{0.5}$ lamellae was determined to be 7 μm. It can also be observed from the IPF map that both constituent alloys show very random crystallographic textures evidenced by the random grain colors.

Fig. 7.2 (c) gives the EBSD phase map of the same area, showing that the CrMnFeCoNi lamellae are FCC structured, whereas the $AlCoCrFeNiTi_{0.5}$ lamellae consist of major BCC phases plus a small amount of FCC phases. Comparing the IPF and phase map figures, we find that these discrete FCC phases are primarily distributed at the grain boundaries of the major BCC phases. Some discrete grain boundary FCC phases are also observed in the BSE image and are indicated in Fig. 7.2 (f). It should be noted that the $AlCoCrFeNiTi_{0.5}$ HEA was reported to be free of FCC phases [59, 202]. Concerning this point, the formation of FCC phases in the $AlCoCrFeNiTi_{0.5}$ lamellae is ascribed to the introduction of a small amount of CrMnFeCoNi constituents (Fig. 7.3), through partial remelting of the previous layer followed by simultaneous solidification. Moreover, very good metallurgical bonding is achieved at the CrMnFeCoNi/$AlCoCrFeNiTi_{0.5}$ interfaces (Fig. 7.2 (d), (e) and (f)), and no obvious defects (e.g. oxide particles, frequently observed in diffusion-bonded laminates [289, 290]) are formed. Finally, the remarkable differences in the phases and microstructures across the CrMnFeCoNi/$AlCoCrFeNiTi_{0.5}$ interfaces lead to a distinct difference in microhardness, with 197 HV in the CrMnFeCoNi lamellae and 657 HV in the $AlCoCrFeNiTi_{0.5}$ lamellae.

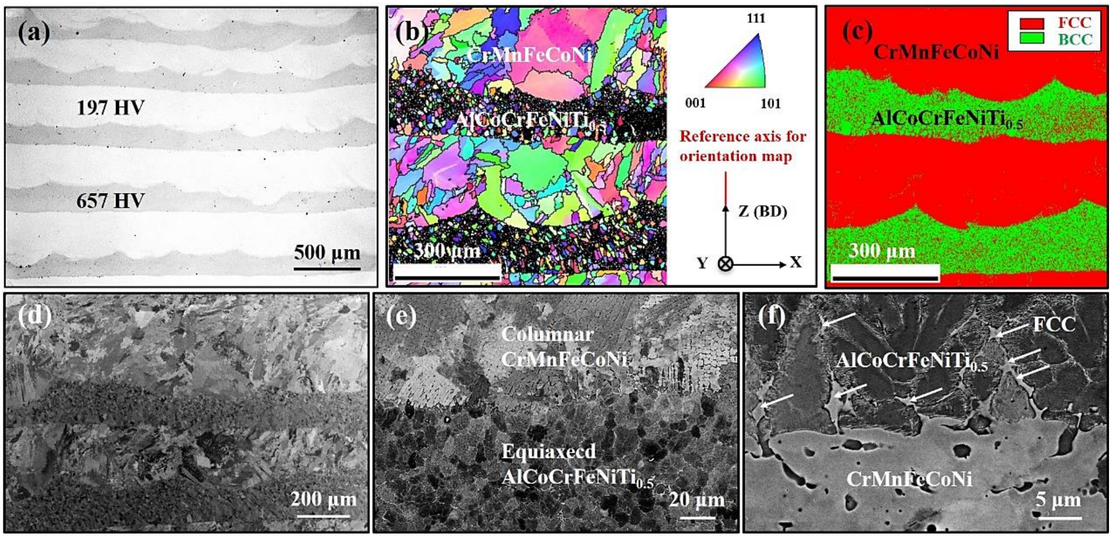

Fig. 7.2 Microstructures of the LENS^{TM}-deposited CrMnFeCoNi/AlCoCrFeNiTi$_{0.5}$ laminate composite HEA observed on a XZ cross-section. (a) OM micrograph of a well-defined laminate. (b) EBSD IPF map of alternating columnar and equiaxed grain microstructures. The reference axis is the build direction, i.e. Z-axis. (c) EBSD phase map of FCC and BCC phases. (d), (e) and (f) BSE micrographs indicating well-bonded CrMnFeCoNi/AlCoCrFeNiTi$_{0.5}$ interfaces. The arrows in (f) indicate some discrete FCC phases at the substantial BCC's grain boundaries.

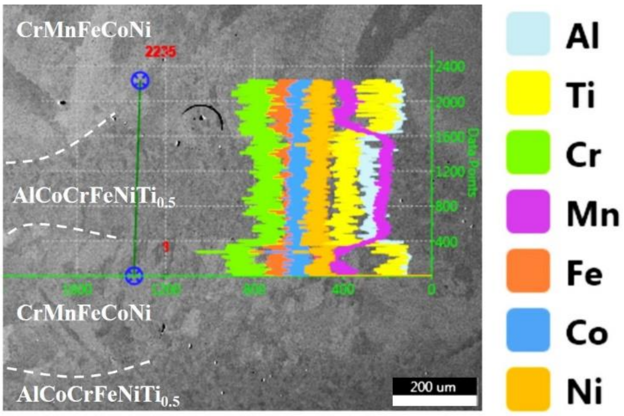

Fig. 7.3 EDS line scan across a complete AlCoCrFeNiTi$_{0.5}$ lamella. The CrMnFeCoNi/AlCoCrFeNiTi$_{0.5}$ interfaces are marked by white dashed lines for better clearness.

Typical compressive stress-strain curves corresponding to both loading cases of the CrMnFeCoNi/AlCoCrFeNiTi$_{0.5}$ laminated HEA are plotted in Fig. 7.4. It is noted that this laminated HEA exhibits a remarkable combination of yield strength and macroscopic plasticity, surpassing those of conventional laminates, e.g. Ti/Al$_3$Ti [17], Al/Al$_2$O$_3$ [291] and Al/graphene [292]. The yield strengths of this laminated HEA are anisotropic, and were determined to be ~ 888 and 990 MPa, respectively, for normal and parallel loading cases. For the parallel loading case (i.e. an iso-strain case), the strong AlCoCrFeNiTi$_{0.5}$ lamellae carry the load, and the soft CrMnFeCoNi lamellae only transfer the load to the AlCoCrFeNiTi$_{0.5}$ lamellae, resulting in a harder orientation and hence a higher yield strength, which is similar to what was observed for conventional laminated alloys [17, 291, 292]. The yield strength of the laminated alloys has been previously reported to scale with the volume fractions and yield strengths of constituent alloys, i.e. rule of mixture [293]. Hence, the compressive properties of the CrMnFeCoNi HEA and the AlCoCrFeNiTi$_{0.5}$ HEA fabricated by the LENS^{TM} process were also tested, and are shown in Fig. 7.4. No obvious anisotropic compressive properties were found for these two constituent alloys, and this may be attributed to the random crystallographic textures developed in both alloys. Assuming the rule of mixture, where $\sigma_{\mathrm{ys}} = f_1 \cdot \sigma_{\mathrm{ys,1}} + f_2 \cdot \sigma_{\mathrm{ys,2}}$ (f_{i} represents the volume fraction of constituent *i*; $\sigma_{\mathrm{ys,i}}$ represents the yield strength of constituent *i*), the yield strength of this laminated HEA is calculated to be 847 MPa. This value constitutes a substantial portion of the measured yield strength, especially for the normal loading case, suggesting that the high yield strength of this laminated HEA primarily originates from the high-strength AlCoCrFeNiTi$_{0.5}$ lamellae that are BCC structured and fine equiaxed-grained. Furthermore, we note that this laminated HEA shows a substantial and steady work hardening mechanism and hence good macroscopic plasticity, without premature complete fracture. In contrast, conventional laminated alloys, e.g. the Ti/Al_3Ti laminate, completely fractured when compressed to a few percent strain [17, 291].

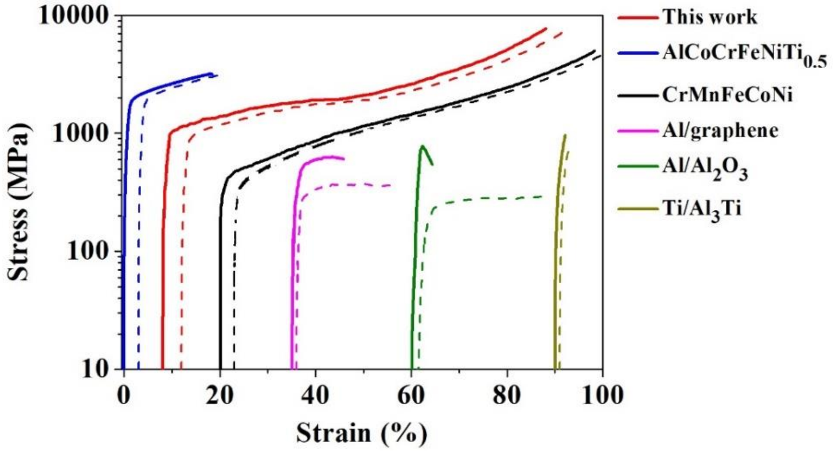

Fig. 7.4 Typical compressive stress-strain curves of the CrMnFeCoNi/AlCoCrFeNiTi$_{0.5}$ laminated HEA synthesized by the LENS^{TM} process, compared to those of LENS^{TM}-deposited CrMnFeCoNi HEA and AlCoCrFeNiTi$_{0.5}$ HEA and those of conventional laminates [17, 291, 292]. The compressive tests of the CrMnFeCoNi/AlCoCrFeNiTi$_{0.5}$ laminated HEA and the LENS^{TM}-deposited CrMnFeCoNi HEA were stopped at ~ 80% strain. The solid and dashed curves are corresponding to parallel and normal loading cases, respectively. For a better comparison, the stress-strain curves are somewhat shifted towards the right.

To understand the origin of the resistance to complete failure of this laminated HEA, multi-cycle loading-unloading compressive tests were performed, and after each cycle, the specimen was ex-situ examined by SEM (Fig. 7.5). When the load axis is normal to the laminate plane, damage evolves by transverse (i.e. normal to the interfaces) cracking within the AlCoCrFeNiTi$_{0.5}$ lamellae (Fig. 7.5 (a1)). Interestingly, these transverse cracks normally terminate at the interfaces. Furthermore, some smaller and discrete transverse cracks are also formed in the vicinity of the main crack (Fig. 7.5 (a2)). With straining, more transverse cracks are formed within the AlCoCrFeNiTi$_{0.5}$ lamellae, and the earlier cracks broaden (Fig. 7.5 (b1)). Note that these cracks do not connect and are bridged by the ductile CrMnFeCoNi lamellae. Furthermore, it is noted that the tips of the cracks generate shear bands in the adjacent CrMnFeCoNi lamellae (Fig. 7.5 (b2)). This indicates that strain localization, rather than homogenous deformation, has occurred in the CrMnFeCoNi lamellae. With further straining, the shear bands initiated by two separate cracks may connect (Fig. 7.5 (c1) and (c2)), and finally shear cracks are formed in the ductile CrMnFeCoNi lamellae (Fig. 7.5 (d1) and (d2)). For such a loading case (i.e. an iso-stress case), the rigid AlCoCrFeNiTi$_{0.5}$ lamellae delay the occurrence of macro-plastic deformation and hence delay the yielding of the complete specimen. During straining, the soft CrMnFeCoNi lamellae in turn bridge the cracked AlCoCrFeNiTi$_{0.5}$ lamellae and hence avoid premature complete failure of the specimen.

When the load axis is parallel to the laminate plane, damage evolves by longitudinal (i.e. parallel to the interfaces) cracking within the brittle AlCoCrFeNiTi$_{0.5}$ lamellae (Fig. 7.5 (e1) and (f1)). Such longitudinal cracks are believed to nucleate from both ends which directly contact the crossheads. The larger cracks may branch into several smaller cracks which finally terminate at the interfaces (Fig. 7.5 (e2) and (f2)). With straining, frequent crushing was observed in the AlCoCrFeNiTi$_{0.5}$ lamellae (Fig. 7.5 (g2) and (h2)). Furthermore, it is interesting to note that the right side AlCoCrFeNiTi$_{0.5}$ lamella seems to buckle together with adjacent CrMnFeCoNi lamellae, and the CrMnFeCoNi/AlCoCrFeNiTi$_{0.5}$ interfaces are surprisingly intact during straining (Fig. 7.5 (g1) and (h1)). This is beyond expectation, and as reported in Refs [17, 282], it is more common that delamination occurs along the interfaces and then the ductile lamellae bend independently. Overall speaking, for both loading orientations, the soft CrMnFeCoNi lamellae desirably bridge the cracked $AlCoCrFeNiTi_{0.5}$ lamellae, and the good interfacial metallurgical bonding effectively prevents the interfacial failure, both of which prevent premature complete failure of this laminated HEA.

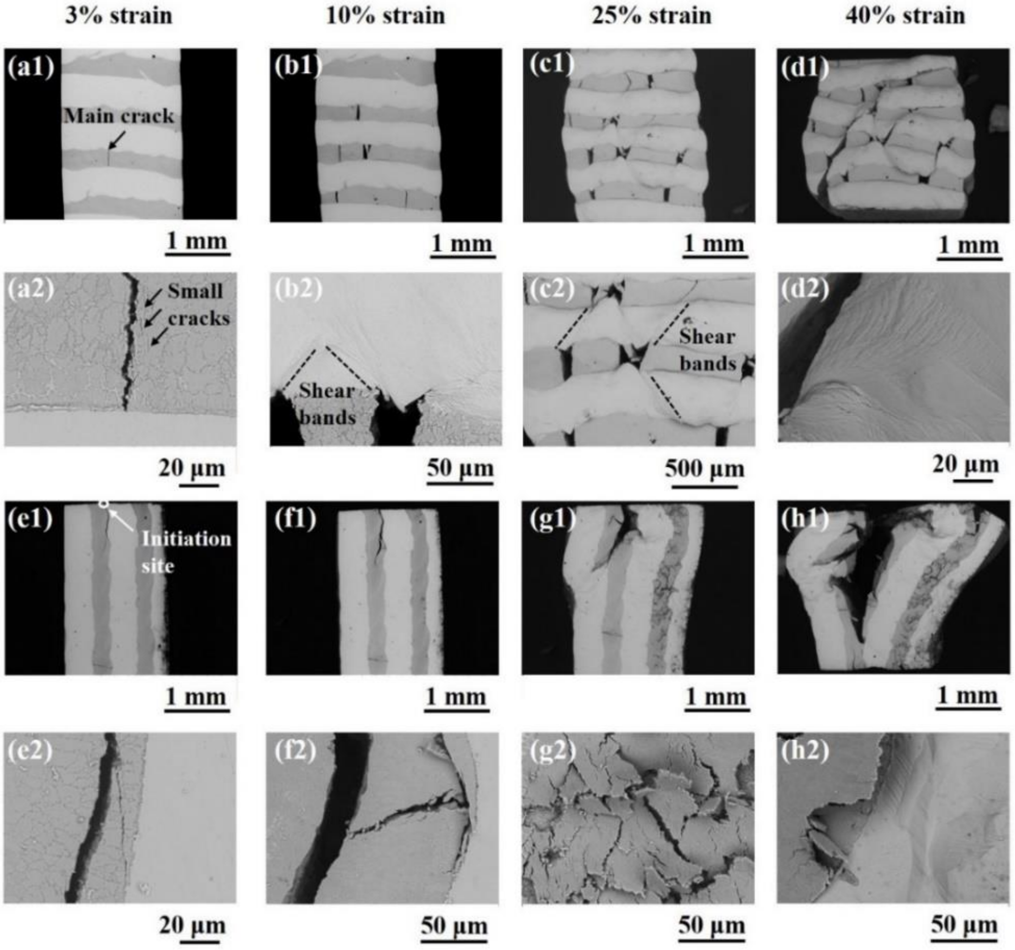

Fig. 7.5 SEM micrographs showing the progressive damage evolution of the $CrMnFeCoNi/AlCoCrFeNiTi_{0.5}$ laminated HEA during compression, with the load axis normal (a1 – d2) or parallel (e1 – h2) to the laminate plane. The corresponding strain values are indicated at the top. (a2 – d2) and (e2 – h2) are a magnified view of the characteristics in (a1 – d1) and (e1 – h1), respectively.

7.4 Conclusions

To sum up, the CrMnFeCoNi/AlCoCrFeNiTi$_{0.5}$ laminated HEA was additively manufactured by the LENS^{TM} process in this chapter, and this material exhibits a remarkable combination of yield strength and macroscopic plasticity during compression. The rule of mixture reveals that the high-strength AlCoCrFeNiTi$_{0.5}$ lamellae with hard BCC phases and fine equiaxed grains is a major contributor to the high yield strength of this laminated HEA. The ex-situ damage evolution investigation reveals that the soft CrMnFeCoNi lamellae effectively bridge the cracked AlCoCrFeNiTi$_{0.5}$ lamellae, and the good interfacial metallurgical bonding prevents the interfacial delamination, which are believed to be the main origin of the large macroscopic plasticity achieved. This study demonstrates an alternative approach for achieving high-performance HEAs.

Chapter 8 Overall conclusions

In this project, several alloy systems (i.e. CrCoNi, CrMnFeCoNi, $AlCoCrFeNiTi_{0.5}$ and a laminated alloy $CrMnFeCoNi/AlCoCrFeNiTi_{0.5}$) were additively manufactured by the $LENS^{TM}$ process. The following conclusions can be drawn from this project:

(1) The ternary equi-atomic CrCoNi alloy was additively manufactured by the $LENS^{TM}$ process at varied laser scan speeds, and special focus was given to fundamental research problems, e.g. melt pool solidification, grain structure and cracking behavior. The $LENS^{TM}$-processed CrCoNi alloy exhibits a single-phase FCC solid solution structure as evidenced by XRD and rationalized by Scheil's solidification simulation. The increased laser scan speed generates more heterogenous grain structures. To be more specific, the grain structure varies from columnar to columnar plus equiaxed when the laser scan speed increases from 10 to 50 mm/s. Furthermore, the increased laser scan speed achieves more pronounced quenching effects and hence generates finer celluar spacing. A quantitative relationship between the cooling rate and celluar spacing has been established. Furthermore, the increased laser scan speed generates more dislocations and promotes the formation of the stacking faults. The CrCoNi alloy shows a low susceptibility to solidification cracking and crack-free CrCoNi alloys can be successfully printed by the $LENS^{TM}$ process. However, the high laser scan speed creates a large thermal gradient and hence a high thermal stress that can still trigger solidification cracking of the CrCoNi alloy.

(2) The quinary equi-atomic HEA CrMnFeCoNi was also additively manufactured by

the LENS^{TM} process, and the solidification conditions, phase formation, as-deposited microstructures and tensile behavior were investigated by a combinatorial approach. The LENS^{TM}-deposited CrMnFeCoNi alloy exhibits a single-phase disordered face centered cubic structure, as evidenced by XRD, and rationalized by Scheil's solidification simulation with the aid of the high entropy alloys database. Multi-scale as-deposited microstructures, i.e. columnar grains, solidification and dislocation substructures, are formed. Furthermore, elemental segregation is observed and rationalized by Scheil's simulation. The LENS^{TM}-deposited CrMnFeCoNi alloy exhibits a tensile yield strength that is comparable to that of finer-grained wrought-annealed counterparts. This is largely attributed to the high dislocation density and hence the enhanced initial-dislocation strengthening of the LENS^{TM}-deposited CrMnFeCoNi alloy. The tensile deformation process is mainly accommodated by dislocation activities with the assistance of deformation twinning. The promoted dislocation recovery process during straining leads to a weakened work hardening capability and hence a reduced uniform tensile elongation of the LENS^{TM}-deposited CrMnFeCoNi alloy, as compared with the wrought-annealed counterparts.

(3) A senary non-equi-atomic HEA AlCoCrFeNiTi$_{0.5}$ was additively manufactured by the LENS^{TM} process. The increase of laser traverse speed or the decrease of laser power leads to a larger temperature gradient. Through the manipulation of the laser traverse speed and laser power, we have established a wide range of temperature gradients (i.e. 85 to 1005 K/mm). The microstructure of the LENS^{TM}-deposited AlCoCrFeNiTi$_{0.5}$ alloy consists of proeutectic B2-structured dendrites delineated by lamellar or rod-like B2/A2 eutectic structures which cling to the proeutectic dendrites. Furthermore, the B2 and A2 phases can nucleate and grow independently at the grain boundaries to form

eutectic cells. Such microstructures have been successfully described with the aid of Scheil's solidification model. Furthermore, proeutectic B2-structured grains are totally equiaxed and randomly textured. A high density of nucleation sites (a minimum of 3×10^9 /mm^3) is estimated, and is attributed to frequent dendrite fragmentation. The volume fraction ϕ values of equiaxed crystals at the solidification front are estimated to be greater than 49% for the various G - V combinations established in this study, indicating that fully equiaxed grain microstructures can be formed, hence providing a theoretical basis for our experimental findings.

(4) Finally, the laminated HEA CrMnFeCoNi/AlCoCrFeNiTi$_{0.5}$ was additively manufactured by the LENS^{TM} process, and this material exhibits a remarkable combination of yield strength and macroscopic plasticity during compression. The rule of mixtures reveals that the high-strength AlCoCrFeNiTi$_{0.5}$ lamellae with hard BCC phases and fine equiaxed grains is a major contributor to the high yield strength of this laminated HEA. The ex-situ damage evolution investigation reveals that the soft CrMnFeCoNi lamellae effectively bridge the cracked AlCoCrFeNiTi$_{0.5}$ lamellae, and the good interfacial metallurgical bonding prevents interfacial delamination, which is believed to be the main origin of the large macroscopic plasticity achieved. This study demonstrates an alternative approach for achieving high-performance HEAs.

Chapter 9 Suggested future work

9.1 Synthesize multi-phase HEAs with enhanced properties

In this project, research has been conducted on the microstructures and mechanical behavior of two HEAs. Although important results have been achieved, the strength-ductility trade-off of AM-ed HEAs also exists. In order to achieve an improved strength-ductility synergy, the HEAs should exhibit a multi-phase microstructure comprising both hard and soft phases. Therefore, future work will be directed towards the exploration of more candidate HEAs with desirable phase combinations and enhanced properties for the AM process.

9.2 Synthesize new AM-ed laminated HEAs with outstanding mechanical properties

We have proven that lamination is a very effective approach to achieve improved strength-ductility synergy. In the future, we will try more laminated AM-ed HEAs with varied printing (e.g. laser power and laser scan speed) and lamination parameters (e.g. volume fraction of constituent materials).

References

[1] B. Gludovatz, A. Hohenwarter, D. Catoor, E.H. Chang, E.P. George, R.O. Ritchie, A fracture-resistant high-entropy alloy for cryogenic applications, Science 345 (2014) 1153-1158.

[2] A. Takeuchi, K. Amiya, T. Wada, K. Yubuta, W. Zhang, High-entropy alloys with a hexagonal close-packed structure designed by equi-atomic alloy strategy and binary phase diagrams, JOM 66 (2014) 1984-1992.

[3] M.C. Gao, B. Zhang, S.M. Guo, J.W. Qiao, J.A. Hawk, High-entropy alloys in hexagonal close-packed structure, Metall. Mater. Trans. A 47 (2016) 3322-3332.

[4] Y.-J. Liang, L. Wang, Y. Wen, B. Cheng, Q. Wu, T. Cao, Q. Xiao, Y. Xue, G. Sha, Y. Wang, Y. Ren, X. Li, L. Wang, F. Wang, H. Cai, High-content ductile coherent nanoprecipitates achieve ultrastrong high-entropy alloys, Nat. Commun. 9 (2018) 4063.

[5] J.R. Strife, D.E. Passoja, The effect of heat-treatment on microstructure and cryogenic fracture properties in 5Ni and 9Ni steel, Metall. Trans. A 11 (1980) 1341-1350.

[6] Z. Tang, T. Yuan, C.-W. Tsai, J.-W. Yeh, C.D. Lundin, P.K. Liaw, Fatigue behavior of a wrought $Al_{0.5}CoCrCuFeNi$ two-phase high-entropy alloy, Acta Mater. 99 (2015) 247-258.

[7] Z. Wu, H. Bei, G.M. Pharr, E.P. George, Temperature dependence of the mechanical properties of equiatomic solid solution alloys with face-centered cubic crystal structures, Acta Mater. 81 (2014) 428-441.

[8] Z. Wu, H. Bei, F. Otto, G.M. Pharr, E.P. George, Recovery, recrystallization, grain growth and phase stability of a family of FCC-structured multi-component equiatomic

solid solution alloys, Intermetallics 46 (2014) 131-140.

[9] W. Ji, W.M. Wang, H. Wang, J.Y. Zhang, Y.C. Wang, F. Zhang, Z.Y. Fu, Alloying behavior and novel properties of CoCrFeNiMn high-entropy alloy fabricated by mechanical alloying and spark plasma sintering, Intermetallics 56 (2015) 24-27.

[10] Y. Zou, H. Ma, R. Spolenak, Ultrastrong ductile and stable high-entropy alloys at small scales, Nat. Commun. 6 (2015).

[11] W.H. Liu, Y. Wu, J.Y. He, T.G. Nieh, Z.P. Lu, Grain growth and the Hall-Petch relationship in a high-entropy FeCrNiCoMn alloy, Scr. Mater. 68 (2013) 526-529.

[12] Y.J. Zhou, Y. Zhang, Y.L. Wang, G.L. Chen, Solid solution alloys of AlCoCrFeNiTix with excellent room-temperature mechanical properties, Appl. Phys. Lett. 90 (2007) 181904.

[13] X.Z. Gao, Y.P. Lu, B. Zhang, N.N. Liang, G.Z. Wu, G. Sha, J.Z. Liu, Y.H. Zhao, Microstructural origins of high strength and high ductility in an $AlCoCrFeNi_{2.1}$ eutectic high-entropy alloy, Acta Mater. 141 (2017) 59-66.

[14] P.J. Shi, W.L. Ren, T.X. Zheng, Z.M. Ren, X.L. Hou, J.C. Peng, P.F. Hu, Y.F. Gao, Y.B. Zhong, P.K. Liaw, Enhanced strength-ductility synergy in ultrafine-grained eutectic high-entropy alloys by inheriting microstructural lamellae, Nat. Commun. 10 (2019).

[15] Y.M. Wang, T. Voisin, J.T. McKeown, J.C. Ye, N.P. Calta, Z. Li, Z. Zeng, Y. Zhang, W. Chen, T.T. Roehling, R.T. Ott, M.K. Santala, P.J. Depond, M.J. Matthews, A.V. Hamza, T. Zhu, Additively manufactured hierarchical stainless steels with high strength and ductility, Nat. Mater. 17 (2018) 63.

[16] D. Embury, O. Bouaziz, Steel-based composites: driving forces and classifications, Annu. Rev. Mater. Res. 40 (2010) 213-241.

[17] A. Rohatgi, D.J. Harach, K.S. Vecchio, K.P. Harvey, Resistance-curve and fracture

behavior of Ti-Al_3Ti metallic-intermetallic laminate (MIL) composites, Acta Mater. 51 (2003) 2933-2957.

[18] Y. Li, Q. Zhou, S. Zhang, P. Huang, K. Xu, F. Wang, T. Lu, On the role of weak interface in crack blunting process in nanoscale layered composites, Appl. Surf. Sci. 433 (2018) 957-962.

[19] B. Cantor, I.T.H. Chang, P. Knight, A.J.B. Vincent, Microstructural development in equiatomic multicomponent alloys, Mater. Sci. Eng. A 375-377 (2004) 213-218.

[20] J.W. Yeh, S.K. Chen, S.J. Lin, J.Y. Gan, T.S. Chin, T.T. Shun, C.H. Tsau, S.Y. Chang, Nanostructured high-entropy alloys with multiple principal elements: novel alloy design concepts and outcomes, Adv. Eng. Mater. 6 (2004) 299-303.

[21] O.N. Senkov, G.B. Wilks, J.M. Scott, D.B. Miracle, Mechanical properties of $Nb_{25}Mo_{25}Ta_{25}W_{25}$ and $V_{20}Nb_{20}Mo_{20}Ta_{20}W_{20}$ refractory high entropy alloys, Intermetallics 19 (2011) 698-706.

[22] J.M. Park, J. Choe, J.G. Kim, J.W. Bae, J. Moon, S. Yang, K.T. Kim, J.-H. Yu, H.S. Kim, Superior tensile properties of 1%C-CoCrFeMnNi high-entropy alloy additively manufactured by selective laser melting, Mater. Res. Lett. (2019) 1-7.

[23] F.X. Zhang, S.J. Zhao, K. Jin, H. Bei, D. Popov, C. Park, J.C. Neuefeind, W.J. Weber, Y.W. Zhang, Pressure-induced fcc to hcp phase transition in Ni-based high entropy solid solution alloys, Appl. Phys. Lett. 110 (2017).

[24] B. Gludovatz, A. Hohenwarter, K.V.S. Thurston, H. Bei, Z. Wu, E.P. George, R.O. Ritchie, Exceptional damage-tolerance of a medium-entropy alloy CrCoNi at cryogenic temperatures, Nat. Commun. 7 (2016).

[25] Y. Zhang, T.T. Zuo, Z. Tang, M.C. Gao, K.A. Dahmen, P.K. Liaw, Z.P. Lu, Microstructures and properties of high-entropy alloys, Prog. Mater Sci. 61 (2014) 1-93.

[26] J.-W. Yeh, Alloy Design Strategies and Future Trends in High-Entropy Alloys,

JOM 65 (2013) 1759-1771.

[27] Y. Zhang, Y.J. Zhou, J.P. Lin, G.L. Chen, P.K. Liaw, Solid-solution phase formation rules for multi-component alloys, Adv. Eng. Mater. 10 (2008) 534-538.

[28] C. Zhu, Z.P. Lu, T.G. Nieh, Incipient plasticity and dislocation nucleation of FeCoCrNiMn high-entropy alloy, Acta Mater. 61 (2013) 2993-3001.

[29] Y. Brif, M. Thomas, I. Todd, The use of high-entropy alloys in additive manufacturing, Scr. Mater. 99 (2015) 93-96.

[30] Y. Deng, C.C. Tasan, K.G. Pradeep, H. Springer, A. Kostka, D. Raabe, Design of a twinning-induced plasticity high entropy alloy, Acta Mater. 94 (2015) 124-133.

[31] C. Li, J.C. Li, M. Zhao, Q. Jiang, Effect of alloying elements on microstructure and properties of multiprincipal elements high-entropy alloys, J. Alloys Compd. 475 (2009) 752-757.

[32] N.N. Guo, L. Wang, L.S. Luo, X.Z. Li, Y.Q. Su, J.J. Guo, H.Z. Fu, Microstructure and mechanical properties of refractory MoNbHfZrTi high-entropy alloy, Mater. Des. 81 (2015) 87-94.

[33] O.N. Senkov, J.M. Scott, S.V. Senkova, D.B. Miracle, C.F. Woodward, Microstructure and room temperature properties of a high-entropy TaNbHfZrTi alloy, J. Alloys Compd. 509 (2011) 6043-6048.

[34] S. Maiti, W. Steurer, Structural-disorder and its effect on mechanical properties in single-phase TaNbHfZr high-entropy alloy, Acta Mater. 106 (2016) 87-97.

[35] Z. Li, K.G. Pradeep, Y. Deng, D. Raabe, C.C. Tasan, Metastable high-entropy dual-phase alloys overcome the strength-ductility trade-off, Nature 534 (2016) 227.

[36] T.F. Yang, S.Q. Xia, S. Liu, C.X. Wang, S.S. Liu, Y. Zhang, J.M. Xue, S. Yan, Y.G. Wang, Effects of Al addition on microstructure and mechanical properties of AlxCoCrFeNi High-entropy alloy, Mater. Sci. Eng. A 648 (2015) 15-22.

[37] A. Manzoni, H. Daoud, R. Volkl, U. Glatzel, N. Wanderka, Phase separation in equiatomic AlCoCrFeNi high-entropy alloy, Ultramicroscopy 132 (2013) 212-215.

[38] Z. Tang, O.N. Senkov, C.M. Parish, C. Zhang, F. Zhang, L.J. Santodonato, G. Wang, G. Zhao, F. Yang, P.K. Liaw, Tensile ductility of an AlCoCrFeNi multi-phase high-entropy alloy through hot isostatic pressing (HIP) and homogenization, Mater. Sci. Eng. A 647 (2015) 229-240.

[39] W.R. Wang, W.L. Wang, J.W. Yeh, Phases, microstructure and mechanical properties of AlxCoCrFeNi high-entropy alloys at elevated temperatures, J. Alloys Compd. 589 (2014) 143-152.

[40] W.R. Wang, W.L. Wang, S.C. Wang, Y.C. Tsai, C.H. Lai, J.W. Yeh, Effects of Al addition on the microstructure and mechanical property of AlxCoCrFeNi high-entropy alloys, Intermetallics 26 (2012) 44-51.

[41] C. Li, J.C. Li, M. Zhao, Q. Jiang, Effect of aluminum contents on microstructure and properties of AlxCoCrFeNi alloys, J. Alloys Compd. 504 (2010) S515-S518.

[42] A. Munitz, S. Salhov, S. Hayun, N. Frage, Heat treatment impacts the micro-structure and mechanical properties of AlCoCrFeNi high entropy alloy, J. Alloys Compd. 683 (2016) 221-230.

[43] N. Tsuno, S. Shimabayashi, K. Kakehi, C.M.F. Rae, R.C. Reed, Tension/compression asymmetry in yield and creep strengths of Ni-based superalloys, 2008.

[44] X.D. Xu, P. Liu, S. Guo, A. Hirata, T. Fujita, T.G. Nieh, C.T. Liu, M.W. Chen, Nanoscale phase separation in a fcc-based CoCrCuFeNiAl$_{0.5}$ high-entropy alloy, Acta Mater. 84 (2015) 145-152.

[45] J.Y. He, H. Wang, H.L. Huang, X.D. Xu, M.W. Chen, Y. Wu, X.J. Liu, T.G. Nieh, K. An, Z.P. Lu, A precipitation-hardened high-entropy alloy with outstanding tensile

properties, Acta Mater. 102 (2016) 187-196.

[46] I.S. Wani, T. Bhattacharjee, S. Sheikh, Y.P. Lu, S. Chatterjee, P.P. Bhattacharjee, S. Guo, N. Tsuji, Ultrafine-grained AlCoCrFe$Ni_{2.1}$ eutectic high-entropy alloy, Mater. Res. Lett. 4 (2016) 174-179.

[47] I.S. Wani, T. Bhattacharjee, S. Sheikh, I.T. Clark, M.H. Park, T. Okawa, S. Guo, P.P. Bhattacharjee, N. Tsuji, Cold-rolling and recrystallization textures of a nano-lamellar AlCoCrFe$Ni_{2.1}$ eutectic high entropy alloy, Intermetallics 84 (2017) 42-51.

[48] I.S. Wani, T. Bhattacharjee, S. Sheikh, P.P. Bhattacharjee, S. Guo, N. Tsuji, Tailoring nanostructures and mechanical properties of AlCoCrFe$Ni_{2.1}$ eutectic high entropy alloy using thermo-mechanical processing, Mater. Sci. Eng. A 675 (2016) 99-109.

[49] T.H. Wang, M. Komarasamy, S. Shukla, R.S. Mishra, Simultaneous enhancement of strength and ductility in an AlCoCrFe$Ni_{2.1}$ eutectic high-entropy alloy via friction stir processing, J. Alloys Compd. 766 (2018) 312-317.

[50] Y. Lu, Y. Dong, S. Guo, L. Jiang, H. Kang, T. Wang, B. Wen, Z. Wang, J. Jie, Z. Cao, H. Ruan, T. Li, A promising new class of high-temperature alloys: eutectic high-entropy alloys, Sci. Rep. 4 (2014).

[51] S.G. Ma, Y. Zhang, Effect of Nb addition on the microstructure and properties of AlCoCrFeNi high-entropy alloy, Mater. Sci. Eng. A 532 (2012) 480-486.

[52] R. Zhou, Y. Liu, C.S. Zhou, S.Q. Li, W.Q. Wu, M. Song, B. Liu, X.P. Liang, P.K. Liaw, Microstructures and mechanical properties of C-containing FeCoCrNi high-entropy alloy fabricated by selective laser melting, Intermetallics 94 (2018) 165-171.

[53] R. Zhou, Y. Liu, B. Liu, J. Li, Q. Fang, Precipitation behavior of selective laser melted FeCoCrNi$C_{0.05}$ high entropy alloy, Intermetallics 106 (2019) 20-25.

[54] W. Wu, R. Zhou, B. Wei, S. Ni, Y. Liu, M. Song, Nanosized precipitates and

dislocation networks reinforced C-containing CoCrFeNi high-entropy alloy fabricated by selective laser melting, Mater. Charact. 144 (2018) 605-610.

[55] Y. Zhang, T. Zuo, Y. Cheng, P.K. Liaw, High-entropy alloys with high saturation magnetization, electrical resistivity, and malleability, Sci. Rep. 3 (2013).

[56] S.W. Wu, G. Wang, Q. Wang, Y.D. Jia, J. Yi, Q.J. Zhai, J.B. Liu, B.A. Sun, H.J. Chu, J. Shen, P.K. Liaw, C.T. Liu, T.Y. Zhang, Enhancement of strength-ductility trade-off in a high-entropy alloy through a heterogeneous structure, Acta Mater. 165 (2019) 444-458.

[57] J.M. Zhu, H.M. Fu, H.F. Zhang, A.M. Wang, H. Li, Z.Q. Hu, Microstructures and compressive properties of multicomponent AlCoCrFeNiMox alloys, Mater. Sci. Eng. A 527 (2010) 6975-6979.

[58] Y. Zou, S. Maiti, W. Steurer, R. Spolenak, Size-dependent plasticity in an $Nb_{25}Mo_{25}Ta_{25}W_{25}$ refractory high-entropy alloy, Acta Mater. 65 (2014) 85-97.

[59] Y.J. Zhou, Y. Zhang, T.N. Kim, G.L. Chen, Microstructure characterizations and strengthening mechanism of multi-principal component $AlCoCrFeNiTi_{0.5}$ solid solution alloy with excellent mechanical properties, Mater. Lett. 62 (2008) 2673-2676.

[60] Y. Yu, J. Wang, J. Li, H. Kou, W. Liu, Characterization of BCC phases in AlCoCrFeNiTix high entropy alloys, Mater. Lett. 138 (2015) 78-80.

[61] Y.J. Zhou, Y. Zhang, F.J. Wang, Y.L. Wang, G.L. Chen, Effect of Cu addition on the microstructure and mechanical properties of $AlCoCrFeNiTi_{0.5}$ solid-solution alloy, J. Alloys Compd. 466 (2008) 201-204.

[62] Y.F. Ye, C.T. Liu, Y. Yang, A geometric model for intrinsic residual strain and phase stability in high entropy alloys, Acta Mater. 94 (2015) 152-161.

[63] S. Guo, C. Ng, J. Lu, C.T. Liu, Effect of valence electron concentration on stability of fcc or bcc phase in high entropy alloys, J. Appl. Phys. 109 (2011).

[64] S. Fang, X. Xiao, L. Xia, W. Li, Y. Dong, Relationship between the widths of supercooled liquid regions and bond parameters of Mg-based bulk metallic glasses, J. Non-Cryst. Solids 321 (2003) 120-125.

[65] A. Takeuchi, A. Inoue, Quantitative evaluation of critical cooling rate for metallic glasses, Mater. Sci. Eng. A 304-306 (2001) 446-451.

[66] W. Huang, P. Martin, H.L. Zhuang, Machine-learning phase prediction of high-entropy alloys, Acta Mater. 169 (2019) 225-236.

[67] J.Y. He, C. Zhu, D.Q. Zhou, W.H. Liu, T.G. Nieh, Z.P. Lu, Steady state flow of the FeCoNiCrMn high entropy alloy at elevated temperatures, Intermetallics 55 (2014) 9-14.

[68] B. Schuh, F. Mendez-Martin, B. Voelker, E.P. George, H. Clemens, R. Pippan, A. Hohenwarter, Mechanical properties, microstructure and thermal stability of a nanocrystalline CoCrFeMnNi high-entropy alloy after severe plastic deformation, Acta Mater. 96 (2015) 258-268.

[69] E.J. Pickering, R. Muñoz-Moreno, H.J. Stone, N.G. Jones, Precipitation in the equiatomic high-entropy alloy CrMnFeCoNi, Scr. Mater. 113 (2016) 106-109.

[70] F. Otto, A. Dlouhy, K.G. Pradeep, M. Kubenova, D. Raabe, G. Eggeler, E.P. George, Decomposition of the single-phase high-entropy alloy CrMnFeCoNi after prolonged anneals at intermediate temperatures, Acta Mater. 112 (2016) 40-52.

[71] F. Otto, Y. Yang, H. Bei, E.P. George, Relative effects of enthalpy and entropy on the phase stability of equiatomic high-entropy alloys, Acta Mater. 61 (2013) 2628-2638.

[72] N. Park, B.J. Lee, N. Tsuji, The phase stability of equiatomic CoCrFeMnNi high-entropy alloy: comparison between experiment and calculation results, J. Alloys Compd. 719 (2017) 189-193.

[73] M.G. Poletti, L. Battezzati, Electronic and thermodynamic criteria for the

occurrence of high entropy alloys in metallic systems, Acta Mater. 75 (2014) 297-306.

[74] V. Raghavan, Al-Co-Cr-Ni (aluminum-cobalt-chromium-nickel), J. Phase Equilib. Diff. 27 (2006) 408-409.

[75] H. Shahmir, J.Y. He, Z.P. Lu, M. Kawasaki, T.G. Langdon, Effect of annealing on mechanical properties of a nanocrystalline CoCrFeNiMn high-entropy alloy processed by high-pressure torsion, Mater. Sci. Eng. A 676 (2016) 294-303.

[76] S. Singh, N. Wanderka, B.S. Murty, U. Glatzel, J. Banhart, Decomposition in multi-component AlCoCrCuFeNi high-entropy alloy, Acta Mater. 59 (2011) 182-190.

[77] L.J. Santodonato, Y. Zhang, M. Feygenson, C.M. Parish, M.C. Gao, R.J.K. Weber, J.C. Neuefeind, Z. Tang, P.K. Liaw, Deviation from high-entropy configurations in the atomic distributions of a multi-principal-element alloy, Nat. Commun. 6 (2015).

[78] X.L. Liu, G. Lindwall, T. Gheno, Z.K. Liu, Thermodynamic modeling of Al-Co-Cr, Al-Co-Ni, Co-Cr-Ni ternary systems towards a description for Al-Co-Cr-Ni, Calphad 52 (2016) 125-142.

[79] D. Ma, B. Grabowski, F. Kormann, J. Neugebauer, D. Raabe, Ab initio thermodynamics of the CoCrFeMnNi high entropy alloy: importance of entropy contributions beyond the configurational one, Acta Mater. 100 (2015) 90-97.

[80] D. Ma, M. Yao, K.G. Pradeep, C.C. Tasan, H. Springer, D. Raabe, Phase stability of non-equiatomic CoCrFeMnNi high entropy alloys, Acta Mater. 98 (2015) 288-296.

[81] T. Omori, J. Sato, K. Shinagawa, I. Ohnuma, K. Oikawa, R. Kainuma, K. Ishida, Experimental determination of phase equilibria in the Co-Cr-Ni system, J. Phase Equilib. Diff. 35 (2014) 178-185.

[82] Z. Zhang, M.M. Mao, J. Wang, B. Gludovatz, Z. Zhang, S.X. Mao, E.P. George, Q. Yu, R.O. Ritchie, Nanoscale origins of the damage tolerance of the high-entropy alloy CrMnFeCoNi, Nat. Commun. 6 (2015).

[83] M.J. Jang, S.H. Joo, C.W. Tsai, J.W. Yeh, H.S. Kim, Compressive deformation behavior of CrMnFeCoNi high-entropy alloy, Met. Mater. Int. 22 (2016) 982-986.

[84] G. Laplanche, A. Kostka, O.M. Horst, G. Eggeler, E.P. George, Microstructure evolution and critical stress for twinning in the CrMnFeCoNi high-entropy alloy, Acta Mater. 118 (2016) 152-163.

[85] G. Laplanche, A. Kostka, C. Reinhart, J. Hunfeld, G. Eggeler, E.P. George, Reasons for the superior mechanical properties of medium-entropy CrCoNi compared to high-entropy CrMnFeCoNi, Acta Mater. 128 (2017) 292-303.

[86] J. Miao, C.E. Slone, T.M. Smith, C. Niu, H. Bei, M. Ghazisaeidi, G.M. Pharr, M.J. Mills, The evolution of the deformation substructure in a Ni-Co-Cr equiatomic solid solution alloy, Acta Mater. 132 (2017) 35-48.

[87] Z.J. Zhang, H.W. Sheng, Z.J. Wang, B. Gludovatz, Z. Zhang, E.P. George, Q. Yu, S.X. Mao, R.O. Ritchie, Dislocation mechanisms and 3D twin architectures generate exceptional strength-ductility-toughness combination in CrCoNi medium-entropy alloy, Nat. Commun. 8 (2017).

[88] J. Chen, P.Y. Niu, Y.Z. Liu, Y.K. Lu, X.H. Wang, Y.L. Peng, J.N. Liu, Effect of Zr content on microstructure and mechanical properties of AlCoCrFeNi high entropy alloy, Mater. Des. 94 (2016) 39-44.

[89] Y. Dong, K.Y. Zhou, Y. Lu, X.X. Gao, T.M. Wang, T.J. Li, Effect of vanadium addition on the microstructure and properties of AlCoCrFeNi high entropy alloy, Mater. Des. 57 (2014) 67-72.

[90] Z.Q. Fu, W.P. Chen, S.C. Fang, X.M. Li, Effect of Cr addition on the alloying behavior, microstructure and mechanical properties of twinned $CoFeNiAl_{0.5}Ti_{0.5}$ alloy, Mater. Sci. Eng. A 597 (2014) 204-211.

[91] Y. Liu, J.S. Wang, Q.H. Fang, B. Liu, Y. Wu, S.Q. Chen, Preparation of superfine-

grained high entropy alloy by spark plasma sintering gas atomized powder, Intermetallics 68 (2016) 16-22.

[92] I. Moravcik, J. Cizek, P. Gavendova, S. Sheikh, S. Guo, I. Dlouhy, Effect of heat treatment on microstructure and mechanical properties of spark plasma sintered $AlCoCrFeNiTi_{0.5}$ high entropy alloy, Mater. Lett. 174 (2016) 53-56.

[93] Y.J. Yin, J.Q. Sun, J. Guo, X.F. Kan, D.C. Yang, Mechanism of high yield strength and yield ratio of 316 L stainless steel by additive manufacturing, Mater. Sci. Eng. A 744 (2019) 773-777.

[94] A. Yadollahi, N. Shamsaei, S.M. Thompson, D.W. Seely, Effects of process time interval and heat treatment on the mechanical and microstructural properties of direct laser deposited 316L stainless steel, Mater. Sci. Eng. A 644 (2015) 171-183.

[95] A. Yadollahi, N. Shamsaei, Y. Hammi, M.F. Horstemeyer, Quantification of tensile damage evolution in additive manufactured austenitic stainless steels, Mater. Sci. Eng. A 657 (2016) 399-405.

[96] Y. Xue, A. Pascu, M.F. Horstemeyer, L. Wang, P.T. Wang, Microporosity effects on cyclic plasticity and fatigue of LENS^{TM}-processed steel, Acta Mater. 58 (2010) 4029-4038.

[97] L. Wang, S.D. Felicelli, J.E. Craig, Experimental and numerical study of the LENS rapid fabrication process, J. Manuf. Sci. Eng. 131 (2009).

[98] B. Zheng, Y. Zhou, J.E. Smugeresky, J.M. Schoenung, E.J. Lavernia, Thermal behavior and microstructural evolution during laser deposition with laser-engineered net shaping: Part I. Numerical calculations, Metall. Mater. Trans. A 39A (2008) 2228-2236.

[99] I. Yadroitsev, P. Krakhmalev, I. Yadroitsava, Selective laser melting of Ti6Al4V alloy for biomedical applications: temperature monitoring and microstructural

evolution, J. Alloys Compd. 583 (2014) 404-409.

[100] W. Xu, E.W. Lui, A. Pateras, M. Qian, M. Brandt, In situ tailoring microstructure in additively manufactured Ti-6Al-4V for superior mechanical performance, Acta Mater. 125 (2017) 390-400.

[101] W. Xu, M. Brandt, S. Sun, J. Elambasseril, Q. Liu, K. Latham, K. Xia, M. Qian, Additive manufacturing of strong and ductile Ti-6Al-4V by selective laser melting via in situ martensite decomposition, Acta Mater. 85 (2015) 74-84.

[102] X.Q. Wang, L.N. Carter, B. Pang, M.M. Attallah, M.H. Loretto, Microstructure and yield strength of SLM-fabricated CM247LC Ni-superalloy, Acta Mater. 128 (2017) 87-95.

[103] G.Q. Yu, D.D. Gu, D.H. Dai, M.J. Xia, C.L. Ma, Q.M. Shi, On the role of processing parameters in thermal behavior, surface morphology and accuracy during laser 3D printing of aluminum alloy, J. Phys. D 49 (2016).

[104] P.P. Yuan, D.D. Gu, Molten pool behaviour and its physical mechanism during selective laser melting of TiC/AlSi10Mg nanocomposites: simulation and experiments, J. Phys. D 48 (2015).

[105] Y.H. Zhou, W.P. Li, D.W. Wang, L. Zhang, K. Ohara, J. Shen, T. Ebel, M. Yan, Selective laser melting enabled additive manufacturing of Ti–22Al–25Nb intermetallic: excellent combination of strength and ductility, and unique microstructural features associated, Acta Mater. 173 (2019) 117-129.

[106] I. Kunce, M. Polanski, K. Karczewski, T. Plocinski, K.J. Kurzydlowski, Microstructural characterisation of high-entropy alloy AlCoCrFeNi fabricated by laser engineered net shaping, J. Alloys Compd. 648 (2015) 751-758.

[107] T. Fujieda, H. Shiratori, K. Kuwabara, T. Kato, K. Yamanaka, Y. Koizumi, A. Chiba, First demonstration of promising selective electron beam melting method for

utilizing high-entropy alloys as engineering materials, Mater. Lett. 159 (2015) 12-15.

[108] H. Shiratori, T. Fujieda, K. Yamanaka, Y. Koizumi, K. Kuwabara, T. Kato, A. Chiba, Relationship between the microstructure and mechanical properties of an equiatomic AlCoCrFeNi high-entropy alloy fabricated by selective electron beam melting, Mater. Sci. Eng. A 656 (2016) 39-46.

[109] J. Joseph, P. Hodgson, T. Jarvis, X.H. Wu, N. Stanford, D.M. Fabijanic, Effect of hot isostatic pressing on the microstructure and mechanical properties of additive manufactured Al_xCoCrFeNi high entropy alloys, Mater. Sci. Eng. A 733 (2018) 59-70.

[110] J. Joseph, T. Jarvis, X.H. Wu, N. Stanford, P. Hodgson, D.M. Fabijanic, Comparative study of the microstructures and mechanical properties of direct laser fabricated and arc-melted Al_xCoCrFeNi high entropy alloys, Mater. Sci. Eng. A 633 (2015) 184-193.

[111] J. Joseph, N. Stanford, P. Hodgson, D.M. Fabijanic, Tension/compression asymmetry in additive manufactured face centered cubic high entropy alloy, Scr. Mater. 129 (2017) 30-34.

[112] Z.G. Zhu, Q.B. Nguyen, F.L. Ng, X.H. An, X.Z. Liao, P.K. Liaw, S.M.L. Nai, J. Wei, Hierarchical microstructure and strengthening mechanisms of a CoCrFeNiMn high entropy alloy additively manufactured by selective laser melting, Scr. Mater. 154 (2018) 20-24.

[113] R.D. Li, P.D. Niu, T.C. Yuan, P. Cao, C. Chen, K.C. Zhou, Selective laser melting of an equiatomic CoCrFeMnNi high-entropy alloy: processability, non-equilibrium microstructure and mechanical property, J. Alloys Compd. 746 (2018) 125-134.

[114] A. Piglione, B. Dovgyy, C. Liu, C.M. Gourlay, P.A. Hooper, M.S. Pham, Printability and microstructure of the CoCrFeMnNi high-entropy alloy fabricated by laser powder bed fusion, Mater. Lett. 224 (2018) 22-25.

[115] Z. Qiu, C. Yao, K. Feng, Z. Li, P.K. Chu, Cryogenic deformation mechanism of CrMnFeCoNi high-entropy alloy fabricated by laser additive manufacturing process, Int. J. Lightweight Mater. Manuf. 1 (2018) 33-39.

[116] S. Xiang, H.W. Luan, J. Wu, K.F. Yao, J.F. Li, X. Liu, Y.Z. Tian, W.L. Mao, H. Bai, G.M. Le, Q. Li, Microstructures and mechanical properties of CrMnFeCoNi high entropy alloys fabricated using laser metal deposition technique, J. Alloys Compd. 773 (2019) 387-392.

[117] X. Gao, Y. Lu, Laser 3D printing of CoCrFeMnNi high-entropy alloy, Mater. Lett. 236 (2019) 77-80.

[118] Z. Tong, X. Ren, J. Jiao, W. Zhou, Y. Ren, Y. Ye, E.A. Larson, J. Gu, Laser additive manufacturing of FeCrCoMnNi high-entropy alloy: effect of heat treatment on microstructure, residual stress and mechanical property, J. Alloys Compd. 785 (2019) 1144-1159.

[119] S. Guan, D. Wan, K. Solberg, F. Berto, T. Welo, T.M. Yue, K.C. Chan, Additive manufacturing of fine-grained and dislocation-populated CrMnFeCoNi high entropy alloy by laser engineered net shaping, Mater. Sci. Eng. A 761 (2019) 138056.

[120] Y. Chew, G.J. Bi, Z.G. Zhu, F.L. Ng, F. Weng, S.B. Liu, S.M.L. Nai, B.Y. Lee, Microstructure and enhanced strength of laser aided additive manufactured CoCrFeNiMn high entropy alloy, Mater. Sci. Eng. A 744 (2019) 137-144.

[121] T. Fujieda, H. Shiratori, K. Kuwabara, M. Hirota, T. Kato, K. Yamanaka, Y. Koizumi, A. Chiba, S. Watanabe, CoCrFeNiTi-based high-entropy alloy with superior tensile strength and corrosion resistance achieved by a combination of additive manufacturing using selective electron beam melting and solution treatment, Mater. Lett. 189 (2017) 148-151.

[122] I. Kunce, M. Polanski, J. Bystrzycki, Microstructure and hydrogen storage

properties of a TiZrNbMoV high entropy alloy synthesized using laser engineered net shaping (LENS), Int. J. Hydrogen Energy 39 (2014) 9904-9910.

[123] D. Choudhuri, T. Alam, T. Borkar, B. Gwalani, A.S. Mantri, S.G. Srinivasan, M.A. Gibson, R. Banerjee, Formation of a Huesler-like $L2_1$ phase in a CoCrCuFeNiAlTi high-entropy alloy, Scr. Mater. 100 (2015) 36-39.

[124] T. Borkar, V. Chaudhary, B. Gwalani, D. Choudhuri, C.V. Mikler, V. Soni, T. Alam, R.V. Ramanujan, R. Banerjee, A combinatorial approach for assessing the magnetic properties of high entropy alloys: role of Cr in $AlCo_xCr_{1-x}FeNi$, Adv. Eng. Mater. 19 (2017) 1700048.

[125] T. Borkar, B. Gwalani, D. Choudhuri, C.V. Mikler, C.J. Yannetta, X. Chen, R.V. Ramanujan, M.J. Styles, M.A. Gibson, R. Banerjee, A combinatorial assessment of $Al_xCrCuFeNi_2$ ($0 < x < 1.5$) complex concentrated alloys: microstructure, microhardness, and magnetic properties, Acta Mater. 116 (2016) 63-76.

[126] B. Gwalani, V. Soni, O.A. Waseem, S.A. Mantri, R. Banerjee, Laser additive manufacturing of compositionally graded $AlCrFeMoV_x$ ($x = 0$ to 1) high-entropy alloy system, Opt. Laser Technol. 113 (2019) 330-337.

[127] M.L. Griffith, M.E. Schlienger, L.D. Harwell, M.S. Oliver, M.D. Baldwin, M.T. Ensz, M. Essien, J. Brooks, C.V. Robino, J.E. Smugeresky, W.H. Hofmeister, M.J. Wert, D.V. Nelson, Understanding thermal behavior in the LENS process, Mater. Des. 20 (1999) 107-113.

[128] Y. Xiong, W.H. Hofmeister, Z. Cheng, J.E. Smugeresky, E.J. Lavernia, J.M. Schoenung, In situ thermal imaging and three-dimensional finite element modeling of tungsten carbide-cobalt during laser deposition, Acta Mater. 57 (2009) 5419-5429.

[129] Y.H. Xiong, W.H. Hofmeister, J.E. Smugeresky, J.P. Delplanque, J.M. Schoenung, Investigation of atypical molten pool dynamics in tungsten carbide-cobalt

during laser deposition using in-situ thermal imaging, Appl. Phys. Lett. 100 (2012).

[130] L. Wang, S. Felicelli, Analysis of thermal phenomena in LENS^{TM} deposition, Mater. Sci. Eng. A 435 (2006) 625-631.

[131] L. Wang, S. Felicelli, Y. Gooroochurn, P.T. Wang, M.F. Horstemeyer, Optimization of the LENS process for steady molten pool size, Mater. Sci. Eng. A 474 (2008) 148-156.

[132] R. Ye, J.E. Smugeresky, B. Zheng, Y. Zhou, E.J. Lavernia, Numerical modeling of the thermal behavior during the LENS process, Mater. Sci. Eng. A 428 (2006) 47-53.

[133] W. Xiao, S. Li, C. Wang, Y. Shi, J. Mazumder, H. Xing, L. Song, Multi-scale simulation of dendrite growth for direct energy deposition of nickel-based superalloys, Mater. Des. 164 (2019) 107553.

[134] P.P. Yuan, D.D. Gu, D.H. Dai, Particulate migration behavior and its mechanism during selective laser melting of TiC reinforced Al matrix nanocomposites, Mater. Des. 82 (2015) 46-55.

[135] M. Gäumann, S. Henry, F. Cleton, J.D. Wagniere, W. Kurz, Epitaxial laser metal forming: analysis of microstructure formation, Mater. Sci. Eng. A 271 (1999) 232-241.

[136] G.P. Dinda, A.K. Dasgupta, J. Mazumder, Laser aided direct metal deposition of Inconel 625 superalloy: microstructural evolution and thermal stability, Mater. Sci. Eng. A 509 (2009) 98-104.

[137] H. Yin, S.D. Felicelli, Dendrite growth simulation during solidification in the LENS process, Acta Mater. 58 (2010) 1455-1465.

[138] X. Lin, T.M. Yue, H.O. Yang, W.D. Huang, Microstructure and phase evolution in laser rapid forming of a functionally graded Ti-Rene88DT alloy, Acta Mater. 54 (2006) 1901-1915.

[139] X. Lin, T.M. Yue, H.O. Yang, W.D. Huang, Laser rapid forming of SS316L/Rene88DT graded material, Mater. Sci. Eng. A 391 (2005) 325-336.

[140] X. Lin, T.M. Yue, Phase formation and microstructure evolution in laser rapid forming of graded SS316L/Rene88DT alloy, Mater. Sci. Eng. A 402 (2005) 294-306.

[141] Y.M. Li, H. Yang, X. Lin, W.D. Huang, J.G. Li, Y.H. Zhou, The influences of processing parameters on forming characterizations during laser rapid forming, Mater. Sci. Eng. A 360 (2003) 18-25.

[142] W. Kurz, C. Bezencon, M. Gäumann, Columnar to equiaxed transition in solidification processing, Sci. Technol. Adv. Mat. 2 (2001) 185-191.

[143] M. Gäumann, C. Bezencon, P. Canalis, W. Kurz, Single-crystal laser deposition of superalloys: processing-microstructure maps, Acta Mater. 49 (2001) 1051-1062.

[144] D. Dube, M. Fiset, A. Couture, I. Nakatsugawa, Characterization and performance of laser melted AZ91D and AM60B, Mater. Sci. Eng. A 299 (2001) 38-45.

[145] F. Cleton, P.H. Jouneau, S. Henry, M. Gaumann, P.A. Buffat, Crystallographic orientation assessment by electron backscattered diffraction, Scanning 21 (1999) 232-237.

[146] R. Banerjee, P.C. Collins, A. Genc, H.L. Fraser, Direct laser deposition of in situ Ti-6Al-4V-TiB composites, Mater. Sci. Eng. A 358 (2003) 343-349.

[147] R.S. Amano, P.K. Rohatgi, Laser engineered net shaping process for SAE 4140 low alloy steel, Mater. Sci. Eng. A 528 (2011) 6680-6693.

[148] R. Banerjee, C.A. Brice, S. Banerjee, H.L. Fraser, Microstructural evolution in laser deposited Ni-25at.% Mo alloy, Mater. Sci. Eng. A 347 (2003) 1-4.

[149] Y.Z. Zhou, A. Volek, N.R. Green, Mechanism of competitive grain growth in directional solidification of a nickel-base superalloy, Acta Mater. 56 (2008) 2631-2637.

[150] X.H. Zhan, Z.B. Dong, Y.H. Wei, R. Ma, Simulation of grain morphologies and competitive growth in weld pool of Ni-Cr alloy, J. Cryst. Growth 311 (2009) 4778-4783.

[151] Y.Y. Zhu, D. Liu, X.J. Tian, H.B. Tang, H.M. Wang, Characterization of microstructure and mechanical properties of laser melting deposited Ti-6.5Al-3.5Mo-1.5Zr-0.3Si titanium alloy, Mater. Des. 56 (2014) 445-453.

[152] T. Wang, Y.Y. Zhu, S.Q. Zhang, H.B. Tang, H.M. Wang, Grain morphology evolution behavior of titanium alloy components during laser melting deposition additive manufacturing, J. Alloys Compd. 632 (2015) 505-513.

[153] L.L. Parimi, G.A. Ravi, D. Clark, M.M. Attallah, Microstructural and texture development in direct laser fabricated IN718, Mater. Charact. 89 (2014) 102-111.

[154] K.V. Yang, Y.J. Shi, F. Palm, X.H. Wu, P. Rometsch, Columnar to equiaxed transition in Al-Mg(-Sc)-Zr alloys produced by selective laser melting, Scr. Mater. 145 (2018) 113-117.

[155] A.B. Spierings, K. Dawson, T. Heeling, P.J. Uggowitzer, R. Schäublin, F. Palm, K. Wegener, Microstructural features of Sc- and Zr-modified Al-Mg alloys processed by selective laser melting, Mater. Des. 115 (2017) 52-63.

[156] Y.B. Zuo, B. Jiang, Y. Zhang, Z. Fan, Iop, Grain refinement of DC cast magnesium alloys with intensive melt shearing, 3rd International Conference on Advances in Solidification Processes2012.

[157] Y.H. Zhang, X.R. Cheng, H.G. Zhong, Z.S. Xu, L.J. Li, Y.Y. Gong, X.C. Miao, C.J. Song, Q.J. Zhai, Comparative study on the grain refinement of Al-Si alloy solidified under the impact of pulsed electric current and travelling magnetic field, Metals 6 (2016).

[158] T. Yuan, Z. Luo, S. Kou, Grain refining of magnesium welds by arc oscillation,

Acta Mater. 116 (2016) 166-176.

[159] S. Wang, J. Kang, X. Zhang, Z. Guo, A study on the effect of ultrasonic treatment on the microstructure of Sn-30 wt.% Bi alloy, Materials 11 (2018).

[160] M.X. Zhang, C.M. Liu, X.Z. Shi, X.P. Chen, C. Chen, J.H. Zuo, J.P. Lu, S.Y. Ma, Residual stress, defects and grain morphology of Ti-6Al-4V alloy produced by ultrasonic impact treatment assisted selective laser melting, Appl. Sci. 6 (2016).

[161] C.J. Todaro, M.A. Easton, D. Qiu, D. Zhang, M.J. Bermingham, E.W. Lui, M. Brandt, D.H. StJohn, M. Qian, Grain structure control during metal 3D printing by high-intensity ultrasound, Nat. Commun. 11 (2020) 142.

[162] G. Zimmermann, C. Pickmann, M. Hamacher, E. Schaberger-Zimmermann, H. Neumann-Heyme, K. Eckert, S. Eckert, Fragmentation-driven grain refinement in directional solidification of AlCu10wt-% alloy at low pulling speeds, Acta Mater. 126 (2017) 236-250.

[163] H. Yasuda, Y. Yamamoto, N. Nakatsuka, M. Yoshiya, T. Nagira, A. Sugiyama, I. Ohnaka, K. Uesugi, K. Umetani, In situ observation of solidification phenomena in Al-Cu and Fe-Si-Al alloys, Int. J. Cast Met. Res. 22 (2009) 15-21.

[164] E. Wesner, A. Choudhury, A. August, M. Berghoff, B. Nestler, A phase-field study of large-scale dendrite fragmentation in Al-Cu, J. Cryst. Growth 359 (2012) 107-121.

[165] N. Wang, S. Mokadem, M. Rappaz, W. Kurz, Solidification cracking of superalloy single- and bi-crystals, Acta Mater. 52 (2004) 3173-3182.

[166] H. Peng, Y. Shi, S. Gong, H. Guo, B. Chen, Microstructure, mechanical properties and cracking behaviour in γ'–precipitation strengthened nickel-base superalloy fabricated by electron beam melting, Mater. Des. 159 (2018) 155-169.

[167] Q.Q. Han, R. Mertens, M.L. Montero-Sistiaga, S.F. Yang, R. Setchi, K.

Vanmeensel, B. Van Hooreweder, S.L. Evans, H.Y. Fan, Laser powder bed fusion of Hastelloy X: effects of hot isostatic pressing and the hot cracking mechanism, Mater. Sci. Eng. A 732 (2018) 228-239.

[168] L. Wang, N. Wang, N. Provatas, Liquid channel segregation and morphology and their relation with hot cracking susceptibility during columnar growth in binary alloys, Acta Mater. 126 (2017) 302-312.

[169] Y. Chen, F.G. Lu, K. Zhang, P.L. Nie, S.R.E. Hosseini, K. Feng, Z.G. Li, Dendritic microstructure and hot cracking of laser additive manufactured Inconel 718 under improved base cooling, J. Alloys Compd. 670 (2016) 312-321.

[170] Y. Chen, F.G. Lu, K. Zhang, P.L. Nie, S.R.E. Hosseini, K. Feng, Z.G. Li, P.K. Chu, Investigation of dendritic growth and liquation cracking in laser melting deposited Inconel 718 at different laser input angles, Mater. Des. 105 (2016) 133-141.

[171] Y. Chen, K. Zhang, J. Huang, S.R.E. Hosseini, Z.G. Li, Characterization of heat affected zone liquation cracking in laser additive manufacturing of Inconel 718, Mater. Des. 90 (2016) 586-594.

[172] O.A. Ojo, N.L. Richards, M.C. Chaturvedi, Contribution of constitutional liquation of gamma prime precipitate to weld HAZ cracking of cast Inconel 738 superalloy, Scr. Mater. 50 (2004) 641-646.

[173] O.A. Ojo, N.L. Richards, M.C. Chaturvedi, Study of the fusion zone and heat-affected zone microstructures in tungsten inert gas-welded INCONEL 738LC superalloy, Metall. Mater. Trans. A 37A (2006) 421-433.

[174] M. Zhong, H. Sun, W. Liu, X. Zhu, J. He, Boundary liquation and interface cracking characterization in laser deposition of Inconel 738 on directionally solidified Ni-based superalloy, Scr. Mater. 53 (2005) 159-164.

[175] S. Asavavisithchai, W. Homkrajai, P. Wangyao, Strain-age cracking after

postweld heat treatments in Inconel 738 superalloy, High Temp. Mater. Processes (London), 2010, p. 61.

[176] A.J. Ramirez, J.C. Lippold, High temperature behavior of Ni-base weld metal: part II. insight into the mechanism for ductility dip cracking, Mater. Sci. Eng. A 380 (2004) 245-258.

[177] A.A.N. Németh, D.J. Crudden, D.E.J. Armstrong, D.M. Collins, K. Li, A.J. Wilkinson, C.R.M. Grovenor, R.C. Reed, Environmentally-assisted grain boundary attack as a mechanism of embrittlement in a nickel-based superalloy, Acta Mater. 126 (2017) 361-371.

[178] X.M. Zhao, X. Lin, J. Chen, L. Xue, W.D. Huang, The effect of hot isostatic pressing on crack healing, microstructure, mechanical properties of Rene88DT superalloy prepared by laser solid forming, Mater. Sci. Eng. A 504 (2009) 129-134.

[179] Y.H. Zhou, Z.H. Zhang, Y.P. Wang, G. Liu, S.Y. Zhou, Y.L. Li, J. Shen, M. Yan, Selective laser melting of typical metallic materials: an effective process prediction model developed by energy absorption and consumption analysis, Addit. Manuf. 25 (2019) 204-217.

[180] K.G. Prashanth, S. Scudino, T. Maity, J. Das, J. Eckert, Is the energy density a reliable parameter for materials synthesis by selective laser melting?, Mater. Res. Lett. 5 (2017) 386-390.

[181] N.T. Aboulkhair, N.M. Everitt, I. Ashcroft, C. Tuck, Reducing porosity in AlSi10Mg parts processed by selective laser melting, Addit. Manuf. 1-4 (2014) 77-86.

[182] R. Cunningham, A. Nicolas, J. Madsen, E. Fodran, E. Anagnostou, M.D. Sangid, A.D. Rollett, Analyzing the effects of powder and post-processing on porosity and properties of electron beam melted Ti-6Al-4V, Mater. Res. Lett. 5 (2017) 516-525.

[183] J. Zhou, H.-L. Tsai, Porosity formation and prevention in pulsed laser welding, J.

Heat Transfer 129 (2006) 1014-1024.

[184] X.G. Zheng, Y.N. Shi, L.H. Lou, Healing process of casting pores in a Ni-based superalloy by hot isostatic pressing, J. Mater. Sci. Technol. 31 (2015) 1151-1157.

[185] Y.N. Zhang, X. Cao, P. Wanjara, M. Medraj, Oxide films in laser additive manufactured Inconel 718, Acta Mater. 61 (2013) 6562-6576.

[186] L.-N. Zhu, B.-S. Xu, H.-D. Wang, C.-B. Wang, Measurement of residual stresses using nanoindentation method, Crit. Rev. Solid State Mater. Sci. 40 (2015) 77-89.

[187] N.S. Rossini, M. Dassisti, K.Y. Benyounis, A.G. Olabi, Methods of measuring residual stresses in components, Mater. Des. 35 (2012) 572-588.

[188] P. Rangaswamy, M.L. Griffith, M.B. Prime, T.M. Holden, R.B. Rogge, J.M. Edwards, R.J. Sebring, Residual stresses in LENS components using neutron diffraction and contour method, Mater. Sci. Eng. A 399 (2005) 72-83.

[189] P. Pratt, S.D. Felicelli, L. Wang, C.R. Hubbard, Residual stress measurement of laser-engineered net shaping AISI 410 thin plates using neutron diffraction, Metall. Mater. Trans. A 39A (2008) 3155-3163.

[190] R.J. Moat, A.J. Pinkerton, L. Li, P.J. Withers, M. Preuss, Residual stresses in laser direct metal deposited Waspaloy, Mater. Sci. Eng. A 528 (2011) 2288-2298.

[191] G. Albertini, G. Bruno, A. Carrado, F. Fiori, M. Rogante, F. Rustichelli, Determination of residual stresses in materials and industrial components by neutron diffraction, Meas. Sci. Technol. 10 (1999) R56-R73.

[192] X.M. Zhao, J. Chen, X. Lin, W.D. Huang, Study on microstructure and mechanical properties of laser rapid forming Inconel 718, Mater. Sci. Eng. A 478 (2008) 119-124.

[193] A.H. Nickel, D.M. Barnett, F.B. Prinz, Thermal stresses and deposition patterns in layered manufacturing, Mater. Sci. Eng. A 317 (2001) 59-64.

[194] L. Wang, N. Wang, W.J. Yao, Y.P. Zheng, Effect of substrate orientation on the columnar-to-equiaxed transition in laser surface remelted single crystal superalloys, Acta Mater. 88 (2015) 283-292.

[195] L. Wang, N. Wang, Effect of substrate orientation on the formation of equiaxed stray grains in laser surface remelted single crystal superalloys: experimental investigation, Acta Mater. 104 (2016) 250-258.

[196] T. Vilaro, C. Colin, J.D. Bartout, L. Naze, M. Sennour, Microstructural and mechanical approaches of the selective laser melting process applied to a nickel-base superalloy, Mater. Sci. Eng. A 534 (2012) 446-451.

[197] K.G. Prashanth, S. Scudino, H.J. Klauss, K.B. Surreddi, L. Lober, Z. Wang, A.K. Chaubey, U. Kuhn, J. Eckert, Microstructure and mechanical properties of Al-12Si produced by selective laser melting: effect of heat treatment, Mater. Sci. Eng. A 590 (2014) 153-160.

[198] Y. Liu, A. Li, X. Cheng, S.Q. Zhang, H.M. Wang, Effects of heat treatment on microstructure and tensile properties of laser melting deposited AISI 431 martensitic stainless steel, Mater. Sci. Eng. A 666 (2016) 27-33.

[199] W.Z. Wu, J.L. Jiang, H. Jiang, W. Liu, G.W. Li, B.F. Wang, M.X. Tang, J. Zhao, Improving bending and dynamic mechanics performance of 3D printing through ultrasonic strengthening, Mater. Lett. 220 (2018) 317-320.

[200] M.A. Melia, J.D. Carroll, S.R. Whetten, S.N. Esmaeely, J. Locke, E. White, I. Anderson, M. Chandross, J.R. Michael, N. Argibay, E.J. Schindelholz, A.B. Kustas, Mechanical and corrosion properties of additively manufactured CoCrFeMnNi high entropy alloy, Addit. Manuf. 29 (2019) 100833.

[201] Z. Sun, X.P. Tan, M. Descoins, D. Mangelinck, S.B. Tor, C.S. Lim, Revealing hot tearing mechanism for an additively manufactured high-entropy alloy via selective

laser melting, Scr. Mater. 168 (2019) 129-133.

[202] S. Guan, K. Solberg, D. Wan, F. Berto, T. Welo, T.M. Yue, K.C. Chan, Formation of fully equiaxed grain microstructure in additively manufactured $AlCoCrFeNiTi_{0.5}$ high entropy alloy, Mater. Des. 184 (2019) 108202.

[203] P.K. Sarswat, S. Sarkar, A. Murali, W. Huang, W. Tan, M.L. Free, Additive manufactured new hybrid high entropy alloys derived from the AlCoFeNiSmTiVZr system, Appl. Surf. Sci. 476 (2019) 242-258.

[204] H. Dobbelstein, E.L. Gurevich, E.P. George, A. Ostendorf, G. Laplanche, Laser metal deposition of compositionally graded TiZrNbTa refractory high-entropy alloys using elemental powder blends, Addit. Manuf. 25 (2019) 252-262.

[205] S.S. Al-Bermani, M.L. Blackmore, W. Zhang, I. Todd, The origin of microstructural diversity, texture, and mechanical properties in electron beam melted Ti-6Al-4V, Metall. Mater. Trans. A 41 (2010) 3422-3434.

[206] M. Rappaz, J.M. Drezet, M. Gremaud, A new hot-tearing criterion, Metall. Mater. Trans. A 30 (1999) 449-455.

[207] C. Haase, F. Tang, M.B. Wilms, A. Weisheit, B. Hallstedt, Combining thermodynamic modeling and 3D printing of elemental powder blends for high-throughput investigation of high-entropy alloys - Towards rapid alloy screening and design, Mater. Sci. Eng. A 688 (2017) 180-189.

[208] M. Moorehead, K. Bertsch, M. Niezgoda, C. Parkin, M. Elbakhshwan, K. Sridharan, C. Zhang, D. Thoma, A. Couet, High-throughput synthesis of Mo-Nb-Ta-W high-entropy alloys via additive manufacturing, Mater. Des. 187 (2020) 108358.

[209] I. Kunce, M. Polanski, J. Bystrzycki, Structure and hydrogen storage properties of a high entropy ZrTiVCrFeNi alloy synthesized using laser engineered net shaping (LENS), Int. J. Hydrogen Energy 38 (2013) 12180-12189.

[210] S. Ozbilen, Satellite formation mechanism in gas atomised powders, Powder Metall. 42 (1999) 70-78.

[211] K.N. Amato, S.M. Gaytan, L.E. Murr, E. Martinez, P.W. Shindo, J. Hernandez, S. Collins, F. Medina, Microstructures and mechanical behavior of Inconel 718 fabricated by selective laser melting, Acta Mater. 60 (2012) 2229-2239.

[212] E. Cakmak, M.M. Kirka, T.R. Watkins, R.C. Cooper, K. An, H. Choo, W. Wu, R.R. Dehoff, S.S. Babu, Microstructural and micromechanical characterization of IN718 theta shaped specimens built with electron beam melting, Acta Mater. 108 (2016) 161-175.

[213] B.E. Carroll, T.A. Palmer, A.M. Beese, Anisotropic tensile behavior of Ti-6Al-4V components fabricated with directed energy deposition additive manufacturing, Acta Mater. 87 (2015) 309-320.

[214] J.R. Croteau, S. Griffiths, M.D. Rossell, C. Leinenbach, C. Kenel, V. Jansen, D.N. Seidman, D.C. Dunand, N.Q. Vo, Microstructure and mechanical properties of Al-Mg-Zr alloys processed by selective laser melting, Acta Mater. 153 (2018) 35-44.

[215] B. Zheng, Y. Zhou, J.E. Smugeresky, J.M. Schoenung, E.J. Lavernia, Thermal behavior and microstructure evolution during laser deposition with laser-engineered net shaping: part II. experimental investigation and discussion, Metall. Mater. Trans. A 39A (2008) 2237-2245.

[216] L. Carter, M. Attallah, R. C. Reed, Laser powder bed fabrication of nickel-base superalloys: influence of parameters; characterisation, quantification and mitigation of cracking, 2012, pp. 577-586.

[217] J. Zhang, R.F. Singer, Hot tearing of nickel-based superalloys during directional solidification, Acta Mater. 50 (2002) 1869-1879.

[218] F. Otto, A. Dlouhy, C. Somsen, H. Bei, G. Eggeler, E.P. George, The influences

of temperature and microstructure on the tensile properties of a CoCrFeMnNi high-entropy alloy, Acta Mater. 61 (2013) 5743-5755.

[219] S.H. Joo, H. Kato, M.J. Jang, J. Moon, E.B. Kim, S.J. Hong, H.S. Kim, Structure and properties of ultrafine-grained CoCrFeMnNi high-entropy alloys produced by mechanical alloying and spark plasma sintering, J. Alloys Compd. 698 (2017) 591-604.

[220] H. Shahmir, J. He, Z. Lu, M. Kawasaki, T.G. Langdon, Effect of annealing on mechanical properties of a nanocrystalline CoCrFeNiMn high-entropy alloy processed by high-pressure torsion, Mater. Sci. Eng. A 676 (2016) 294-303.

[221] I.A. Ovid'ko, R.Z. Valiev, Y.T. Zhu, Review on superior strength and enhanced ductility of metallic nanomaterials, Prog. Mater Sci. 94 (2018) 462-540.

[222] E. Ma, Instabilities and ductility of nanocrystalline and ultrafine-grained metals, Scr. Mater. 49 (2003) 663-668.

[223] Y. Wang, M. Chen, F. Zhou, E. Ma, High tensile ductility in a nanostructured metal, Nature 419 (2002) 912.

[224] I. Palcic, M. Balazic, M. Milfelner, B. Buchmeister, Potential of laser engineered net shaping (LENS) technology, Mater. Manuf. Processes 24 (2009) 750-753.

[225] M. Tang, P.C. Pistorius, S. Narra, J.L. Beuth, Rapid solidification: selective laser melting of AlSi10Mg, JOM 68 (2016) 960-966.

[226] M. Laurent-Brocq, A. Akhatova, L. Perriere, S. Chebini, X. Sauvage, E. Leroy, Y. Champion, Insights into the phase diagram of the CrMnFeCoNi high entropy alloy, Acta Mater. 88 (2015) 355-365.

[227] G.P. Dinda, A.K. Dasgupta, J. Mazumder, Evolution of microstructure in laser deposited Al-11.28%Si alloy, Surf. Coat. Technol. 206 (2012) 2152-2160.

[228] G.P. Dinda, A.K. Dasgupta, J. Mazumder, Texture control during laser deposition of nickel-based superalloy, Scr. Mater. 67 (2012) 503-506.

[229] G.P. Dinda, A.K. Dasgupta, S. Bhattacharya, H. Natu, B. Dutta, J. Mazumder, Microstructural characterization of laser-deposited Al 4047 alloy, Metall. Mater. Trans. A 44A (2013) 2233-2242.

[230] Y.M. Ren, X. Lin, X. Fu, H. Tan, J. Chen, W.D. Huang, Microstructure and deformation behavior of Ti-6A1-4V alloy by high-power laser solid forming, Acta Mater. 132 (2017) 82-95.

[231] S. Gorsse, C. Hutchinson, M. Goune, R. Banerjee, Additive manufacturing of metals: a brief review of the characteristic microstructures and properties of steels, Ti-6Al-4V and high-entropy alloys, Sci. Technol. Adv. Mat. 18 (2017) 584-610.

[232] C. Qiu, M.A. Kindi, A.S. Aladawi, I.A. Hatmi, A comprehensive study on microstructure and tensile behaviour of a selectively laser melted stainless steel, Sci. Rep. 8 (2018) 7785.

[233] L. Liu, Q. Ding, Y. Zhong, J. Zou, J. Wu, Y.-L. Chiu, J. Li, Z. Zhang, Q. Yu, Z. Shen, Dislocation network in additive manufactured steel breaks strength–ductility trade-off, Mater. Today 21 (2018) 354-361.

[234] D.Y. Deng, R.L. Peng, H. Brodin, J. Moverare, Microstructure and mechanical properties of Inconel 718 produced by selective laser melting: sample orientation dependence and effects of post heat treatments, Mater. Sci. Eng. A 713 (2018) 294-306.

[235] J. Chen, Z. Yao, X. Wang, Y. Lu, X. Wang, Y. Liu, X. Fan, Effect of C content on microstructure and tensile properties of as-cast CoCrFeMnNi high entropy alloy, Mater. Chem. Phys. 210 (2018) 136-145.

[236] G.A. Salishchev, M.A. Tikhonovsky, D.G. Shaysultanov, N.D. Stepanov, A.V. Kuznetsov, I.V. Kolodiy, A.S. Tortika, O.N. Senkov, Effect of Mn and V on structure and mechanical properties of high-entropy alloys based on CoCrFeNi system, J. Alloys Compd. 591 (2014) 11-21.

[237] J. Friedel, Dislocations, New York, Pergamon Press, 1964.

[238] V. Mohles, Simulations of dislocation glide in overaged precipitation-hardened crystals, Philos. Mag. A 81 (2001) 971-990.

[239] S.J. Sun, Y.Z. Tian, H.R. Lin, X.G. Dong, Y.H. Wang, Z.J. Zhang, Z.F. Zhang, Enhanced strength and ductility of bulk CoCrFeMnNi high entropy alloy having fully recrystallized ultrafine-grained structure, Mater. Des. 133 (2017) 122-127.

[240] G.I. Taylor, The mechanism of plastic deformation of crystals. Part I.—Theoretical, Proc. R. Soc. Lond. A 145 (1934) 362.

[241] R.E. Stoller, S.J. Zinkle, On the relationship between uniaxial yield strength and resolved shear stress in polycrystalline materials, J. Nucl. Mater. 283-287 (2000) 349-352.

[242] G. Laplanche, P. Gadaud, O. Horst, F. Otto, G. Eggeler, E.P. George, Temperature dependencies of the elastic moduli and thermal expansion coefficient of an equiatomic, single-phase CoCrFeMnNi high-entropy alloy, J. Alloys Compd. 623 (2015) 348-353.

[243] Q. Lin, X. An, H. Liu, Q. Tang, P. Dai, X. Liao, In-situ high-resolution transmission electron microscopy investigation of grain boundary dislocation activities in a nanocrystalline CrMnFeCoNi high-entropy alloy, J. Alloys Compd. 709 (2017) 802-807.

[244] Y.H. Zhao, X.Z. Liao, Z. Jin, R.Z. Valiev, Y.T. Zhu, Microstructures and mechanical properties of ultrafine grained 7075 Al alloy processed by ECAP and their evolutions during annealing, Acta Mater. 52 (2004) 4589-4599.

[245] S. Kumari, D.K. Singh, P.K. Giri, Strain anisotropy in freestanding germanium nanoparticles synthesized by ball milling, J. Nanosci. Nanotechnol. 9 (2009) 5231-5236.

[246] G.K. Williamson, R.E. Smallman, III. Dislocation densities in some annealed and

cold-worked metals from measurements on the X-ray debye-scherrer spectrum, Philos. Mag. 1 (1956) 34-46.

[247] D. Wang, C. Song, Y. Yang, Y. Bai, Investigation of crystal growth mechanism during selective laser melting and mechanical property characterization of 316L stainless steel parts, Mater. Des. 100 (2016) 291-299.

[248] G.P. Dinda, L. Song, J. Mazumder, Fabrication of Ti-6Al-4V scaffolds by direct metal deposition, Metall. Mater. Trans. A 39 (2008) 2914-2922.

[249] H. Ali, H. Ghadbeigi, K. Mumtaz, Processing parameter effects on residual stress and mechanical properties of selective laser melted Ti6Al4V, J. Mater. Eng. Perform. 27 (2018) 4059-4068.

[250] A. Considère, Mémoire sur l’emploi du fer et de l’acier dans les constructions, Ann des Ponts et Chaussés (1885) 574-775.

[251] K. Lu, L. Lu, S. Suresh, Strengthening materials by engineering coherent internal boundaries at the nanoscale, Science 324 (2009) 349.

[252] M.A. Meyers, O. Vöhringer, V.A. Lubarda, The onset of twinning in metals: a constitutive description, Acta Mater. 49 (2001) 4025-4039.

[253] K.M. Rahman, V.A. Vorontsov, D. Dye, The effect of grain size on the twin initiation stress in a TWIP steel, Acta Mater. 89 (2015) 247-257.

[254] I. Gutierrez-Urrutia, D. Raabe, Grain size effect on strain hardening in twinning-induced plasticity steels, Scr. Mater. 66 (2012) 992-996.

[255] I. Gutierrez-Urrutia, S. Zaefferer, D. Raabe, The effect of grain size and grain orientation on deformation twinning in a Fe–22wt.% Mn–0.6wt.% C TWIP steel, Mater. Sci. Eng. A 527 (2010) 3552-3560.

[256] A.J. Zaddach, C. Niu, C.C. Koch, D.L. Irving, Mechanical properties and stacking fault energies of NiFeCrCoMn high-entropy alloy, JOM 65 (2013) 1780-1789.

[257] S. Huang, W. Li, S. Lu, F. Tian, J. Shen, E. Holmström, L. Vitos, Temperature dependent stacking fault energy of FeCrCoNiMn high entropy alloy, Scr. Mater. 108 (2015) 44-47.

[258] Y.T. Zhu, X.Z. Liao, X.L. Wu, J. Narayan, Grain size effect on deformation twinning and detwinning, J. Mater. Sci. 48 (2013) 4467-4475.

[259] U.F. Kocks, Laws for work-hardening and low-temperature creep, J. Eng. Mater. Tech. Trans. ASME 98 (1976) 76-85.

[260] H. Mecking, U.F. Kocks, Kinetics of flow and strain-hardening, Acta Metall. 29 (1981) 1865-1875.

[261] Y. Estrin, H. Mecking, A unified phenomenological description of work hardening and creep based on one-parameter models, Acta Metall. 32 (1984) 57-70.

[262] I.S. Yasnikov, A. Vinogradov, Y. Estrin, Revisiting the Considère criterion from the viewpoint of dislocation theory fundamentals, Scr. Mater. 76 (2014) 37-40.

[263] A. Vinogradov, I.S. Yasnikov, H. Matsuyama, M. Uchida, Y. Kaneko, Y. Estrin, Controlling strength and ductility: Dislocation-based model of necking instability and its verification for ultrafine grain 316L steel, Acta Mater. 106 (2016) 295-303.

[264] A. Vinogradov, Mechanical properties of ultrafine-grained metals: new challenges and perspectives, Adv. Eng. Mater. 17 (2015) 1710-1722.

[265] E.W. Hart, Theory of the tensile test, Acta Metall. 15 (1967) 351-355.

[266] L. Thijs, M.L.M. Sistiaga, R. Wauthle, Q. Xie, J.-P. Kruth, J. Van Humbeeck, Strong morphological and crystallographic texture and resulting yield strength anisotropy in selective laser melted tantalum, Acta Mater. 61 (2013) 4657-4668.

[267] E. Chauvet, P. Kontis, E.A. Jagle, B. Gault, D. Raabe, C. Tassin, J.J. Blandin, R. Dendievel, B. Vayre, S. Abed, G. Martin, Hot cracking mechanism affecting a non-weldable Ni-based superalloy produced by selective electron beam melting, Acta Mater.

142 (2018) 82-94.

[268] L. Thijs, K. Kempen, J.P. Kruth, J. Van Humbeeck, Fine-structured aluminium products with controllable texture by selective laser melting of pre-alloyed AlSi10Mg powder, Acta Mater. 61 (2013) 1809-1819.

[269] X. Tan, Y. Kok, Y.J. Tan, M. Descoins, D. Mangelinck, S.B. Tor, K.F. Leong, C.K. Chua, Graded microstructure and mechanical properties of additive manufactured Ti-6Al-4V via electron beam melting, Acta Mater. 97 (2015) 1-16.

[270] T. Ishimoto, K. Hagihara, K. Hisamoto, S.H. Sun, T. Nakano, Crystallographic texture control of beta-type Ti-15Mo-5Zr-3Al alloy by selective laser melting for the development of novel implants with a biocompatible low Young's modulus, Scr. Mater. 132 (2017) 34-38.

[271] J.D. Hunt, Steady-state columnar and equiaxed growth of dendrites and eutectic, Mater. Sci. Engng. 65 (1984) 75-83.

[272] M. Gäumann, R. Trivedi, W. Kurz, Nucleation ahead of the advancing interface in directional solidification, Mater. Sci. Eng. A 226 (1997) 763-769.

[273] H. Rao, S. Giet, K. Yang, X. Wu, C.H.J. Davies, The influence of processing parameters on aluminium alloy A357 manufactured by selective laser melting, Mater. Des. 109 (2016) 334-346.

[274] M. Löbel, T. Lindner, T. Mehner, T. Lampke, Influence of titanium on microstructure, phase formation and wear behaviour of AlCoCrFeNiTix high-entropy alloy, Entropy 20 (2018).

[275] M. Rappaz, W.J. Boettinger, On dendritic solidification of multicomponent alloys with unequal liquid diffusion coefficients, Acta Mater. 47 (1999) 3205-3219.

[276] W. Kurz, B. Giovanola, R. Trivedi, Theory of microstructural development during rapid solidification, Acta Metall. 34 (1986) 823-830.

[277] J.H. Martin, B.D. Yahata, J.M. Hundley, J.A. Mayer, T.A. Schaedler, T.M. Pollock, 3D printing of high-strength aluminium alloys, Nature 549 (2017) 365-369.

[278] Y. Chen, S. Zhang, H. Song, M. Cheng, H. Li, J. Liu, Sudden transition from columnar to equiaxed grain of cast copper induced by rare earth microalloying, Mater. Des. 91 (2016) 314-320.

[279] H. Yasuda, Y. Yamamoto, N. Nakatsuka, T. Nagira, M. Yoshiya, A. Sugiyama, I. Ohnaka, K. Umetani, K. Uesugi, In situ observation of nucleation, fragmentation and microstructure evolution in Sn-Bi and Al-Cu alloys, Int. J. Cast Met. Res. 21 (2008) 125-128.

[280] D.O. Cox, A.S. Tetelman, Improved fracture toughness of a titanium-alloy laminate by controlled diffusion bonding, J. Adhes. 5 (1973) 279-300.

[281] H. Wu, G.H. Fan, B.C. Jin, L. Geng, X.P. Cui, M. Huang, Fabrication and mechanical properties of TiBw/Ti-Ti(Al) laminated composites, Mater. Des. 89 (2016) 697-702.

[282] T. Li, F.C. Jiang, E.A. Olevsky, K.S. Vecchio, M.A. Meyers, Damage evolution in Ti6Al4V-Al_3Ti metal-intermetallic laminate composites, Mater. Sci. Eng. A 443 (2007) 1-15.

[283] A.B. Pandey, B.S. Majumbar, D.B. Miracle, Laminated particulate-reinforced aluminum composites with improved toughness, Acta Mater. 49 (2001) 405-417.

[284] F. Kummel, T. Hausol, H.W. Hoppel, M. Goken, Enhanced fatigue lives in AA1050A/AA5005 laminated metal composites produced by accumulative roll bonding, Acta Mater. 120 (2016) 150-158.

[285] X.L. Ma, C.X. Huang, J. Moering, M. Ruppert, H.W. Hoppel, M. Goken, J. Narayan, Y.T. Zhu, Mechanical properties of copper/bronze laminates: role of interfaces, Acta Mater. 116 (2016) 43-52.

[286] Y. Du, G.H. Fan, T.B. Yu, N. Hansen, L. Geng, X.X. Huang, Laminated Ti-Al composites: processing, structure and strength, Mater. Sci. Eng. A 673 (2016) 572-580.

[287] M.Y. Seok, J.A. Lee, D.H. Lee, U. Ramamurty, S. Nambu, T. Koseki, J.I. Jang, Decoupling the contributions of constituent layers to the strength and ductility of a multi-layered steel, Acta Mater. 121 (2016) 164-172.

[288] S. Sardar, A. Mandal, S.K. Pal, S.B. Singh, Solid-state joining by roll bonding and accumulative roll bonding, 2015.

[289] C.M. Cepeda-Jiménez, F. Carreño, O.A. Ruano, A.A. Sarkeeva, A.A. Kruglov, R.Y. Lutfullin, Influence of interfacial defects on the impact toughness of solid state diffusion bonded Ti–6Al–4V alloy based multilayer composites, Mater. Sci. Eng. A 563 (2013) 28-35.

[290] K. Burger, M. Rühle, Material transport mechanisms during the diffusion bonding of niobium to Al_2O_3, Ultramicroscopy 29 (1989) 88-97.

[291] S. Roy, B. Butz, A. Wanner, Damage evolution and domain-level anisotropy in metal/ceramic composites exhibiting lamellar microstructures, Acta Mater. 58 (2010) 2300-2312.

[292] S.W. Feng, Q. Guo, Z. Li, G.L. Fan, Z.Q. Li, D.B. Xiong, Y.S. Su, Z.Q. Tan, J. Zhang, D. Zhang, Strengthening and toughening mechanisms in graphene-Al nanolaminated composite micro-pillars, Acta Mater. 125 (2017) 98-108.

[293] X.L. Ma, C.X. Huang, W.Z. Xu, H. Zhou, X.L. Wu, Y.T. Zhu, Strain hardening and ductility in a coarse-grain/nanostructure laminate material, Scr. Mater. 103 (2015) 57-60.